ARGENTUM SENSITIZED ZINC OXIDE PHOTOELECTRODE: FABRICATION, CHARACTERIZATION AND APPLICATION FOR PHOTOELECTROCHEMICAL WATER SPLITTING

SITI NUR HASLINDA BINTI MOHD DAUD

FACULTY OF SCIENCE
UNIVERSITY OF MALAYA
KUALA LUMPUR

2018

ARGENTUM SENSITIZED ZINC OXIDE PHOTOELECTRODE: FABRICATION, CHARACTERIZATION AND APPLICATION FOR PHOTOELECTROCHEMICAL WATER SPLITTING

SITI NUR HASLINDA BINTI MOHD DAUD

THESIS SUBMITTED IN FULFILMENT OF THE
REQUIREMENTS FOR THE DEGREE OF
DOCTOR OF PHILOSOPHY

DEPARTMENT OF PHYSICS
FACULTY OF SCIENCE
UNIVERSITY OF MALAYA
KUALA LUMPUR

2018

UNIVERSITY OF MALAYA
ORIGINAL LITERARY WORK DECLARATION

Name of Candidate: **SITI NUR HASLINDA BINTI MOHD DAUD**

Matric No: **SHC 130066**

Name of Degree: **DOCTOR OF PHILOSOPHY**

Title of Thesis:

ARGENTUM SENSITIZED ZINC OXIDE PHOTOELECTRODE: FABRICATION, CHARACTERIZATION AND APPLICATION FOR PHOTOELECTROCHEMICAL WATER SPLITTING

Field of Study: **EXPERIMENTAL PHYSICS**

I do solemnly and sincerely declare that:

(1) I am the sole author/writer of this Work;
(2) This Work is original;
(3) Any use of any work in which copyright exists was done by way of fair dealing and for permitted purposes and any excerpt or extract from, or reference to or reproduction of any copyright work has been disclosed expressly and sufficiently and the title of the Work and its authorship have been acknowledged in this Work;
(4) I do not have any actual knowledge nor do I ought reasonably to know that the making of this work constitutes an infringement of any copyright work;
(5) I hereby assign all and every rights in the copyright to this Work to the University of Malaya ("UM"), who henceforth shall be owner of the copyright in this Work and that any reproduction or use in any form or by any means whatsoever is prohibited without the written consent of UM having been first had and obtained;
(6) I am fully aware that if in the course of making this Work I have infringed any copyright whether intentionally or otherwise, I may be subject to legal action or any other action as may be determined by UM.

Candidate's Signature Date:

Subscribed and solemnly declared before,

Witness's Signature Date:

Name:

Designation:

ARGENTUM SENSITIZED ZINC OXIDE PHOTOELECTRODE: FABRICATION, CHARACTERIZATION AND APPLICATION FOR PHOTOELECTROCHEMICAL WATER SPLITTING

ABSTRACT

Current research reports the fabrication, structural- and optical-characterizations of Argentum (Ag) sensitized Zinc Oxide (ZnO) photoelectrode and their performance in photoelectrochemical (PEC) water splitting application. The optimization of ZnO nanopillars had been successfully carried out and the plasmonic Ag nanoparticles was then subsequently hydrothermally sensitized on ZnO nanopillars through varied Ag^+ ions reduction time and $AgNO_3$ concentration. The structural- and optical-properties of all samples were systematically characterized by using several characterization tools. After that, all of the samples were tested for PEC water splitting and linear sweep voltammetry technique was conducted to study the current-voltage behaviour. Additionally, Nyquist plot and Mott-Schottky plot were conducted to probe the electronic properties and charge transfer. Ag nanoparticles sensitized ZnO nanopillars with 30 min Ag^+ ions reduction period and 1 mM $AgNO_3$ concentration exhibit the highest photocurrent density (with maximum photoconversion efficiency) which is almost 1.4 times higher than that of ZnO nanopillars. Mott-Schottky analysis indicated that all photoelectrodes exhibit n-type characteristic, where the flat band potential and charge carrier density for all photoelectrodes can be derived hereafter. Ag nanoparticles sensitized ZnO nanopillars with 30 min Ag^+ ions reduction period and 1 mM $AgNO_3$ concentration showed the smallest capacitive arc diameter, which indicated that Ag nanoparticles enhanced the electron mobility and reduced the charge-transfer resistance.

Keywords: Photoelectrochemical water splitting, ZnO nanopillars, Ag nanoparticles, photoconversion efficiency, photocurrent density,

ARGENTUM PEKAAN ZINK OKSIDA FOTOELEKTROD: FABRIKASI, PENCIRIAN, DAN APLIKASI UNTUK FOTOELEKTROKIMIA PEMECAHAN AIR

ABSTRAK

Kajian penyelidikan terkini melaporkan tentang fabrikasi, pencirian struktur dan sifat optik Argentum (Ag) pekaan Zink Oksida (ZnO) fotoelektrod dan penilaian dalam aplikasi fotoelektokimia pemecahan air. Pengoptimuman ZnO turus nano telah berjaya dijalankan dan plasmon Ag zarah nano seterusnya dipekakan terhadap ZnO turus nano secara hidroterma melalui tempoh penurunan Ag^+ ion dan kepekatan $AgNO_3$ yang divariasikan. Sifat struktur dan optik untuk semua sampel dicirikan secara sistematik dengan menggunakan beberapa alatan pencirian. Selepas itu, kesemua sampel diuji untuk PEC pemecahan air dan teknik voltametri imbasan linear dijalankan untuk mengkaji kelakuan arus-voltan. Sebagai tambahan, teknik plot "Nyquist" dan plot "Mott-Schottky" dilakukan untuk mendalami sifat elektonik dan pemindahan cas. Ag zarah nano pekaan ZnO turus nano dengan 30 min tempoh penurunan Ag^+ ion dan 1 mM kepekatan $AgNO_3$ mempamerkan ketumpatan arus yang tertinggi (dengan penukaran foto yang maksima) iaitu 1.4 kali lebih tinggi daripada ZnO turus nano. Analisa "Mott-Schottky" mendapati bahawa kesemua fotoelektrod mempunyai ciri-ciri jenis-n, di mana keupayaan jalur datar dan ketumpatan pembawa cas diperolehi. Ag zarah nano pekaan ZnO turus nano dengan 30 min masa penurunan Ag^+ ion dan 1 mM kemolaran $AgNO_3$ menunjukkan kapasitif diameter lengkok yang terkecil, di mana ia menunjukkan bahawa Ag zarah nano meningkatkan mobiliti elektron dan mengurangkan rintangan pemindahan cas.

Kata kunci: Fotoelektrokimia pemecahan air, ZnO nano turus, Ag nano zarah, kecekapan penukaran foto, ketumpatan arus

ACKNOWLEDGEMENTS

First of all, I want to express my sincere gratitude to Allah S.W.T for His blessings and He had and always facilitate my PhD journey for the past three and half years. He calmed my heart every time I failed and He gave me a way out until I managed to finish up my thesis. Alhamdulillah.

Also, I would like to express my deepest thank to my supervisor, Dr. Chiu Wee Siong and Dr. Zarina Aspanut for their excellent guidance, patience, caring and providing me a vibrant atmosphere for doing research. Besides, I would like to thank to my scholarship, MyPhD for financially supporting my study as well as to all grants funded by University Malaya.

My special thank goes to Dr. Haw, Maisarah, Aimi, Angela, Annie, Aliff, Aidahani and Hamizah, who's as my colleagues, were always willing to help and give best suggestions. Not to forget, AMCAL and LDMRC's members, assistant of science officers, science officers of Physics Department, Faculty Science, University Malaya.

I would like to thanks as well to ISMA KL and KRIM KL for always supporting my Ph.D journey especially Sikin, Shahada, Liza, Wani, Farhana, Fieza, Kinah, Adlina, Aini, Finaz, Amanina, Naima, Hasmira, Soraya, Atifah, Najihah and to my present and previous "*mas'ullah*" and "*usrah-mates*". I am really and always appreciate all those spirits, understanding and sisterhood. My highest appreciation goes to my father and mother in law, my siblings, my siblings in law and my big families for always give me advice and supports as well as for always stay behind me all these times.

Lastly, the most important person in my life, my mother and father, Mrs. Maimon Mohamad and Mr. Mohd Daud Hamdan as well as my lovely husband, Mr. Syed Fariq Fathullah and our son, Syed Mujahid Fathullah, thank you so much for always be by my side, for your love and care, for support me emotionally. This thesis is specially dedicated to you guys. Thank you all.

TABLE OF CONTENTS

CHAPTER 6: PHOTOELECTROCHEMICAL WATER SPLITTING BY USING ARGENTUM NANOPARTICLES SENSITIZED ZINC OXIDE NANOPILLARS PHOTOELECTRODE…………………………………….. **105**

LIST OF FIGURES

LIST OF TABLES

LIST OF SYMBOLS AND ABBREVIATIONS

AM 1.5 G : Air mass 1.5 global

CB : Conduction band

CE : Counter electrode

C_{sc} : Space charge layer capacitance

DI : Deionized

DRS : Diffuse reflectance spectroscope

EIS : Electrochemical impedance spectroscope

E_{fb} : Flat band potential

E_{onset} : Onset potential

FESEM : Field emission scanning electron microscope

FFT : Fast Fourier transform

ff : Fill factor

HAADF : High-angle annular dark field

HABSE : High-angle back scattering electron

HER : Hydrogen evolution reaction

HRTEM : High-resolution transmission electron microscope

IPCC : International Panel on Climate Change

J_{ph} : Photocurrent density

J_{sc} : Short-circuit current density

LABSE : Low-angle back scattering electron

LSV : Linear sweep voltammetry

MS : Mott-Schottky

NHE : Normal hydrogen electrode

NIR : Near infrared

N_D : Donor density

OER : Oxygen evolution reaction

PEC : Photoelectrochemical

PL : Photoluminescence

RE : Reference electrode

RHE : Reversible hydrogen electrode

R_{CT} : Charge transfer resistance

SAED : Selected area electron diffraction

SCE : Standard Calomel electrode

SHE : Standard hydrogen electrode

SPR : Surface plasmon resonance

STEM : Scanning transmission electron microscope

UV : Ultraviolet

VB : Valence band

VIS : Visible

V_{app} : Applied potential

V_{oc} : Open-circuit potential

V_{redox} : Redox potential

WE : Working electrode

XRD : X-ray diffractometer/diffraction

LIST OF APPENDICES

CHAPTER 1: INTRODUCTION

1.1 Introduction

Briefly, this chapter discusses about the introduction of research study, problem statements and the rationale of research. Besides, this chapter states the research objectives as well as the summary of all chapters will be described in the end of this chapter.

1.2 Introduction of Research Study

Basically, this research is studied about the fabrication and characterization of photoelectrode, whereby zinc oxide (ZnO) and Argentum (Ag) are used as the research materials. Ag will be sensitized on the surface of ZnO in order to produce hybrid structures. The sensitization of Ag and ZnO is believed can enhance the performance of PEC application via the photosplitting of water. It is anticipated that the outcomes of this research will beneficial to the advancement of human civilization, especially in terms of clean- and renewable-energy development through applied science research, where the adoption of value-added photoelectron system will serve as platform to tackle the challenge associated to the energy crisis and climate change.

1.3 Problem Statements

For last decade, energy crisis that rely on fossil fuels has become an important issue among the world and effort in sourcing for alternative resources has been frequently become the subject of study among the scientific communities around the world. Currently, over 95 % of hydrogen and over 90 % of electricity are produced from fossil fuels and biomass (Bard, 2008; Sun et al., 2012). Fossil fuels are believed to be a major cause of irreversible and negative environmental consequences, which contributes to huge amount of greenhouse gas such as carbon dioxide (CO_2) (Davis et al., 2010) and incurs serious air pollution. Several research has unravels the major contribution of hydrogen (H_2) technology toward sustainable life and H_2 gas is believed to be one of the renewable fuel and clean-energy sources, which would serve as an alternative to overcome the environmental challenges. In conjunction with this approach, H_2 can work by itself as a source of energy or else together with other carbon source to generate liquid hydrocarbon (Agrawal et al., 2007).

For the sake of environmentally beneficial and economically competitive, it is essential to find a cost-effective and clean method to produce H_2 gas (Lewis, 2007). Photoelectrochemical (PEC) application, using solar energy to split water has become a promising method in providing clean energy sources in the future. Lately, lots of researches have been done to search for a sustainable electrode material (Sun et al., 2012). Continuous research effort and current challenges are to optimize photoelectrodes towards practical PEC applications with a broad spectrum of absorption, matching energy band to water reduction/oxidation energy levels, long-term stability in harsh condition and the utmost importantly is high photocurrent density in order to reach high photo-to-hydrogen conversion efficiency (Bookbinder et al., 1980; Sun et al., 2012).

Recently, research on PEC water splitting has gained a lot of attention, since it is a facile yet environmentally friendly approach for H_2 gas production (Wei et al., 2012). In a PEC system, the selection and design of the photoelectrode material are critical since carrier transport and light absorption of the photoelectrode largely determine the capability and overall performance of PEC cell of water splitting (Wei et al., 2012; Wei et al., 2012). Many metal oxide materials such as WO_3, Fe_2O_3 and TiO_2 have been extensively studied as photoelectrode material (Enesca et al., 2007; Sivula et al., 2009; Wolcott et al., 2009). In general, TiO_2 has been found to be the pioneer photoanode material for water splitting (Fujishima & Honda, 1972). Recently, ZnO also gained great interest due to its high electrochemical stability, suitable valence and conduction band edges that straddle the redox potentials of water, high electron mobility (10-100 fold higher than TiO_2) (Dittrich et al., 1998; Klingshirn, 2007), absorption occurrence in the visible light region induced by the intrinsic defects, and lower recombination rates of charge carriers that arose from longer electrons and holes from the longer polaron decay lifetimes of ZnO (Quintana et al., 2007).

However, the low photocurrent density and low photoconversion efficiency, resulting from the inadequate light absorption of ZnO photoanode are the main issues that hinder its practical application (Wei et al., 2012). In order to enhance the photoconversion efficiency in a ZnO-based PEC cell, many strategies have been reported. For example, reducing the size to the nanoscale to increase the specific surface area (Ahn et al., 2008; Ahn et al., 2008; Wolcott et al., 2009), doping with different kinds of impurities to reduce the band gap and enhance the absorption of visible light (Ahn et al., 2007; Hsu & Lin, 2012). In additional to those methods, sensitizing ZnO with dye or quantum dots (Unalan et al., 2008; Wang et al., 2010), producing solid solution of nitrides (Maeda et al., 2008; Maeda et al., 2009), and modifying ZnO with noble metal nanoparticles also is being explored to enhance light trapping (Wei et al., 2012).

Therefore, in current work, Ag sensitized ZnO photoelectrode is proposed to be fabricated for better enhancement of photoconversion efficiency as well as photocurrent generation. Ag which is one of noble metal material can be used to produce a hybrid Ag/ZnO heterostructure in order to enhance the light trapping caused by the special property belong to Ag which is well known as surface plasmon resonance (SPR). Fermi level of Ag is lower than ZnO, then the photoexcited electrons can be easily transferred from covalence band to Ag deposited on the surface of ZnO, while photogenerated valance band holes remain on the ZnO. These activities reduce the possibility of electron-hole recombination (Ni et al., 2007). Thus, it may increase the photoconversion efficiency. Besides that, we propose to produce Ag sensitized ZnO photoelectrode with vertically aligned on the zinc foil to achieve large surface area to enable efficient light trapping. Therefore, large quanta of light can be captured during the water splitting process, and this would significantly enhance the photocurrent density rate.

1.4 Rationale of Research

In this research, for the first time, the fabrication of Ag/ZnO heterostructures will be conducted at low temperature (50 °C) on Zn foil substrate through hydrothermal approach. The synthesis will be carried out without any used of capping ligands/surfactants or hazardous reducing agents if compared to preceding reports (Zheng et al., 2007; Warule et al., 2011; Wu et al., 2014; Chai et al., 2014; Dong et al., 2014). In conjugation with this, most of those studies reported that the temperature that used to synthesis heterostructures of Ag/ZnO composites is fallen within the range of 95 °C - 180 °C.

Also, capping agents are usually employed in order to obtain such a unique heterostructures. For instance, Chai et al. have added triethanolamine in their synthesis to induce the formation of Ag/ZnO heterostructures microspheres (Chai et al., 2014). Additionally, the reduction process of Ag^+ ions to form Ag nanoparticles normally involved additional reducing agents such as $NaBH_4$ and ammonia solution as reported by Wu et al. (2014) and Dong et al. (2014). However, in this research there is no additional reducing agents will be utilized, in fact Zn foil itself will act as reducing agent to reduce Ag^+ ions. This statement will be proven in the results and discussion section.

Moreover, current study also depicts the major contribution feasibly controlling the reaction time to fine tune the morphology of the Ag/ZnO nanocomposites through time-dependent crystallization process, where the initially form nanopillars is viable to be converted into hyperbranched ZnO during secondary hydrothermal treatment by the presence of Ag nanoparticles as catalyst. It is postulated that current synthesis approach can offer a potential route in producing nanostructures, which is simplified, facile and economically practicable.

1.5 Research Objectives

There are five main objectives of this research which are listed as follows:

I. To produce vertically aligned ZnO nanopillars on the Zn foil by using hydrothermal method at low temperature.
II. To sensitize Ag nanoparticles on the as-prepared vertically aligned ZnO nanopillars by using hydrothermal approach.
III. To characterize the properties of Ag sensitized ZnO photoelectrode by using Field Emission Scanning Electron Microscope (FESEM), High Resolution Transmission Electron Microscope (HRTEM), X-Ray Diffractometer (XRD), Raman Spectroscope, Photoluminescence (PL) and Diffuse Reflectance Spectroscope (DRS).
IV. To evaluate the performance of Ag sensitized ZnO photoelectrode via PEC water splitting application.
V. To analyze the PEC characteristic of Ag sensitized ZnO photoelectrode through Linear Sweep Voltammetry, Nyquist plot and Mott-Schottky plot measurement.

1.6 Organization of Chapters

Summarizing, this thesis is divided to seven chapters with Chapter 1 describes about the introduction of this research, the problem statement, rationale of research and the objectives of this research. Besides that, Chapter 2 explains about the literature review regarding to PEC applications as well as the overview on materials such as ZnO and Ag. Chapter 3 discusses about the methodology including the fabrication of sample and brief explanation about the characterization techniques that are utilized to analyze the properties and PEC characteristics of Ag/ZnO heterostructures.

In addition, the results ZnO nanopillars modification will be reported in Chapter 4 and further results and discussion of Ag sensitized ZnO heterostructures will be discussed in details in Chapter 5. The performance and study of PEC characteristics of Ag sensitized ZnO heterostructures will be further explained in Chapter 6. Finally, Chapter 7 discusses about the conclusions as well as the recommendation for future study in order to improve the results in this research.

CHAPTER 2: LITERATURE REVIEW

2.1 Introduction

Literature review is essential for researchers before starting any experiment because literature review helps them to gain ideas and to further know the technological development and existing limitation within the field of interest. Moreover, literature review also provides a guideline to the researchers so that the research will be more focus and obtain good findings.

This chapter discusses about the background study of PEC water splitting, their basic theory and mechanism. Furthermore, an overview of semiconductor and noble metal materials as well as the technique in fabricating photoelectrode will be briefly described.

2.2 The Energy Challenge and Sources

The world’s population is expected to keep increasing until at least mid-century and this indicates that the new inhabitants need water, food, shelter, transportation and consumer products, in which all of these require energy. In conjugation with this, one of the main challenges faced by the mankind energy shortage in order to meet the desired living creature. Statistically, the power consumption of the global population of nearly 7 billion people (in 2011) was 15 TW, and estimated to increase to 9 billion people with 30 TW power consumption by 2050 (Osterloh & Parkinson, 2011; Grätzel & Krol, 2012). Even though fossil fuels would be capable of meeting this energy demand, in which provide about 85 % of our energy supply and the reserve can sustain from 150 – 400 years for coil, 40 – 80 years for oil and 60 – 160 years for natural gases, but the burning of fossil fuels can be harmful to environment and human well-being (Grätzel & Krol, 2012).

The increasing of greenhouse gases, particularly CO_2 in the atmosphere, as a results of excessive combustion of carbon-based fuels has incurred serious Earth’s climate change and global warming. Since the revolution of industrial area, a CO_2 level in the atmosphere has risen from 280 – 394 ppm, and it is still rising by about 2 ppm/year. According to the International Panel on Climate Change (IPCC), a CO_2 level above 450 ppm carries a high potential in causing serious global warming by more than 2 °C (Boddy et al., 1968; Ogden & Williams, 1990; Grätzel & Krol, 2012). In order to overcome this problems and to reduce the dependence on fossil fuels, the large-scale transition towards renewable, carbon-free and sustainable sources of energy is urgently-needed. Table 2.1 shows the choices of sustainable energy sources with their respective global power generating.

Table 2.1: Overview in sustainable energy sources and global power generating (Resourced from Grätzel & Krol, 2012)

Energy source	Power (TW)	Remarks
Wind	4	Represents about 10 – 15 % of global technical potential for on- and off-shore installations
Hydroelectric	1-2	Remaining untapped potential is 0.5 TW
Geothermal	12	Only a small fraction can be exploited
Biomass	10	Needs 10 % of earth's land surface to be covered by switch grass
Nuclear	10	Requires construction of a 1 GW_{peak} power plant every 35 H for the next 40 years.
Solar	>20	Requires 0.16 % of the earth's surface to be covered with 10 % efficient solar cells which total solar power reaching the earth's surface is 120, 000 TW

According to Table 2.1, only solar energy has the potential to meet the prospected energy requirements in contrast to other sources. However, 816 000 km^2 of the earth's surface area has to be covered with 10 % efficient solar cells in order to generate 20 TW power from the sun, whereby this area is almost equal to the total surface area of combined France and Germany. In other analogy, one has to produce 650 m^2 solar cell panel per second, 24/7 for 365 days per year, for the next 40 years in order to generate 20 TW peak power (Osterloh & Parkinson, 2011; Grätzel & Krol, 2012). Thus, large-scale energy storage solutions need to be implemented and one of the most comprehensive solution is by storing solar energy in the form of chemical fuel. The examples of chemical fuel includes methane, methanol, gasoline, diesel, hydrogen and many more. All of these examples require a carbon sources except for H_2 gas. Although H_2 gas has the highest energy density of 143 MJ/kg, but it suffers from low volumetric energy densities (0.011 MJ/L) cause it quite difficult to store (Cook et al., 2010). In order to overcome this matter, H_2 gas can be stored in the form of high pressure storage containers (~700 bar), liquid cryo-storage or in clathrate hydrate cages. Besides that, H_2 gas also can be stored in the form of chemical bonds such as metal hydrides (MgH_2 and $LiBH_4$) (Grätzel & Krol, 2012).

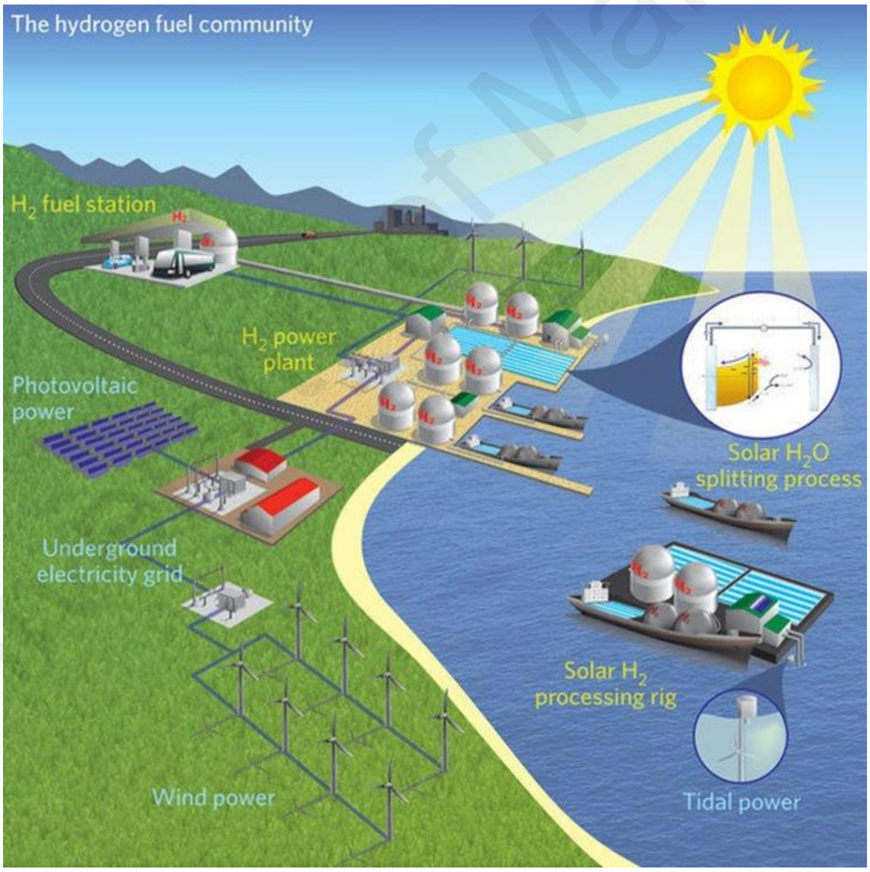

Figure 2.1: Illustration of implementation of a sustainable solar water splitting power plant (Resourced from Tachibana et al., 2012)

As well known, water is the most convenient and abundant source of H_2 gas. Grätzel and Krol (2012) stated that ~3.5×10^{13} L of water is required in order to store the energy in the form of H_2 gas for the world uses in 1 year (4.7×10^{20} J), in which corresponds to 0.01 % of the annual rain fall, or 0.000002 % of the amount of water in the world's ocean. Hence, the conversion of solar energy into H_2 gas via the splitting of water has become a promising method to tackle with the challenges of energy demand. In conjugation with this, Figure 2.1 illustrates the example of implementation of a sustainable solar water splitting power plant for clean, safe and efficient H_2 gas production and utilization. For the sake of reduction cost, the power plant involves the assistance of commercially available renewable energy sources such as wind, solar and tidal in order to aid in powering the plant. The generated H_2 gas can then be transported to fuelling stations for subsequent use in fuel cell, in engine and for electricity (Tachibana et al., 2012; Kibria, 2012).

2.2.1 Benefits of Solar Water Splitting Technology

H_2 gas production via solar water splitting technology is very beneficial in reducing the cost of daily lives. For example, one civil engineer in New Jersey, Strizki personalized his own home-energy system that consisted of 56 solar panels, electrolyzer (a device that uses electricity to break down water into H_2 and O_2 gases), 100 batteries for night time power and 10 propane tank (to store H_2 gas) as well as Plug Power fuel cell. He managed to generate 90 kWh of electricity on a typical summer day and consumed 10 kWh of electricity daily to run family's appliances, then the remaining 80 kWh of electricity was used for recharging the battery (which provided the electricity at night time) and powering the electrolyzer. With this kind of technology, he never paid for power bills anymore (Biello, 2008). Besides that, Shelton (2015) reported that the world's largest eco-friendly H_2 plant was opened in Germany which was capable in producing enough H_2 gas for around 2000 fuel-cell cars with an assumed mileage of 10,000 km [6,214 miles] per year. In addition to this, U.S.A is promoting home-grown fuel cell (an electrochemical device that combines H_2 and O_2 gases to produce electricity with water and heat as by-products) to enhance the economic growth and job development (Fuel Cell and Hydrogen Energy Association, 2015). In Malaysia, hydroenergy, fossil fuels, natural gas and biomass are mostly used as energy sources (https://en.wikipedia.org). Malaysia should be involved in solar water splitting technology and use H_2 gas as an alternative energy sources due to the energy demands and environmental issues.

There are many pathways exist to convert water and sunlight into H_2 gas such as photocatalytic water splitting, photoelectrochemical water splitting, coupled photovoltaic-electrolysis systems, thermochemical conversion and so on (Grätzel & Krol, 2012). However, this research are mainly focus on the study of PEC water splitting pathways.

2.3 Background Study on Photoelectrochemical Water Splitting

PEC water splitting idea was sparked since the discovery of the photoelectric effect by Edmond Becquerel, a French scientist (Grätzel, 2001). Hereafter, researchers and engineers have been infatuated with the idea of converting light into electric power or chemical fuels. In 1839, Becquerel’s pioneering photoelectric experiments were done with liquid, in which the illumination of solution that containing a metal halide salt produced a current between two platinum electrodes immersed in electrolyte. Becquerel’s experiment was motivated by photography whereby the first photographic images had made by Daguerre in 1837and followed with the silver halide process by Fox Talbot in 1839 (Grätzel, 2001). The formulation of silver halides emulsions became science only after the theoretical analysis were done by Gurney and Mott in 1938, in which sensitivity of photographic films can be detected. Since then, the sensitivity was recognized due to the semiconductor nature of the silver halide grains that possessed a band gap (Gurney & Mott, 1938). In 1883, Vogel discovered that silver halide emulsions could be sensitized by adding a dye and caused the photosensitivity extended to longer wavelengths. Four years later, Moser carried over the concept of dye enhancement from photography to PEC cells by using the dye erythrosine on silver halide electrodes (Grätzel, 2001). The modern photoelectrochemistry had been founded and changed from a mere support of photography to a thriving research direction on its own, was laid down by the study of Brattain and Garret (1938). Subsequently, Gerischer undertook the first detailed electrochemical and PEC studies on the semiconductor-electrolyte interface (Gerischer, 1966). Research on PEC cell became more active after the oil crisis in 1973, which stimulated a worldwide quest for alternative energy sources.

The investigations of PEC cell focused on two types of cell which is the first type was the regenerative cell, that converts light to electric power leaving no net chemical change behind. The second type was the photosynthetic cells which operates on the similar principle with the first type of cell except that there were two redox systems: one reacts with holes at the surface of semiconductor electrode and the second reacts with electrons entering the counter electrode. The overall reaction was used water and sunlight (Grätzel, 2001). In 1972, Fujishima and Honda implemented the concept of photosynthetic cells through the water photolysis of TiO_2 and this material has become a pioneer in PEC studies. They constructed an electrochemical cell, in which n-type TiO_2 semiconductor was connected with a 30 cm^2 surface area of platinum black electrode via an external load as depicted in Figure 2.2. Upon irradiation by 500 W Xenon lamp, current flowed the platinum electrode to the TiO_2 electrode through the external circuit. With respect to the direction of current flows, it was revealed that oxygen evolution reaction (OER) occurred at the TiO_2 electrode, while hydrogen evolution reaction (HER) occurred at platinum electrode. Fujishima and Honda managed to estimate the quantum efficiency to be approximately 0.1 (Fujishima & Honda, 1972).

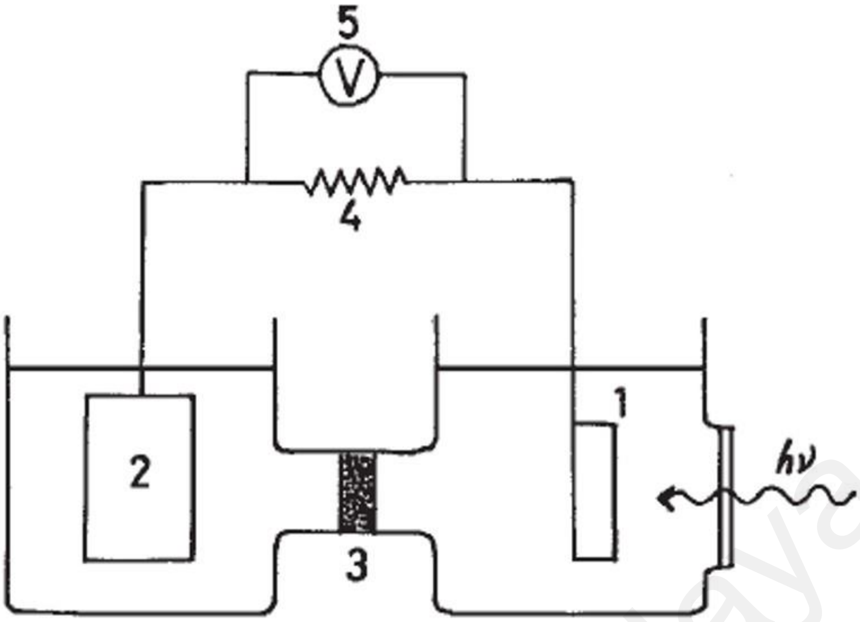

Figure 2.2: Design of electrochemical cell by Fujishima and Honda by using ~1 cm^2 surface area of TiO_2 electrode (Resourced from Fujishima & Honda, 1972)

In 1998, Khaselev and Turner demonstrated a PEC solar-to-hydrogen conversion efficiency of 12.4 % which combined the solar energy harvesting and water electrolysis into a single device (Khaselev & Turner, 1998). This highlights a great potential for PEC technology. In conjugation with this, PEC water splitting, also known as artificial photosynthesis can be defined as highly-efficient and eco-friendly approach to meet the energy demand via conversion of solar energy into chemical energy in the form of H_2 gas (Liu et al., 2013; Zhang et al., 2014).

PEC water splitting is a powerful, but complex process which several key criteria must be met simultaneously in order to decompose water into H_2 and O_2 gases efficiently and sustainably. The key criteria consisted of: (1) semiconductor must generate sufficient voltage upon illumination to split water; (2) bulk band gap must be small enough to adsorb a significant portion of solar spectrum; (3) band edge potentials at the surfaces must straddle the H_2 and O_2 redox potentials; (4) the system must exhibit long-term stability against corrosion in electrolytes and (5) charge transfer from the semiconductor surface to the solution must be facile to minimize the energy losses (Chen et al., 2013). In addition to this, the key component of PEC systems is the semiconductor photoelectrode that can fulfil the key criteria as mentioned before. With respect to the key criteria (2), photoelectrode should has band gap higher than 1.23 eV in order to split water efficiently. Semiconductor material especially metal oxides usually possess a large band gap (> 3 eV), which can only harvest UV portion of solar spectrum that consisted of only ~4 %. In order to enhance the solar to hydrogen conversion efficiency, tremendous effort has been made so that metal oxides can harvest the visible photons, since visible light accounts for ~46 % of solar irradiation (Zou et al., 2001).

Besides that, important point in the semiconductor photoelectrodes are the width of band gap and levels of conduction band (CB) and valence band (VB), in which the lowest-unoccupied CB should be more negative than the redox potential of H^+/H_2 (0 V vs NHE), while the highest-unoccupied VB level should be more positive than the redox potential of O_2/H_2O (1.23 V vs NHE). Figure 2.3 depicts the relationship between the band structure of various semiconductor and the redox potential of water splitting. The band structure is just a thermodynamic requirement but not a sufficient condition, therefore the band gap of visible-light driven photoelectrodes should be in the range of $1.23 \text{ eV} < E_g < 3.0 \text{ eV}$ (Kudo & Miseki, 2009).

Current study used ZnO as the photoelectrode since ZnO also gained great interest its high electrochemical stability, suitable valence and conduction band edges that straddle the redox potentials of water, high electron mobility (10-100 fold higher than TiO_2) (Dittrich et al., 1998; Klingshirn, 2007), absorption occurrence in the visible light region induced by the intrinsic defects, and lower recombination rates of charge carriers that arose from longer electrons and holes from the longer polaron decay lifetimes of ZnO (Quintana et al., 2007). As mentioned in previous chapter, the low photocurrent density and low photoconversion efficiency, resulting from the inadequate light absorption of

ZnO photoanode due to larger band dap are the main issues that hinder its practical application (Wei et al., 2012).

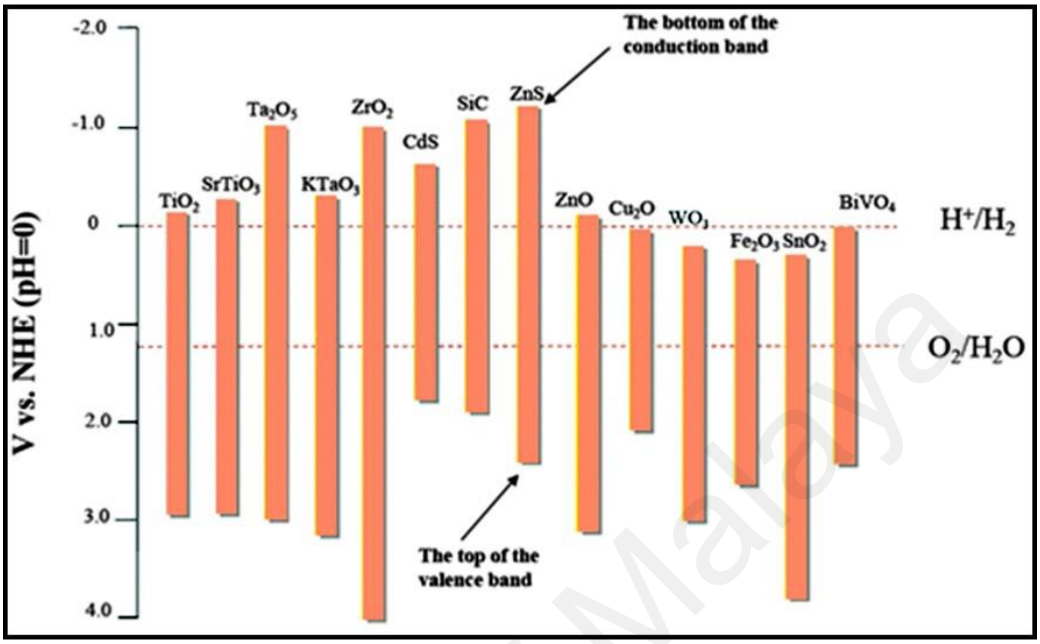

Figure 2.3: Relationship between the semiconductor band structures and redox potential of water splitting (Resourced from Yang et al., 2014)

Many strategies have been reported in order to enhance the photoconversion efficiency in a ZnO-based PEC cell such as reducing the size to the nanoscale to increase the specific surface area (Ahn et al., 2008; Wolcott et al., 2009), doping with different kinds of impurities to reduce the band gap and enhance the absorption of visible light (Hsu & Lin, 2012), sensitizing ZnO with dye or quantum dots (Unalan et al., 2008; Wang et al., 2010), producing solid solution of nitrides (Maeda et al., 2008; Maeda et al., 2009) and sensitizing ZnO with noble metal nanoparticles also is being explored to enhance light trapping (Wei et al., 2012). In this current work, sensitization with noble metal has been chosen due to the special property belong to Ag which is well known as SPR.

2.3.1 Basic Photoelectrochemical Test Setup

One of the key component in PEC that required careful consideration is a PEC setup. Usually, a general PEC setup contains a working electrode (WE) and counter electrode

(CE) (in two-electrode configuration) with an optional reference electrode (RE) (in three-electrode configuration). Plus, PEC system also need reservoir to hold the electrolyte, an optically transparent window that allows the illumination on sample, facilities to electrically connect the electrodes to the outside world, input and output for gas circulation system and/or gas purging as well as a membrane that separates anode and cathode compartments (to avoid mixing of evolved O_2 and H_2 gases) (Chen et al., 2013). Selection of CE, RE and electrolyte are another important parameters that need consideration in PEC setup.

2.3.2 The Counter Electrode Selection

In order to avoid performance limitations, the reaction at the CE should be fast and most importantly the WE itself should have a high catalytic activity. Platinum (Pt) is a common material choice for CE, which combines good chemical stability with small overpotential for H_2 gas evolution (~0.1 V). Ideally, the surface area of Pt should be at least two times larger than WE. Plus, both of CE and WE should be faced to each other symmetrically in order to avoid the inhomogeneous current densities at the WE. For the case of n-type semiconductor, H^+ is reduced to form H_2 gas via the HER at CE, so large surface area Pt foils or meshes can be a good CEs. In contrast, for p-type semiconductor, H_2O is oxidized to evolve O_2 gas via the OER at the CE, so Pt is not a suitable candidate since it is a poor OER catalyst. Oxides such as RuO_2 is much better CE and it can reduce overpotential if compared to the noble metals (Grätzel & Krol, 2012; Chen et al., 2013).

2.3.3 The Reference Electrode Selection

The applied potential is a key parameter when studying the properties of WE whereby this applied potential should be measured with respect to a fixed reference potential, so if there is any changes in the applied potential it will reflect a change in WE alone. The CE cannot be used for this purpose due to the unknown values of the overpotential at the CE/electrolyte interface and this overpotential is varied with the amount of current that flow through the cell. A third electrode should be added to the PEC cell which is well-known as RE in order to avoid the current-dependence (Grätzel & Krol, 2012). Table 2.2 shows an overview of commonly used RE in PEC water splitting research. Stability in the electrolyte solutions is an important selection criterion for a RE. Ag/AgCl electrodes are mostly used as RE and have largely replaced the traditional and environmentally less-friendly saturated calomel electrodes (SCEs) which is based on Hg/Hg2Cl2. In addition, Ag/AgCl can be generally used in a wide range of pH values (Grätzel & Krol, 2012; Chen et al., 2013).

Table 2.2: An overview of reference electrodes in PEC research (Resourced from Grätzel & Krol, 2012)

Reference electrode	Filling solution	Potential (vs SHE) at T=298 K
Reversible hydrogen	Actual electrolyte solution, purged with H_2 gas	0.0 – 0.059 × pH
Standard hydrogen (= normal hydrogen)	$[H^+] = 1.18$ mol.L^{-1} $p(H_2) = 10^5$ Pa	0.000
Silver/silver chloride (Ag/AgCl)	0.1 M KCl	0.2889
	1 M KCl	0.237
	3 M KCl	0.210
	3.5 M KCl	0.205
	Saturated KCl	0.198
	3 M NaCl	0.209
	Saturated NaCl	0.197
Calomel (Hg/Hg_2Cl_2)	0.1 M KCl	0.334
	1 M KCl	0.281
	3.5 M KCl	0.250
	Saturated KCl	0.242
	Saturated NaCl	0.236

2.3.4 The Electrolyte

The electrolyte in a PEC cell generally is a solvent that contained dissolved active species. In PEC water splitting, the active species and solvent are one and the same, which is water. Since the pure water is poorly conducting, additional ions must present in the solvent so that the desired current flow can be realized. In order to avoid the large Ohmic voltage losses across the electrolyte, the concentration of the supporting electrolyte should be sufficiently high. The type of dissolved ions and their concentrations are strongly influenced the electrolyte conductivity. At very high concentrations which is >1 M, the ion-pair formation may results in a decrement of the conductivity with concentrations (Grätzel & Krol, 2012; Chen et al., 2013).

Table 2.3: List of electrolytes that commonly employed in PEC test with respective materials (Resourced from Chen et al., 2013)

Material	Conductivity type	Electrolyte	Electrolyte concentration (M)	pH value
$GaInP_2$	p-type	Sulphuric acid	3	-0.5
WO_3	n-type	Phosphoric acid	0.33	1.28
	n-type	Sulphuric acid	0.5	0.4
$CuGaSe_2$	n-type	Sulphuric acid	0.5	0.4
InGaN	n-type	Carbonate buffer	-	10
a-SiN	n-type	Carbonate buffer	-	10
Fe_2O_3	n-type	Sodium hydroxide	1	13.6
	n-type	Potassium sulphate	0.5	2
Cu_2O	n-type	Sodium hydroxide	0.1	13
	n-type	Sodium acetate	0.1	7.4
TiO_2	n-type	Any	0.1	All
ZnO	n-type	Any	0.1	6.8

The electrolyte type such as acidic, neutral or basic should be selected to avoid the corrosion when the sample is immersed in the electrolyte. Even though the kinetics for driving HER and OER is lower at neutral pH if compared in acidic and alkaline media, but neutral electrolytes can be a good starting point if the material stability is unknown (Grätzel & Krol, 2012; Chen et al., 2013). Table 2.3 depicts the examples of electrolyte.

2.3.5 The AM 1.5 G Reference Spectrum

The main merit for PEC water splitting is its performance under real sunlight. However, the real sunlight does not have the same intensity and spectral distribution everywhere on the earth. The performance characteristics are usually quoted by using the so-called AM 1.5 G standard, which stands for “air mass 1.5 global” in order to facilitate the comparisons of performance in PEC water splitting. AM 1.5 G refers to the spectral distribution and intensity of the sunlight on a 37° south-facing tilted surface after travelled through 1.5 times the thickness of the earth’s atmosphere, which corresponds to a solar zenith angle of 48.19°. ASTM-G173-03 standard is the most recent and widely used AM 1.5 G reference spectrum (published by the American Society for Testing and Materials) and represents a reasonable average for the 48 contiguous states of the USA over a 1 year period (Grätzel & Krol, 2012).

Additionally, AM number represents the amount of atmosphere traversed in which AM 0 defines the spectrum outside the Earth’s atmosphere at 1 astronomical unit from the Sun, while AM 1 represents sunlight reach the Earth’s surface at the sea level when the Sun is directly overhead. AM 1.5 is chosen as the standard spectrum because it represents approximately the average annual AM value available at locations within the continental US (Chen et al., 2013). The AM 1.5 G spectrum includes the direct and diffuse contributions of the sunlight, where direct light is collected if looking via the tube towards the sun and can be concentrated, while diffuse radiation is the portion of illumination that has undergone forward scattering and cannot be concentrated (Chen et al., 2013). The AM 1.5 G spectrum has 90 % intensity of direct radiation and 10 % intensity of diffuse direction with total integrated intensity of 1000 W.m^2 (100 mW.cm^{-2}) (Murphy et al., 2006).

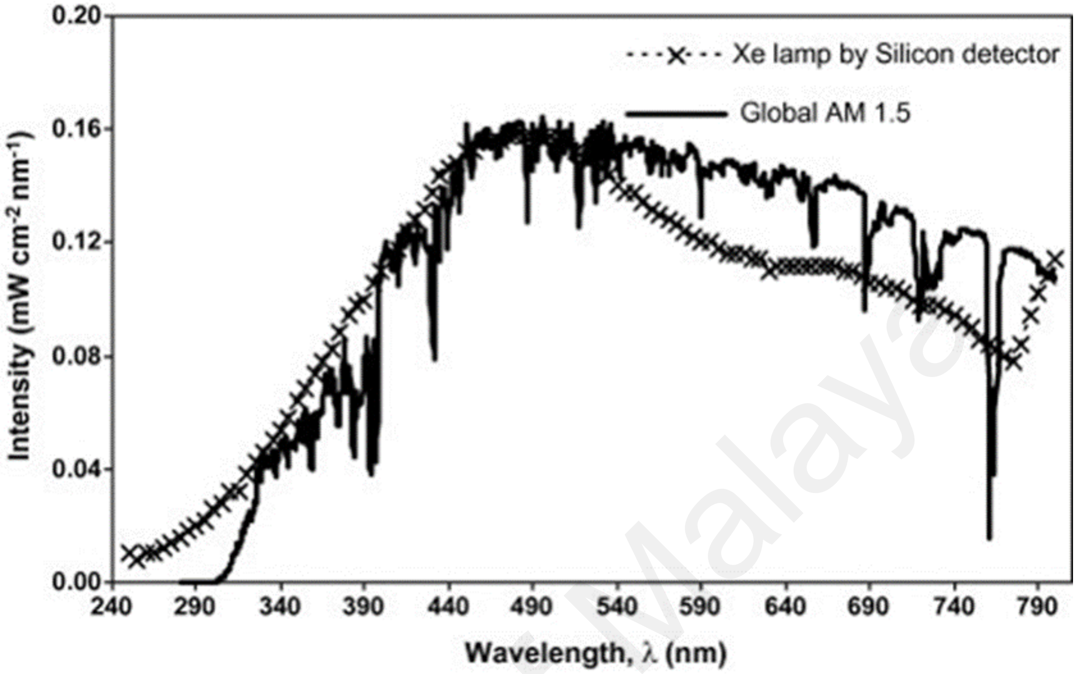

Figure 2.4: Spectrum of Xenon and AM 1.5 G (Resourced from Shaban & Khan, 2007)

Since real AM 1.5 G sunlight is not readily available all the times and at all locations, then solar simulator is highly recommended. Halogen lamps cannot be used since their maximum color temperature is limited to ~3200 K, which is much lower than the color temperature of the Sun (5800 K). In conjugation with this, Xenon lamps are widely accepted to give the best match to solar spectrum (Grätzel & Krol, 2012), whereby Figure 2.4 depicts the spectrum of Xenon and AM 1.5 G, respectively.

2.3.6 Basic Photoelectrochemical Water Splitting Mechanism

Since this research was utilized ZnO and Ag as research materials, then the mechanism of PEC water splitting is explained relating to the Ag/ZnO hybrid structure, whereby the schematic diagram of mechanism is demonstrated in Figure 2.4. Basically, the water splitting process to evolve H_2 and O_2 gases are following reaction mechanism (Zhang et al., 2014):

$$H_2O + 2h^+ \rightarrow 2H^+ + {}^{1}/_{2}\,O_2 \tag{2.1}$$

$$2H^+ + 2e^- \leftrightarrow H_2 \tag{2.2}$$

The PEC mechanism of Ag/ZnO photoelectrode can be explained regarding to the plasmonic sensitization theory which refers to a charge separation process that occurs at the interface between a wide-band gap of ZnO and intimately integrated Ag (Xiao et al, 2013). When Ag and ZnO are in contact to each other, the thermal equilibrium of Fermi level causes the downward bending of the CB of ZnO which therefore creates a potential barrier, namely the Schottky barrier. However, upon the solar irradiation of AM 1.5 G and under the resonant excitation of the SPR of Ag, a population of energetic electrons which are not in the thermal equilibrium with the lattice of Ag are generated. These energetic electrons that possess energies higher than the Schottky barrier can easily cross the barrier and inject to the CB of ZnO (Knight et al., 2011).

Simultaneously, under irradiation of solar, electrons are excited to the CB leaving holes in the VB and the space charge or depletion region is formed as well. The electric field in this region will cause the upward band bending of CB and VB of ZnO as well as promotes the separation of photogenerated electrons/holes as depicted in Figure 2.5. Therefore, holes will move towards the interface to perform the OER at WE and oxidizes water to O_2 gas, while photogenerated electrons as well as the migrated electrons from Ag will move to the interior ZnO and CE via the conducting Zn foil to perform HER and reduce water to form H_2 gas following the Equation (2.1) and (2.2). (Xiao et al., 2013; Zhang et al., 2014; Zhang et al., 2014). In addition, this process also generate the photocurrent density that contributed by the drift of electrons from photoanode through external circuit and reach Pt CE.

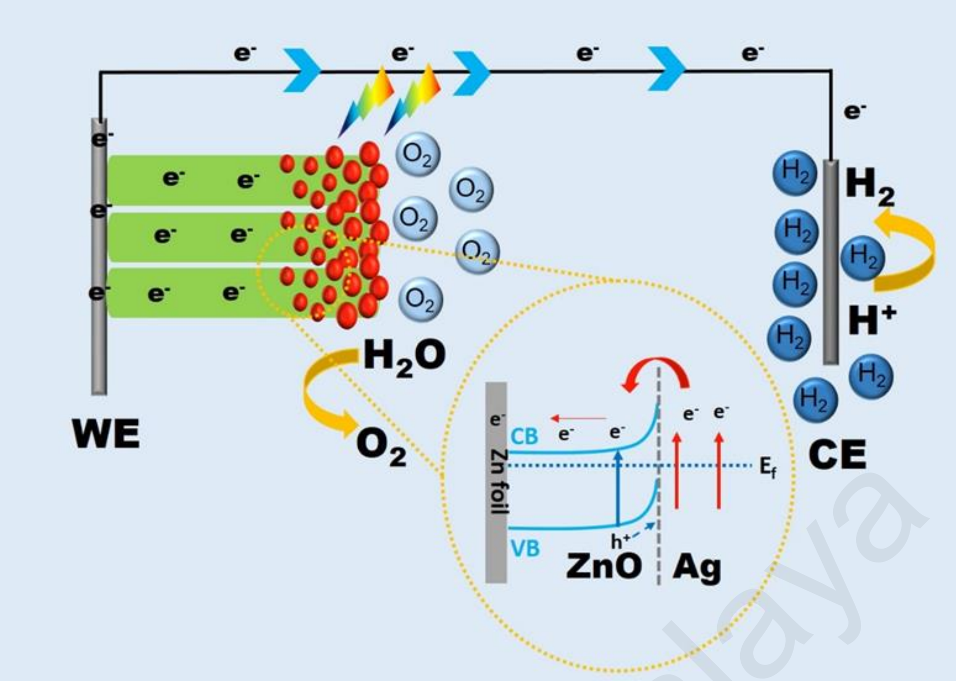

Figure 2.5: Schematic diagram of PEC water splitting mechanism of Ag/ZnO hybrid structure (Re-illustrated from Zhang et al., 2014)

2.4 Photoelectrode

In this research study, ZnO and Ag were used as research materials and it is essential to further understanding their crystal structure, general characteristics and structural as well as the optical properties.

2.4.1 Zinc Oxide

ZnO is an n-type semiconductor materials that has wide band gap of 3.37 eV and high electron-hole binding energy (60 meV) so that excitonic emission processes can persist at or above room temperature (Wang, 2008; Janotti & Chris, 2009). This has rendered the ZnO to be widely adopted as an important material in electronics, optics, optoelectronics, laser and light emitting diode (Jagadish & Pearton, 2006). The optical, piezoelectric and pyroelectric properties that owned by ZnO has made it a great candidate for sensor, transducer, energy generator and photocatalyst for H_2 gas production. Additionally, ZnO also is considered to be a green material that is biocompatible, biosafe, biodegradable and widely used in medical applications as well as in environmental science (Zhou et al., 2006; Zhou et al., 2008). ZnO is an II-VI compound semiconductor which has hexagonal wurtzite structure that belong to the space group $P6_3mc$ (Hermann-Mauguin notation) and C_{6v}^4 (Schoenflies notation), with two lattice parameters a = 0.3296 nm and c = 0.52065 nm in the ration of $c/a = \sqrt{8/3} = 1.633$. The crystal structures shared by ZnO are wurtzite, zinc blende and rocksalt, in which wurtzite symmetry is the most thermodynamically stable phase under the ambient conditions. Meanwhile, zinc blende structure can stabilized only by growth on cubic substrate and rocksalt structure may obtained at relatively high pressures, as in the case of GaN (Morkoç & Özgür, 2009). Figure 2.6 schematically shows the crystal structure of three phases of ZnO.

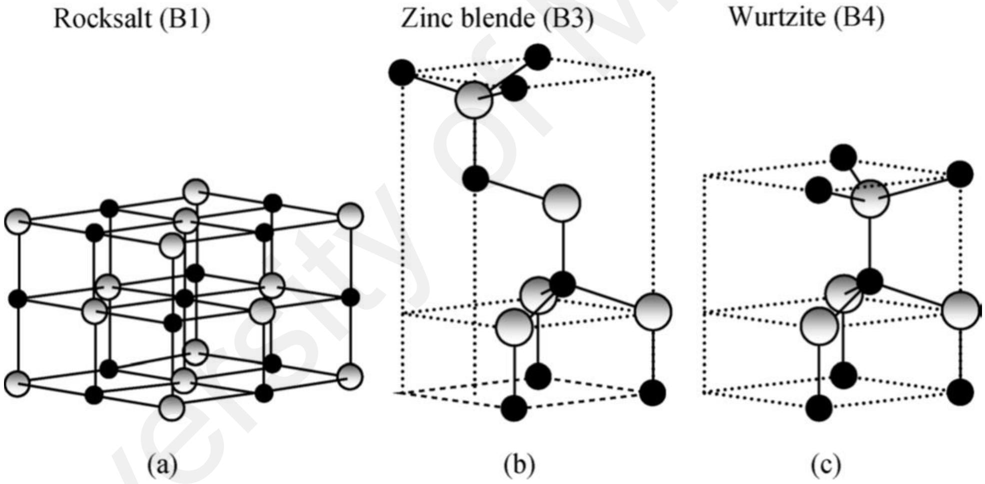

Figure 2.6: Crystal structure of (a) rocksalt, (b) zinc blende and (c) wurtzite for ZnO (Resourced from Morkoç & Özgür, 2009)

ZnO nanostructures are one of the most splendid families of nanomaterials that categorized under hexagonal phase wurtzite crystal structure, in which this wurtzite structure has two important characteristics includes non-central symmetry and polar surfaces. Basically, the structure of ZnO can be described as a number of alternating planes that composed of tetrahedrally coordinated O^{2-} and Zn^{2+} ions, whereby they are stacked alternatively in c-axis. The positively charged (0001) Zn and negatively charged $(000\bar{1})$ O polar surfaces result in a normal dipole moment and spontaneous polarization along the *c*-axis as well as a divergence in surface energy. The electrostatic interaction energy and distinct chemical reactions at the polar surfaces explain the formation of a wide range of unique nanostructures such as springs, rings, bows, ribbons, helices and so on (Wang, 2008).

2.4.2 Argentum

Ag is a chemical element that possess atomic number of 47 and exhibits the highest electrical conductivity, thermal conductivity and reflectivity among noble metal. Ag has long been identified as precious metal that frequently used in numerous of applications such as solar panels, water filtration, window coatings and in catalysis of chemical reactions. In periodic table, Ag is situated in group 11 alongside with copper and aurum, whereby its 47 electrons are arranged in the configuration of $[Kr]4d^{10}5s^1$. Ag crystallized in a face-centered cubic lattice with the crystal structure as depicted in Figure 2.7.

Additionally, as other noble materials, Ag also owns a unique characteristic which is well-known as surface plasmon resonance (SPR), where SPR phenomena is depended on several parameters. Among the parameters include shape, size, composition, and the interparticles geometry as well as spacing of the nanoparticles assembly (Huang et al., 2009; Sau et al., 2010). The collective oscillations of the free electrons give rise to large local electric field enhancements (strongly concentrated light intensities) upon the resonant excitation, whereby this intensity enhancements are maximal at the metal surface and decay away from the surface exponentially (Xiao et al., 2013).

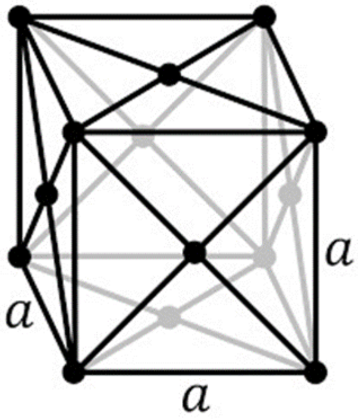

Figure 2.7: Face-centered cubic crystal structure of Ag (Resourced from http://wikipedia.com)

In addition, these intense electric fields are believed can amplify variety of optical signals such as Raman scattering (Ghosh & Pal, 2007; Porter et al., 2008), fluorescence (Pompa et al., 2006; Ming et al., 2009) and two-photon luminescence (Nevet et al., 2010). The plasmonic metal materials are widely used in optical devices such as data storage and photodetectors (Zijlstra et al., 2009; Knight et al., 2011). In solar energy harvesting, the incorporation of plasmonic metal can result in strong light confinement and increased light absorption, which finally leads to increment of power conversion efficiencies of dye-sensitized solar cells (DSSC) (Qi et al., 2011).

2.4.3 Hybrid Structure of ZnO

As mentioned before, incorporation or sensitization of noble metal and other materials onto the surface of ZnO can enhance the generation of H_2 gas as well as the photocurrent density production in PEC water splitting application. There are numerous of studies have been conducted by researches that incorporate other noble metal or other materials onto ZnO for enhanced PEC water splitting application and the examples can be summarized in Table 2.4.

Table 2.4: Summary of materials incorporated ZnO hybrid structure for PEC water splitting application

Sample	Substrate	Reference
3D branched Au/ZnO	FTO	Zhang et al., 2014
Ag/CdS/ZnO nanocomposite	ITO	Zhang et al., 2014
Au NP sensitized ZnO nanopencil	FTO	Wang et al., 2015
Cl-doped ZnO nanowires	FTO	Wang et al., 2014
ZnO/ZnS/CdS/$CuInS_2$ core-shell	FTO	Yu et al., 2014
ZnO/ZnS/Au sandwich structure	FTO	Liu et al., 2015
ZnO-CdSe core-shell	ITO	Miao et al., 2013
Reduced-graphene oxide/$Zn_{1-x}Ag_xO$ nanocomposite	ITO	Upadhyay et al., 2014
Ag nanoparticles decorated ZnO nanorods	PET	Wei et al., 2012
ZnO/$SrTiO_3$ nanoarrays	ITO	Guo et al., 2014
Pt nanoparticles /ZnO nanorods	ITO	Hsu et al., 2014
Si/ZnO core/shell nanowire	Si	Ji et al., 2013
Match-like ZnO/Au	Zn foil	Wu et al., 2014
N-doped ZnO	ITO	Yang et al., 2009
ZnO/Fe_2O_3 core-shell	FTO	Hsu et al., 2015
PbS sensitized ZnO nanowire	FTO	Li et al., 2016

Table 2.5: Price comparison of precursor salts based on Sigma-Aldrich Company

Noble metal	Purity (%)	Phase	Weight (g)	Price (RM)
Silver nitrate, $AgNO_3$	99.995	Powder	25	667.50
Gold (III) chloride trihydrate, $HAuCl_4$	99.9	Powder	25	11,275.00
Platinum (II) chloride, $PtCl_2$	99.9	Powder	25	37,937.50

Ease in fabrication and reduction of cost are one of the reasons why Ag was chosen (instead of Au or Pt) to be sensitized with ZnO. In conjugation with this, the price comparison of precursor salts that normally used to fabricate Ag, Au and Pt is demonstrated in Table 2.5. Besides that, the plasmonic effect that comes out from the SPR characteristic of Ag (if compared to other materials) was the other reason of choosing it to be sensitized with ZnO (even though Au and Pt also possess this SPR effect, but Ag is much cheaper). Plasmonic metallic nanostructures are characterized by strong interaction with the resonant photons via an excitation of SPR, whereby SPR can be described as the resonant photon-induced collective oscillation of valance electrons. The resonant photon wavelength is different for different metals. For instance, gold and silver exhibit resonant behaviour when they are interacting with ultraviolet and visible photons. Additionally, the resonant wavelength and SPR intensity not only depend on the nature of metal, but also on the shape and size of the metallic nanostructures. In the hybrid system for PEC application, a flux of photons is absorbed by a semiconductor to yield the high-energy charge carriers (electrons and holes). These charge carriers are separated from each other and diffused to catalytically active sites where they drive the chemical transformation. As a result, O_2 and H_2 are formed simultaneously (Linic et al., 2011).

2.5 Hydrothermal Route

The growth of ZnO with various morphologies of one-dimensional (1D) to three-dimensional (3D) ZnO nanostructures have been fabricated and studied by many researchers. For instance, Gu et al. (2009) reported the preparation of vertically aligned ZnO nanorod arrays by using oxidation method. More amazingly, they were able to synthesize sophisticated urchin-like ZnO nanorods superstructures by substituting the flat Zn foils with highly curve ZnO microspheres. Although the method applied by Gu et al. can produce such an intriguing ZnO nanoarchitectures, it was a high-energy consumption approach in which the temperature needed was as high as ~450 – 500 °C (Gu et al., 2009). Hydrothermal method is believed to be one of the synthesis method that possess the capability to systematically and creatively manipulate ZnO nanoarchitectures with diversified geometries. For example, synthesis of 3D firecracker-like of ZnO nanoarchitectures has been successfully produced by hydrothermal method as reported by Ma et al. (2015). The morphology of these 3D ZnO firecracker-like have been controlled at different reaction time via the assistance of surfactant with temperature as low as 60 °C (Ma et al., 2015). Due to its low cost, low synthesis temperature, ease in scaling up and environmental benign factors, hydrothermal route has continuously adopted by many researchers (Shi et al., 2013).

Hydrothermal route can be described as a synthesis method to form and grow the crystals via chemical reactions and the changes of substances solubility, in which heat is supplied in a tightly sealed aqueous solution above the ambient temperature and pressure (Feng & Xu, 2001; Cundy & Cox, 2003). Additionally, the key success of the preparation of inorganic semiconducting nanostructures is by precisely controlling over the hydrothermal synthetic conditions. Hence, the controllable conditions can be classified as the interior and exterior reaction system. The interior reaction system includes concentration, pH value, time, pressure, organic additives or templates, while exterior reaction environment conditions includes mode of input energy. Besides that, the strategies based on the interior reaction system can be categorized up to four types: (1) organic additive- and template-free hydrothermal reaction; (2) organic additive-assisted hydrothermal reaction; (3) template-assisted hydrothermal reaction and (4) substrate-assisted hydrothermal reaction. Whereas, the strategies based on the adjustment of exterior reaction environment still utilize the microwave-assisted and magnetic field-assisted hydrothermal synthetic approach (Shi et al., 2013).

In this research study, Ag/ZnO photoelectrode is grown by using hydrothermal method, where Zn foil is used as substrate. Conducting substrate is essential in PEC water splitting experiment to facilitate the electron migration to the CE. With respect to Table 2.4, fluorine-doped tin oxide (FTO) is the mostly used substrate to grow nanostructures.

However, facile fabrication (ZnO is directly grown on Zn foil) and price of Zn foil were the reason of selecting Zn foil as a substrate in this research study. The market price of the substrates is shown in Table 2.6.

Table 2.6: Price of substrate based on Sigma Aldrich Company

Substrate	Dimension (mm^2)	Price (RM)
Zn foil	50 × 50	234.00
Fluorine-doped tin oxide (FTO)	50 × 50	351.50
Indium-doped tin oxide (ITO)	50 × 50	1545.00

2.6 Other Fabrication Techniques of Ag/ZnO Hybrid

In this work, hydrothermal method has been chosen as a technique to fabricate Ag nanoparticles sensitized ZnO nanopillars and the reasons behind the choice had been discussed before. However, it is worth mentioning other fabrication techniques for the sake of knowledge and understanding. There are numerous techniques to fabricate Ag/ZnO hybrid, for instance, Li and his co-workers synthesized ZnO sea urchin-like on Zn foil by using chemical method that heated in an oven at 25 °C for 12 H. After that, Ag was deposited on the sea urchin-like ZnO via photochemical method and the reduction of Ag^+ ions was performed under sunlight during daytime (Li et al., 2013). Besides that, sophisticated structure of ZnO nanoflowers was successfully grown on a patterned sapphire substrate with a highly ordered hemisphere array via photolithography route and Ag nanoparticles were decorated on top of them by sputtering an Ag target with a radio frequency magnetron sputtering system at room temperature as reported by Tao and his colleagues (Tao et al., 2015).

Deng et al. reported about the preparation of ZnO mircorods via a solvothermal-assisted heat treatment method at 80 °C for 5 H and Ag nanoparticles were subsequently decorated onto the surface of as-prepared ZnO mircorods through solar light photoreduction method. A 500 W xenon lamp was used to reduce Ag^+ ions in ethylene glycol medium (Deng et al., 2012). The unique structure of nest-like ZnO decorated Ag nanoparticles were successfully fabricated as reported by Ding et al. They used two-electrode (Zn-Zn) system to produce nest-like structure of ZnO on Zn foil by applying electric potential of 3 V. Interestingly, a three-electrode configuration was used to integrate Ag nanoparticles on the nest-like ZnO. A Pt wire and Ag/AgCl electrode were served as counter and reference electrode, respectively. The working electrode was biased at -0.6 V in 0.001 M $AgNO_3$ solution for 1 min to held the Ag clusters which were conglomerated by Ag nanoparticles in the center of ZnO nest-like structures (Ding et al., 2013).

In 2015, He and his co-workers had used electrophoretic method to deposited Ag on the surface of ZnO. At first, they prepared ZnO nanorod arrays on a smooth Si wafer by chemical vapour deposition. Ag colloidal solutions were then prepared by using laser ablation of a silver metal target in DI water. The Ag metal plate was fixed below the water surface and was irradiated for 30 min with the first harmonic of a Nd:YAG pulsed laser. In order to perform the integration of Ag process, electrophoretic deposition was used in which, ZnO nanorod arrays was served as the cathode and was immersed into Ag colloidal solution. Then, electrophoretic deposition was further performed for 30 min at a DC voltage of 40 V (He et al., 2015).

Other techniques to synthesize Ag/ZnO hybrids are by using classical polyol process that had been reported by Liu et al. The Ag nanowires were firstly prepared by mixing the PVP, Na_2S and ethylene glycol and were added dropwise into solution of $AgNO_3$ in ethylene glycol. This mixture was heated in a microwave oven. The worm-like Ag/ZnO core-shell structure was then synthesized by preparing TEA and aqueous zinc acetate mixed solution. The specific volume of the as-prepared Ag nanowire suspension was then introduced into the previous mixed solution and these mixtures were ultrasonically stirred at 200 W and 20 MHz for 2 H (Liu et al., 2012). In research that has been done by Wu et al., they used simple hydrothermal method to fabricate ZnO nanorods and decorated with tunable Ag nanoparticles contents. They were firstly grown ZnO nanorods on Zn foil hydrothermally with the presence of DI water as well as the melted 1,6-hexanediamine and subsequently heated at 180 °C for 5 H. Then, the as-prepared ZnO was inserted into a mixture of PVP and $AgNO_3$ that was dissolved in the mixed solvent of ethylene glycol and DI water. The reduction and deposition process of Ag^+ ions were further performed hydrothermally at 180 °C for 3 H (Wu et al., 2013).

2.7 Summary

As an overall, the background of PEC water splitting and corresponding mechanism and basic theory, the active materials as well as technique to prepare photoelectrode have been explained and discussed. Chapter 3 will report on the photoelectrode preparation, characterization techniques and PEC experimental setup.

CHAPTER 3: METHODOLOGY

3.1 Introduction

Basically, this chapter describes sample fabrication by means of facile and low temperature of hydrothermal approach. A stepwise procedure in photoelectrode preparation will be clarified in details. In addition, characterization techniques used to analyze structural and optical properties of the as-prepared photoelectrode are well described. This chapter also explains about the setup of PEC system as well as the PEC characteristic.

3.2 Materials

All of the chemicals were used without any further purification. The materials or chemicals that had been used throughout all of the experiment are listed in Table 3.1 below:

Table 3.1: List of materials

Material / Chemical	Formula	Supplier	Roles
Zinc foil (0.25mm; 99.999 % trace metal)	Zn	Sigma Aldrich	Synthesis and fabrication
Silver nitrate	$AgNO_3$	Merck Millipore	
Zinc nitrate tetrahydrate	$Zn(NO_3)_2.4H_2O$	Sigma Aldrich	
Deionized water (18.2 MΩ cm; TOC≤5ppb)	H_2O	-	
Sodium sulphate	Na_2SO_4	R & M Chemicals	PEC application
Phosphate Buffer solution (pH 7)	-	Laboratory Chemicals	

3.3 Fabrication of Photoelectrode

The fabrication of Ag sensitized ZnO photoelectrode is divided into two stages; which is ZnO nanopillars was firstly direct grown on Zn foil, followed by the sensitization of Ag nanoparticles. The sensitization processes were carried out by varying the reduction period of Ag^+ ions and the concentration of $AgNO_3$ precursor. The details of sample fabrication will be further explained.

3.3.1 Synthesis of ZnO nanopillars on Zn foil

ZnO nanopillars were directly grown onto Zn foil by using facile and low temperature hydrothermal approach whereby the method was modified from the study reported by Luan and co-workers (Luan et al., 2011). Zn foil with dimension of 10 mm x 20 mm x 0.25 mm was firstly polished until mirror-like surface was obtained as shown in Figure 3.1(a). Then, Zn foil was sonicated in distilled water, followed by in ethanol for 10 minutes, respectively. Cleaned Zn foil was placed horizontally at the bottom of Teflon (volume: 50 mL) container containing 40 % (20 mL) volume of DI water. The Teflon was sealed in autoclave and further heated at 50 °C for 24 hours. The picture of Teflon and autoclave can be depicted in Figure 3.1(b). Finally, ZnO nanopillars on Zn foil was purified using distilled water, followed by ethanol and purged with N_2 gas to dry completely.

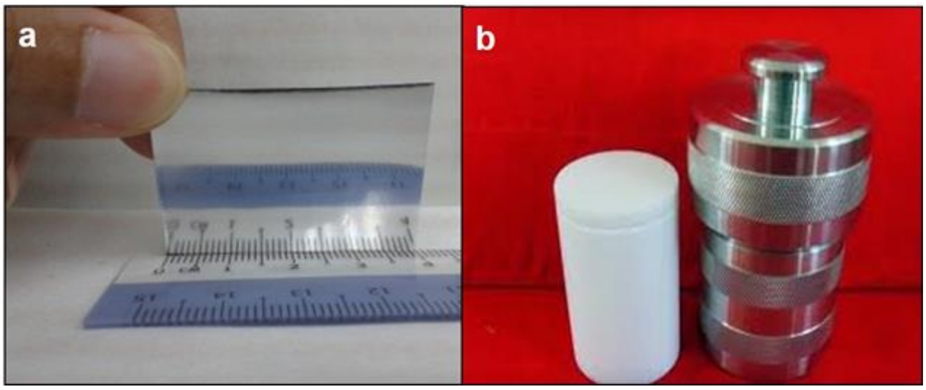

Figure 3.1: (a) Mirror-like surface of polished Zn foil and (b) 50 mL Teflon and autoclave

In order to obtain the desired pillar-like structure of ZnO, optimization of parameter such as temperature, duration, volume of DI water and heating rate was systematically conducted. All of the samples were characterized by using XRD and FESEM to obtain the desired structure. The best optimized parameter that produced ZnO nanopillars will be adopted for sensitization of Ag nanoparticles.

3.3.2 Synthesis of ZnO Nanostructures with Additional Zn Nitrate as Precursor

In addition, the effect towards the ZnO morphology also was studied when Zn salts were used as an additional precursors. 0.0654 g (12.5 mM) of zinc nitrate tetrahydrate ($Zn(NO_3)_2.4H_2O$) were weighted and dissolved in 40 % volume (vol.) of DI water. Next, the $Zn(NO_3)_2.4H_2O$ aqueous solution was poured into Teflon and Zn foil was placed horizontally at the bottom of Teflon. After that, it was further heated at 50 °C for 24 hours in 1°C.min^{-1} heating rate. The obtained sample was purified by distilled water and ethanol prior purging with N_2 gas to dry completely. After that, the vol. of 12.5 mM Zn nitrate was varied from 40 % - 80 %.

The effect towards the ZnO morphology through the variation of Zn nitrate aqueous solution concentration was also investigated. Sample with concentration of 12.5 mM is used as control sample and the concentration was varied from 3.125 mM – 18.75 mM. The procedure is similar with the previous method.

3.3.3 Sensitization of Ag Nanoparticles on ZnO Nanopillars

As mentioned earlier, the sensitization of Ag nanoparticles on the surface of ZnO nanopillars was conducted by varying two parameters such as the reduction period of Ag^+ ions and the concentration of $AgNO_3$ precursor. The sensitization process was carried out through two facile steps of hydrothermal approach whereby the temperature was fixed at 50 °C. The details of procedures will be discussed further as in section below.

3.3.3.1 Sensitization via the Reduction Period of Ag^+ ions

After the desired pillar-like structure was obtained, Ag nanoparticles were integrated on ZnO nanopillars by firstly preparing the stock solution of $AgNO_3$ aqueous solution. A weighed amount of $AgNO_3$ salt dissolved in DI water and stirred for a few minutes until the solution was uniformly mixed. 40 % vol. (20 mL) of 1 mM $AgNO_3$ aqueous solution was prepared by diluting the as-prepared $AgNO_3$ stock solution via equation below:

$$M_1V_1 = M_2V_2 \tag{3.1}$$

Here, M and V are respectively represent molarity and volume. The example of calculation for preparing $AgNO_3$ aqueous solution can be referred in Appendix A. Next, the as-synthesized ZnO nanopillars was placed horizontally at the bottom of Teflon container and 40 % vol. of 1 mM $AgNO_3$ aqueous solution was poured in to the Teflon. The reduction process of Ag^+ ions and the incorporation of Ag nanoparticles on ZnO nanopillars were executed under 50 °C for 30 minutes (min). The samples were then purified using distilled water and ethanol right after the reaction was done to terminate the Ag^+ ions reduction process. Subsequently, the as-obtained sample was dried by N_2 gas purging. The Ag^+ reduction period was varied from 30 min to 360 min and the samples were labelled as Ag/ZnO_30 min, Ag/ZnO_60 min, Ag/ZnO_120 min, Ag/ZnO_240 min and Ag/ZnO_360 min, respectively.

3.3.3.2 Sensitization via Different $AgNO_3$ concentration

The sensitization process was further studied by incorporating the Ag nanoparticles onto the ZnO nanopillars surfaces via the different $AgNO_3$ concentration. The synthesis procedures are similar with the previous parameter except the $AgNO_3$ concentration was varied from 5 mM to 0.2 mM. The samples were then named as Ag/ZnO_5 mM, Ag/ZnO_2 mM, Ag/ZnO_1 mM, Ag/ZnO_0.4 mM and Ag/ZnO_0.2 mM, respectively.

Since Ag nanoparticles were already formed at 30 min duration and to save the time consuming, the reaction period was then fixed at 30 min for all samples.

All of the as-fabricated photoelectrodes will be characterized by characterization tools and will be tested for PEC water splitting application to study their PEC characteristic as well as to quantify the photocurrent density production. The flow chart of Ag sensitized ZnO photoelectrode are shown in Figure 3.2.

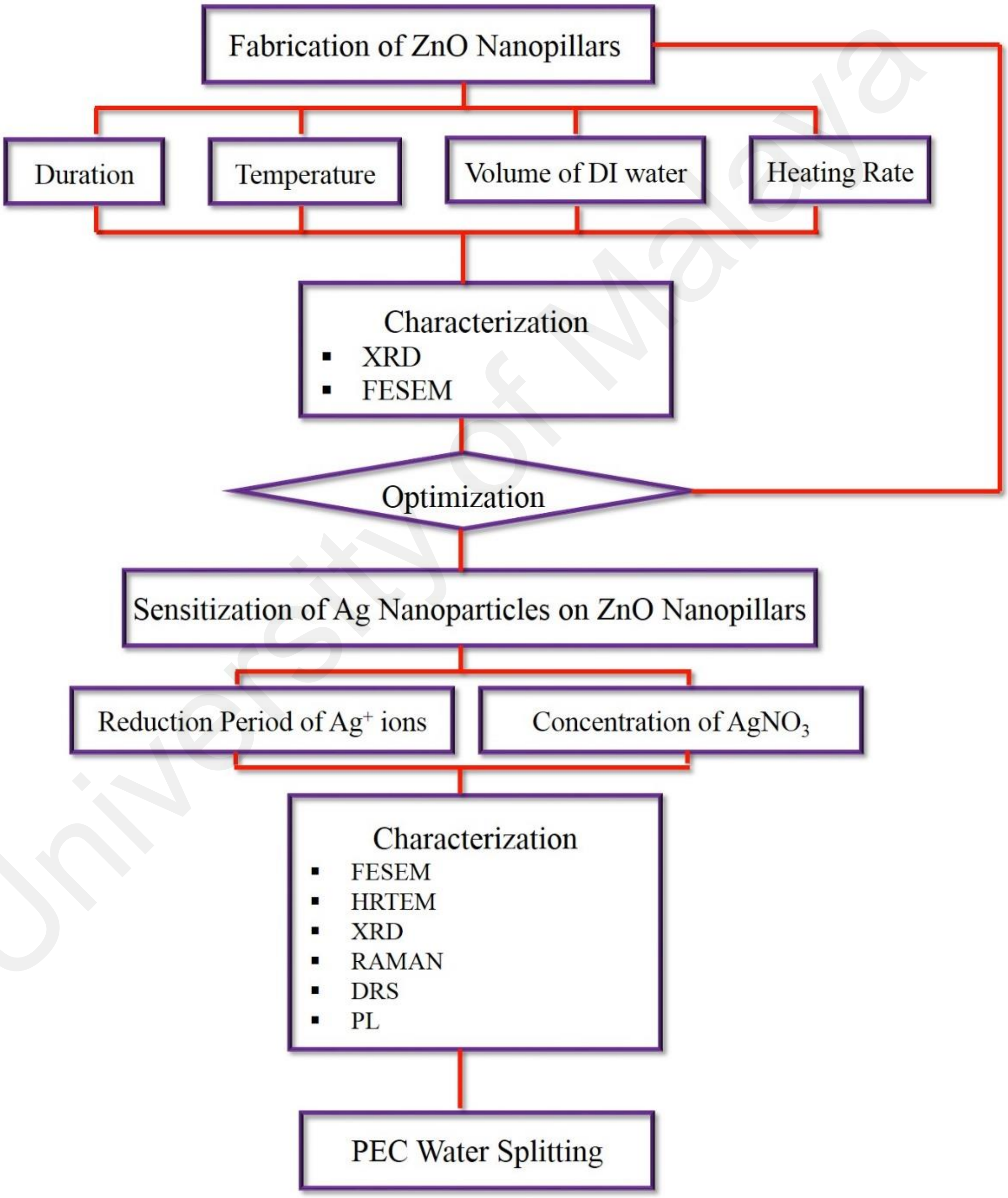

Figure 3.2: Flow chart of Ag sensitized ZnO photoelectrode

3.4 Characterizations

The morphology of as-prepared Ag sensitized ZnO photoelectrodes will be characterized by using field emission scanning electron microscopy (FESEM) and high resolution transmission electron microscopy (HRTEM). X-ray diffractometer (XRD) and Raman spectroscopy were used to analyze the crystallinity and structure of as-prepared photoelectrodes. The optical- and photoluminescence-properties of photoelectrodes will be identified by using diffuse reflectance spectroscopy (DRS) and photoluminescence (PL) spectroscopy. The PEC behaviour will be characterized via LSV, Nyquist plot and Mott-Schottky plot by using potentiostat and electrochemical impedance spectroscopy with combination of potentiostat. The working principle, sample preparation prior to characterization as well as the parameter used will be further explained later on.

3.4.1 Field Emission Scanning Electron Microscope

Nanotechnology fields such as semiconductors, catalysis, electronics, biotechnology and pharmaceuticals have strongly driven the development of recent electron microscopy, not only for the better resolution but for more information from the samples. Field emission scanning electron microscope, an abbreviation of FESEM in which works with electron instead of light. These electrons, so-called the particles with a negative charge are liberated by the field emission source. A FESEM is functioned to visualize fine topography details on the surface, entire or fractioned objects that may be as small as 1 nm (billions of mm) (Swapp, 2017).

Electrons that liberated from a field emission source will accelerate in a high electrical field gradient. Within high vacuum column, these primary electrons are focussed and deflected by electronic lenses to produce a narrow scan beam that bombards the object in which finally results in emission of secondary electrons from each spot on the object. The angle and velocity of the secondary electrons relate to the object's surface structures. The detector catches the secondary electrons to produce an electronic signal which will be amplified and transformed to a video-scan image that can be depicted on the monitor or to a digital image (Swapp, 2017).

Electrons are mostly generated by heating the tungsten filament (electron gun) whereby they are also produced by a crystal of lantanumhexaboride (LaB_6). The use of LaB_6 results in higher densities of electron and a better resolution if compared to that of conventional device. On the other hand, no heating but so-called “cold” source is employed in a FESEM. Additionally, a very sharp and thin tungsten needle which has an average tip diameter of 10^{-7} – 10^{-8} m functions as a cathode in front of primary and secondary anode. The acceleration voltage between cathode and anode is commonly in the order of magnitude of 0.5 – 30 kV. The generated image quality is markedly better due to the electron beam produced by the FE source is 1000 times smaller than in standard microscope (Swapp, 2017).

In this study, high angle backscattered secondary electron (HABSE) mode are utilized during the FESEM scanning. Backscattered electrons (BE) that emitted from the sample can be captured by at angles that closer to or farther from the direction of the incident electrons by changing the position of BE detector. The former is called HABSE, while the latter low angle backscattered secondary electrons (LABSE). The functions of HABSE are to detect compositional differenced (*Z* contrast), in which the higher the accelerating voltage the more information on the inner structure of the samples. Besides, it shows the crystal orientation from crystalline samples. However, HABSE mode has poorest spatial resolution. In addition to this, LABSE mode shows topography in which the information on compositional differences or on the inner structure of the sample. Similar to HABSE mode, it also shows the crystal orientation but has highest spatial resolution (http://www.jeolusa.com/RESOURCES/Electron). The morphology for all as-prepared samples in this study were inspected by using FESEM Hitachi (SU8000) and

JEOL (JSM 7600-F). The energy dispersive X-ray (EDX) mapping has also been carried out by using FESEM.

3.4.2 High Resolution Transmission Electron Microscope

High resolution transmission electron microscope (HRTEM) is an instrument to study the topographical, morphological, and compositional as well as crystallinity of nanomaterials. If compared to other microscope, HRTEM can simultaneously provide information in real space (imaging mode) and reciprocal space (diffraction mode). HRTEM can operate in Bright-field, Dark-field, SAED, High-resolution and CBED modes. HRTEM is coupled with a Gatan digital camera and this instrument can go up to a maximum magnification of 1.5 million. It has an anti-contamination device which assisted with liquid nitrogen to help the filament from contamination caused by volatile sample (Fultz & Howe, 2008; Williams & Carter, 2009).

By utilizing the focused beam of electrons (instead of light), information about the structure and composition of the sample can be achieved via HRTEM technique. An electron source, or so-called electron gun produces a stream of electron which is accelerated towards the specimen using a positive electrical potential. By using the metal apertures and magnetic lenses called “condenser lenses”, the stream is then focused into a thin and focused monochromatic beam. Next, the beam strikes the specimen and part of it will be transmitted through it. This beam will be focused again using a set of lenses called “objective lenses” into an image. This image is fed down the column via the “intermediate and projector lenses” whereby this image will be enlarged depends upon the magnification set. The image is produced by a phosphor image screen in which this image strikes screen and light is then endangered to enable the user to depict the image. The darker image represents the thicker or denser region of the sample (less electrons are transmitted), while the lighter image represents thinner region of the sample (more electrons are transmitted) (Fultz & Howe, 2008; Williams & Carter, 2009).

HRTEM can be operated in Scanning TEM (STEM) mode with Bright Field (BF) and High Angle Annular Dark Field (HAADF) detector. STEM is an amazing tool for characterization of nanostructures that provides elemental composition and crystal information at atomic scale. STEM works on similar principle as normal SEM except sample has to be prepared in ultrathin layer of 200 nm or less (except for nanoparticles) so that the accelerated beam of electrons pass through the sample. This electron beam interacts with TEM sample and detector in collecting the transmitted beam. When operating TEM mode, denser area that composed of heavy elements appear dark due to the more electron scattering within the sample. In contrast to TEM, in STEM mode the opposite is realized which makes HAADF detector very sensitive to differentiate irradiated element based on the atomic number (*Z* contrast) (Fultz & Howe, 2008; Williams & Carter, 2009).

The morphology and compositional of the as-prepared photoelectrode will be characterized by using HRTEM- JEOL (JEM-2100F) with an operating voltage of 200 kV. The as-synthesized photoelectrode was firstly scratched and dissolved in absolute ethanol, followed by placing a drop of colloidal sample solution on the mesh carbon-coated copper grid. The sample was then dried at ambient temperature prior observation under HRTEM.

3.4.3 X-ray Diffractometer

X-ray diffractometer (XRD) is one of the non-destructive tool to analyze the crystallinity and crystal phase for many kinds of matter, ranging from fluids, powders, crystals to thin films. This XRD technique uses X-ray diffraction on the sample in which diffraction occurs when the lights are scattered by a periodic array with long-range order, thereafter results in production of constructive interference at specific angles. The scattering X-rays from atoms produce a diffraction pattern that contains information about the atomic arrangement in crystal (Chauhan & Chauhan, 2014).

The electrons around the atom start to oscillate with the same frequency of the incoming beam when an X-ray beam hits the atom. In almost all directions, destructive interferences are formed which the combining waves are out phase causes no resultant energy is leaving the solid samples. However, the atoms in a crystal are arranged in periodic arrays that will result in the formation of constructive interference in which the waves are in phase and there will be a well-defined X-ray beams leaving the samples (Chauhan & Chauhan, 2014).

X-rays diffracted in phase will produce a signal whereby "in phase" means that the peak of one wave matches the peak of the following wave and diffraction only occurs when the distance travelled by the parallel X-rays are an integer of the wavelength. Bragg's law is simplistic model to understand the required condition for diffraction to be occurred and the equation is as follows:

$$n\lambda = 2d\,sin\theta \tag{3.2}$$

With a space, *d* between the planes for parallel planes of atoms, constructive diffraction occurs when Bragg's law is satisfied. Consequently, a planes produce a diffraction peak at specific angle θ and the sample is rotated so that the angle of diffraction changes. When angle is correct for diffraction, the signal will be recorded and converted into peaks subjected to the intensity of reflected signal. Additionally, the space between the diffracting planes of atoms will determine the peak positions (Henry et al., 2016).

The crystallinity and phases of the as-prepared samples were identified by X-ray diffraction (XRD) using PANalytical X-pert diffractometer (Empyrean) under powder scanning mode with the source of Cu K_α radiation (wavelength, λ = 0.154 nm) that was operated at 45 kV and 40 mA. The scan rate of 0.039°/s has been employed within the range of 30° - 75°.

3.4.4 Raman Spectroscopy

Raman spectroscopy was named in the honour of its inventor, C. V. Raman together with his mate (Raman & Krishnan, 1928). Raman spectroscopy is a scattering technique which is basically based on the inelastic scattering of incident radiation through its interaction with vibrating molecules (Bumbrah & Sharma, 2016). Sample is illuminated with a monochromatic laser beam which interacts with the molecules of sample and originates scattered light in which this scattered light that having frequency different from that of the incident light (inelastic scattering) is utilized to construct the Raman spectrum. The inelastic collision between incident monochromatic radiation and molecules of sample produce Raman spectra. When a monochromatic radiation strikes a sample, it scatters in all directions whereby this scattered radiation has a frequency equal to frequency of incident radiation and constitutes Rayleigh scattering (Willard et al., 1988; Smith & Dent, 2005).

On the other hand, only a small fraction of scattered radiation has a frequency that different from frequency of incident light which is constituted Raman scattering. Stokes lines appear in Raman spectra when the frequency of incident radiation is higher than the frequency of scattered radiation, while anti-stokes lines appear in Raman spectra when the frequency of incident radiation is lower than the frequency of scattered radiation (Willard et al., 1988; Smith & Dent, 2005).

The phonon vibration of the as-synthesized samples were collected using inVia Raman microscope (Renishaw) in which Argon laser at wavelength, λ = 514.5 nm with grating of 2400 lines/mm was employed. All of the measurement condition such as laser power

(100 %), exposure time (10 s) and accumulation (one) were kept the same to ensure that the comparison of the spectra can be done.

3.4.5 Diffuse Reflectance Spectroscopy

There are four possible phenomenon (absorption, transmission, reflection or scattering) occur when electromagnetic radiation in the UV/vis/NIR wavelength range interact with the sample. In order to measure the transmittance and absorbance of a transparent solid or homogeneous solution, typically UV/vs/NIR spectroscopy is utilized. On the other hand, reflectance spectroscopy is used for samples that are difficult to analyze by transmission measurement (Aydin et al., 2013). It is possible to measure the reflected and scattered energy from a sample when the spectrometer is equipped with the proper accessory such as integrating sphere.

When an integrating sphere is used in combination with spectrometer, they become a powerful tool in collecting and measuring specular and/or diffuse reflectance and capturing the scattered light from the sample as well. The external reflectance measurement can be divided into two types which is diffuse and specular reflectance. Diffuse reflectance is an excellent diagnostic tool for powdered, nanostructure and crystalline materials in different spectral ranges. Diffuse reflectance occurs when energy from the incident beam which penetrates one or more particles is reflected in all directions. The back reflected and diffusely scattered light are the collected and directed to the detector optics. Only the fraction of the beam that is scattered and returned back to the surface of the sample is considered as the diffuse reflection (Aydin et al., 2013).

The Kubelka-Munk theory is generally used for analyzing the diffuse reflectance spectra, following the method reported earlier (Aydin et al., 2013; Morales et al., 2008). The Kubelka-Munk equation at any wavelength become:

$$F(R) = \frac{(1-R)^2}{2R} \tag{3.3}$$

Where, R is reflectance. The energy band gap, E_g can be estimated by extrapolating the linear portion of the spectra to the *x*-axis (photon energy) in the graph of $[F(R).E]^2$ versus E, whereas E is the photon energy with an equation of:

$$E = \frac{hc}{\lambda} \tag{3.4}$$

Where, h is Planck constant, c is speed of light and λ is wavelength.

In this study, Diffuse Reflectance spectroscopy (DRS-Varian Cary-5000) equipped with an integrating sphere was utilized to measure the absorption of the as-prepared sample in UV-visible range.

3.4.6 Photoluminescence Spectroscopy

Photoluminescence spectroscopy is a non-destructive method of probing the electronic structure of nanostructures whereby the light is directed and absorbed by the sample. Excess energy is imparted into the material in the process called photoexcitation. This excess energy can be dissipated by the sample is via the emission of light or the so-called luminescence. In the case of photoexcitation, this luminescence is called photoluminescence. The photoexcitation process causes the electrons to excite to the permissible excited state. When these electrons return to their equilibrium state, the excess energy is then released in which may produce light emission (radiative recombination) or may not (nonradiative recombination) (Kumar, 2013).

An excitation wavelength is chosen by one monochromator and luminescence is observed via a second monochromator that usually positioned at 90º to the incident light in order to minimize the intensity of scattering light to reach the detector. Emission spectrum is produced if the excitation wavelength is fixed and the emitted radiation is scanned (Kumar, 2013).

In this research, by utilizing 325 nm He-Cd laser as excitation source, room temperature photoluminescence (PL) properties of the as-synthesized samples were characterized by inVia Raman spectroscope (Renishaw).

3.5 Photoelectrochemical Application

All of the as-prepared photoelectrodes will be further tested for PEC via water splitting process to inspect their performance on catalytic and electrochemical properties. The PEC characteristic as well as the setup will be explained in the following section.

3.5.1 Instruments and Apparatus

All of the instruments and apparatus that had been utilized throughout the PEC experiments is simplified in Table 3.2 as shown below:

Table 3.2: List of Instruments

Instruments	Characteristics	Supplier
Potentiostat/Galvanostat (Autolab – PGSTAT204)	Voltage = 100 – 240 V	Metrohm (Malaysia) Sdn. Bhd.
Electrochemical Impedance Spectroscopy (FRA32M) – in combination with PGSTAT	Frequency range = 10 μHz – 1 MHz Input range = 10 V	
Lamp power (Xenon) - 66901	Power = 50 – 500 W	Newport
Equipped with power supply - 69911	Power intensity = 100 mW.cm^{-2}	
Full reflector - 66215	To reflect wavelength from 200 – 2800 nm	
Air mass filter - 81094	-To provide real output of the xenon lamp to match better with solar spectrum - to meet AM1.5 G standard	

Table 3.2, continued

Platinum rod - 61248000	Thickness = 2 mm; length = 76 mm	Metrohm (Malaysia) Sdn. Bhd.
Equipped with shaft for plug-in electrode SGJ - 61241030		
Ag/AgCl electrode (F0DR-0021)	4M KCl w/AgCl reference filing	PINE Research Instrument
Ready-made design of a quartz-made photocell	Suprasil ® 300 quartz equipped with a flat optical window (window polish, standard: 60/40 scratch/dig)	PINE Research Instrument

3.5.2 Photoelectrochemical Water Splitting Measurement

Prior to the illumination onto the as-prepared photoelectrodes, the electrolyte solution was firstly prepared. 250 mL of 0.1 M Na_2SO_4 aqueous solution was prepared by diluting 3.551 g of Na_2SO_4 in 250 mL DI water. The solution was mixed uniformly and phosphate buffer solution was poured drop by drop to adjust the pH value to be 7.0. Edge of the photoelectrode was firstly scratched to ease the electrons flow from the sample to the CE. The alligator clip was then clipped on the scratched area and the edges as well as back area of the sample were applied with the epoxy to prevent the exposure of the electrolyte to the sample component (substrate and alligator clip). It is worth mentioning that the epoxy should be compatible with the electrolyte over the pH range used to test the photoelectrode. On the other words, the epoxy does not appreciably corrode or electrochemically leach the active compounds into solution along the test duration.

After the epoxy was dried, the sample was connected to the WE. The electrolyte solution was then poured in to the ready-made photocell and all the electrodes were mounted on the photocell as well. In this PEC experiment, Ag/AgCl electrode and platinum rod were used as a RE and CE, respectively. A 300 W Xenon arc lamp was mounted with the full reflector together with the air mass filter. Then, the light was perpendicularly projected onto the planar illuminated area of the photoelectrode by passing through the photocell window. The distance of the photoelectrode and arc lamp was kept 6.0 cm and all of the respective electrodes were connected to the potentiostat.

The potentiostat are compulsory to be calibrated by using the dummy cell prior to the PEC test. Finally, the PEC characteristics of the as-synthesized photoelectrodes will be tested by using linear sweep voltammetry (LSV) via potentiostat as well as by utilizing Nyquist plot and Mott-Schottky (MS) plot via electrochemical impedance spectroscopy (EIS) equipped potentiostat. The obtained spectrum were monitored on the screen and analyzed by NOVA 1.10 software. The results and analysis data of PEC will discussed later on in Chapter 6. Figure 3.3 shows the PEC setup and respective electrodes used along the duration test.

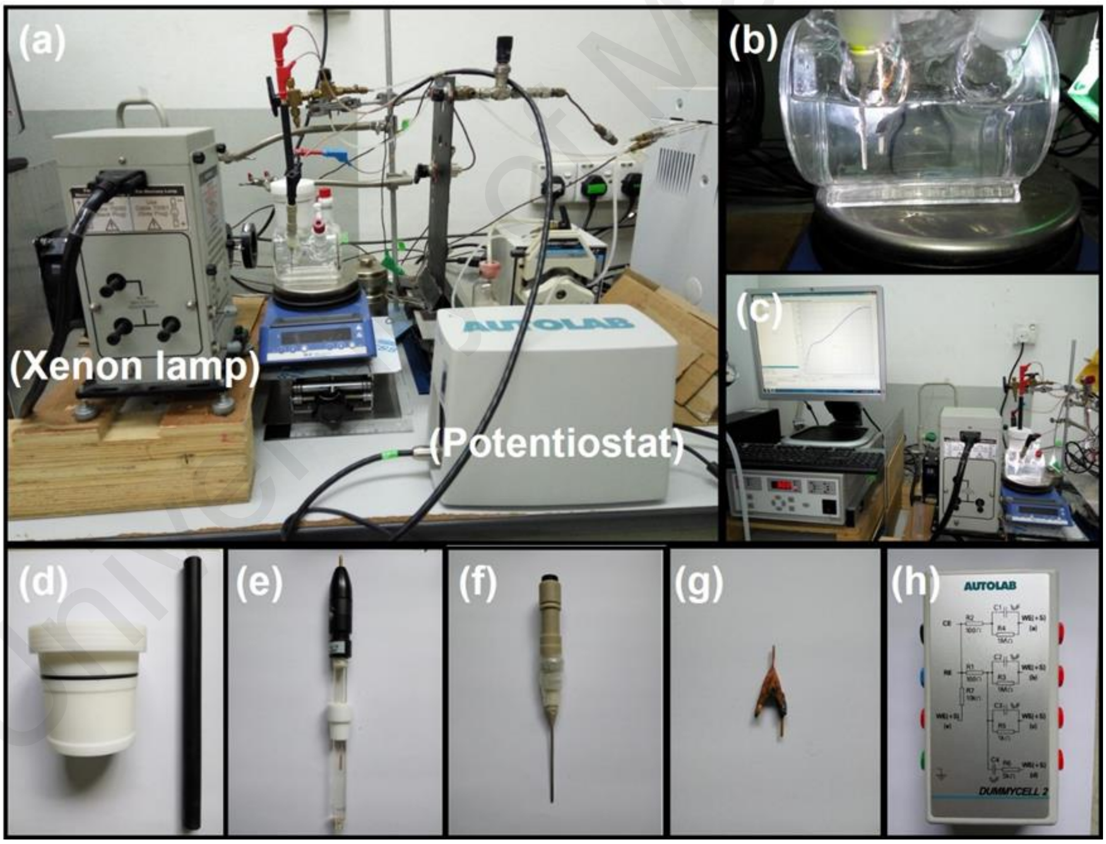

Figure 3.3: (a) PEC setup, (b) close up of PEC photocell with light is directed to sample, (c) spectra of I-V curve is monitored on the screen, (d) working electrode and holder, (e) Ag/AgCl reference electrode, (f) platinum counter electrode equipped shaft, (g) alligator clip and (h) dummy cell to calibrate potentiostat

3.5.3 Linear Sweep Voltammetry

Linear sweep voltammetry is a voltammetric technique whereby the potential between the photoelectrode (WE) and RE is linearly swept as a function of time with current is recorded simultaneously. The potential is scanned starting at the initial potential and will be stopped at the final potential. In addition, LSV is widely used to characterize the performance of photoelectrodes such as open circuit voltage (V_{oc}), short-circuit current (J_{sc}), fill factor (*ff*) and light to hydrogen efficiency (Xu et al., 2013). Scan rate plays an important role in LSV measurement in which higher scan rate will cause the thickness of the diffusion layer decreases if compared to the slower scan rate. Consequently, the ionic flux towards electrode surface related to the current density will be increased (Prasad & Sangaranarayanan, 2013).

As the molecules on the surface of WE are oxidized, they will move away from the surface and new molecules will come into contact with the surface of WE. This flow of electrons out of WE causes the generation of current. The current is a direct measure associated to the scan rate at which electrons are being exchanged via the electrode-electrolyte interface. The current will reach a plateau or exhibits peak when the rate of electron exchange is higher than the rate of the oxidizing species can diffuse from the bulk of the electrolyte to the surface of the electrode (Prasad & Sangaranarayanan, 2013).

In this LSV measurement, photoelectrode was scanned at potential range of -1.5 V – 0.5 V versus Ag/AgCl with scan rate is fixed at 5 mV.s^{-1} and no bias potential was applied. The measurement of LSV was executed in the dark and illuminated condition. Then, the photocurrent density against potential (versus Ag/AgCl) was plotted and analyzed.

3.5.4 Photoconversion Efficiency

The photoconversion efficiency is one of the important criteria for PEC study, where all of the photogenerated electrons and holes that involve in the redox process during water splitting will be evaluated. The overall solar-to-hydrogen efficiency can be estimated by using below equation (Chen et al, 2013):

$$\eta = I \left(\frac{1.23 - V_{app}}{P_{light}}\right) \tag{3.5}$$

Where V_{app} is an applied external potential versus RHE, I is the externally measured current at V_{app} and P_{light} is the power density of the incident light. The value of 1.23 V basically represent redox potential, V_{redox} based on a Gibbs free energy change for water splitting of 237 $kJ.mol^{-1}$.

The value of the photocurrent density, J_{ph} can be obtained from the I-V graph which is measured from the LSV measurement. Since the potential is measured versus the Ag/AgCl reference electrode, the conversion to the reversible hydrogen electrode (RHE) can be done by using Nernst equation (Hoang et al., 2012; Zhang et al., 2014):

$$E_{RHE} = E_{Ag/AgCl} + E^{o}_{Ag/AgCl} + 0.059pH \tag{3.6}$$

E_{RHE} is the converted potential versus RHE, $E_{Ag/AgCl}$ is the potential measured against the Ag/AgCl reference electrode and $E^{o}_{Ag/AgCl}$ is the standard electrode potential of Ag/AgCl reference electrode (0.1976 V versus RHE at 25 ºC).

3.5.5 Nyquist Plot

Electrochemical impedance spectroscopy (EIS) is one of the powerful diagnostic approaches to investigate the charge transfer kinetics at photoelectrode/electrolyte interface in PEC water splitting reaction. It also can be used to characterize the limitations and improve the performance of fuel cell as well (Liu et al., 2016; Ren et al., 2016). In addition, EIS provides information on the capacitive behaviour of the system, may be able to distinguish between two or more electrochemical taking place and can identify the diffusion-limited reaction. In order to perform the EIS measurement, a small sinusoidal perturbation (potential or current) of fixed frequency is firstly applied. With an application of small sinusoidal perturbation, pseudo-linear system will generate or else if the system is non-linear, the current response will contain harmonics of the excitation frequency (Barsoukov & Macdonald, 2005).

EIS data can be presented as a Bode plot or Nyquist plot whereby unlike the Nyquist plot, the Bode plot does show the frequency information. Figure 3.4 depicts the Nyquist plot and Bode plot, respectively. The results obtained from the Nyquist plot can be fitted into the RC circuit, which is so-called Randles circuit as shown in Figure 3.4(c).

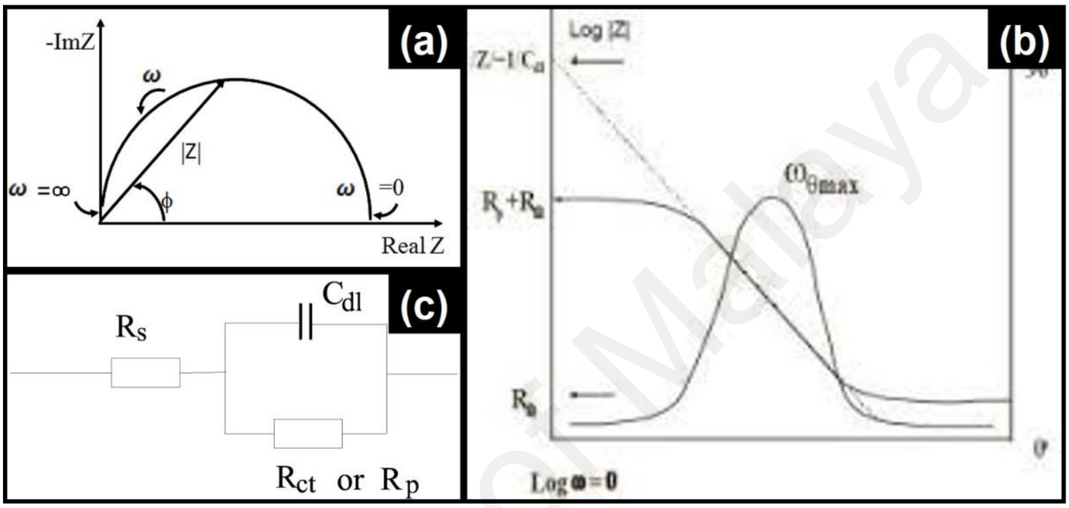

Figure 3.4: (a) Nyquist plot, (b) Bode plot and (c) Randles circuit (Barsoukov & Macdonald, 2005)

Electrical resistance is the ability of a circuit to resist the electrical current follow which obeys the Ohm’s law:

$$V = IR \tag{3.7}$$

Where, V, I and R define voltage, current and resistance, respectively. This relationship only apply in ideal resistor. However, in the real world of electrochemistry process circuit exhibits much more complex behaviour. Hence, impedance seems to suit in the real condition of circuit. The excitation signal can be expressed in a function of time as follows:

$$E_t = E_\circ sin(\omega t) \tag{3.8}$$

E_t is the potential, E_0 is the amplitude of the signal and ω is the radial frequency. The relationship between radial frequency and frequency can be expressed as:

$$\omega = 2\pi f \tag{3.9}$$

In a linear system, the response signal, I_t is shifted in phase (φ) that has a different amplitude, I_0:

$$I_t = I_0 \, sin(\omega t - \varphi) \tag{3.10}$$

Hence, the impedance can be expressed analogous to Ohm’s law as:

$$Z = \frac{E_t}{I_t} = \frac{E_0 \, sin(\omega t)}{I_0 \, sin(\omega t - \varphi)} = Z_0 \frac{sin(\omega t)}{sin(\omega t - \varphi)} \tag{3.11}$$

By applying Euler relationship,

$$exp(j\varphi) = cos \, \varphi + j \, sin \, \varphi \tag{3.12}$$

Then, the impedance can be possibly expressed as a complex function where, the potential is described as:

$$E_t = E_0 \, exp(j\omega t) \tag{3.13}$$

And current response as:

$$I_t = I_0 \, exp(j\omega t - \varphi) \tag{3.14}$$

Therefore, the impedance can be expressed as a complex number:

$$Z(\omega) = \frac{E}{I} = Z_0 \, exp(j\varphi) = Z_0 \, (cos \, \varphi + j \, sin \, \varphi) \tag{3.15}$$

Z(ω) is composed of real and imaginary in which if the real part is plotted on the *x*-axis while the imaginary part is plotted on the *y*-axis, Nyquist plot will be produced as shown in Figure 3.4(a).

In the EIS measurement to generate the Nyquist plot, the applied frequency was set from 100 KHz – 10 Hz with 0 V bias potential and the sinusoidal potential was fixed at 10 mV.

3.5.6 Mott-Schottky Plot

Mott-Schottky (MS) plot is one of the EIS technique that can provide an information and estimation of flat band potential, E_{fb} and the free charge carrier density (donors or acceptors), N_D of the photoelectrode. Additionally, N_D also plays a role in the bulk and surface semiconductor properties such as the width of the depletion layer and rate recombination. The conductivity type can also be revealed by MS plot in which the n-type materials will possess a positive slope while p-type materials will produce a negative slope (Gratzel & Krol, 2012; Chen et al., 2013).

Basically, the MS plot relationship involves measurement of the capacitance of the space charge layer, C_{sc} of the semiconductor electrode as a function of applied potential, E and can be expressed as (Ren et al., 2016):

$$\frac{1}{C_{sc}^2} = \frac{2}{\varepsilon\varepsilon_0 e A^2 N_D}\left[E - E_{fb} - \frac{kT}{e}\right] \tag{3.16}$$

Where; ε is the dielectric constant of the semiconductor, ε_0 is the permittivity in vacuum (8.85×10^{-14} F.cm^{-1}), e is the charge of electron, N_D is the free carrier density, k is Boltzmann constant, T is the temperature and E is an applied potential. The derivation of MS equation can be referred in Appendix B.

The value of E_{fb} is determined by the extrapolation of x-axis in MS plot ($1/C^2_{sc}$ versus E) at various frequency. In addition, the value N_D can be determined from the slope of MS plot by an equation (Yang et al., 2009):

$$N_D = \frac{2}{\varepsilon\epsilon_0 A^2 e}\left[\frac{d}{dV}\left(\frac{1}{C^2}\right)^{-1}\right] \tag{3.17}$$

The example for N_D calculation can be referred in Appendix C. In MS plot measurement, an applied potential was set to the range of -0.5 V – 0.5 V with the used frequency was 1000 Hz and the potential is plotted against to normal hydrogen electrode (NHE) via equation (Yang et al., 2009):

$$E_{NHE} = E_{Ag/AgCl} + 0.1976V \tag{3.18}$$

A detailed energy band diagram for a complete PEC cell can be drawn, whereby Figure 3.5 shows a cell composed of an n-type photoanode and a metal counter electrode. Usually, the *y*-axis represent the energy of an electron at a certain point *x* in the cell, whereby the energy of an electron in vacuum at infinite distance is chosen as a reference. At the electrolyte phase in Figure 3.5, the energy of the redox couple in an electrolyte with respect to the vacuum level ($e\phi_R*$) is not accurately known. Theoretical and experimental estimate that the H_2/H^+ standard redox energy located between 4.3 and 4.85 eV below E_{vacuum}. Since there is no electric field is assumed to be present in this phase, the vacuum level is drawn as a horizontal line in the electrolyte. This assumption is realistic for most water splitting application because highly concentration of electrolytes are frequently used in order to avoid the Ohmic voltage losses. For the case of a very low electrolyte concentration (<0.1 M), there may be insufficient ions are available at the outer Helmholtz plane to balance all the adsorbed charges at the semiconductor surface. Finally, all of these charges are then compensated in a region beyond the outer Helmholtz layer (Bockris et al., 2011).

The band positions, the amount of band bending and the difference between E_c and E_f are the key parameters for the semiconductor. The energy band diagram can directly show whether a certain reduction or oxidation reaction at the semiconductor surface is thermodynamically possible. As depicted in Figure 3.5, holes will be able to oxidize water if the H_2O/O_2 redox energy is located above the top of the valance band. Similarly, electrons with an energy above the redox energy can reduce the H^+. Additionally, the power of reduction and oxidation can be determined by measuring the potential (i.e., Fermi level) of the semiconductor with respect to that of reference electrode. The utilization of reference electrode is beneficial because the measured potential difference does not depend on the amount of current flows through the cell. In contrast, the potential difference between semiconductor and metal electrode depends on V_H at the metal electrode. The structure of Helmholtz layer at the metal/electrolyte interface is similar to the semiconductor, and the capacitance is also in the order of 10 – 20 μF.cm^{-2} (Gratzel & Krol, 2012).

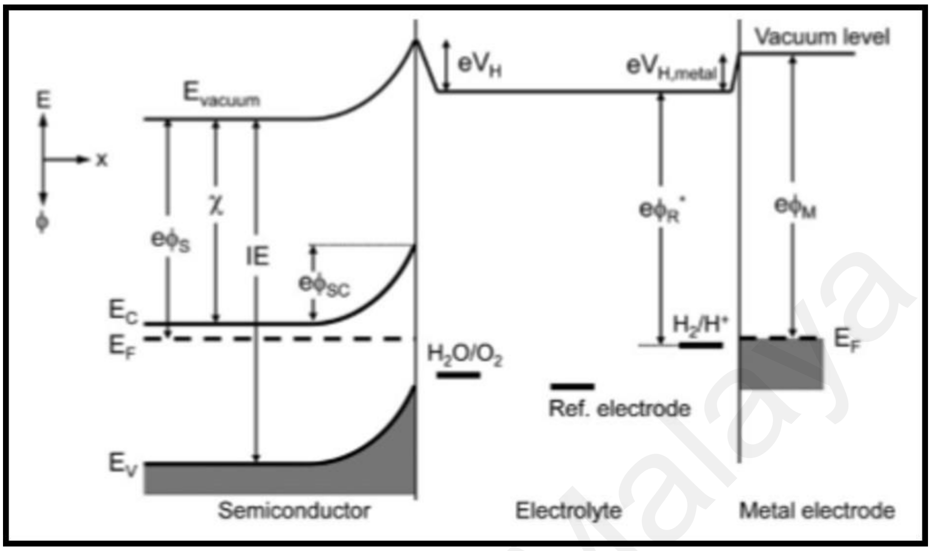

Figure 3.5: Energy band diagram for a PEC cell that consisted of n-type semiconductor and a metal counter electrode (Gratzel & Krol, 2012)

3.6 Summary

The procedure of photoelectrode fabrication, the characterization tools that were used to study the properties of photoelectrode as well as the PEC setup and measurements have been explained briefly in this chapter. The results will be further discussed in the Chapter 4-6.

CHAPTER 4: OPTIMIZATION OF ZINC OXIDE MORPHOLOGY

4.1 Introduction

Chapter 4 discusses about the optimization that had been conducted in order to obtain the desired pillar-like ZnO morphology. Series of experiments had been executed including varied the parameter such as temperature, duration, vol. of DI water and heating rate. This chapter also explains about the effect towards the ZnO morphology when Zn salts were used as precursor. All of the samples were characterized by using XRD and FESEM to analyze their composition and morphology, respectively.

4.2 Morphology Optimization via Reaction Temperature

The procedure to synthesize ZnO nanostructures can be referred in Chapter 3 in which ZnO was hydrothermally grown with varied reaction temperature. Other parameters such as reaction duration, vol. of DI water and heating rate were fixed for 24 H, 40 % (20 mL) vol. of DI water and 5 °C.min^{-1}, respectively. Figure 4.1 depicts the morphology of ZnO nanostructures grown on Zn foil when temperature was varied from 50 °C – 200 °C. As shown in Figure 4.1(a), it is observed that flower-like structures are formed and grown on the tips of rod-like ZnO nanostructures when Zn foil was heated at 50 °C. Interestingly, when reaction temperature was increased to 100 °C, the flower-like disappeared and the rod-like structures were further grown with smooth- and tapered-terminated tips.

At 150 °C, the rod-like structures were getting longer with long and sharp tip rods were lying horizontally on the vertical ZnO nanorods as shown in Figure 4.1(c). There was no much different on the morphology transformation when reaction temperature was increased to 180 °C, except the length of horizontal ZnO nanorods were getting longer and some of them formed branch rod-like structures. Finally, at 200 °C all of the horizontal ZnO nanorods were transformed to larger flower-like structures that located on the tips of vertical ZnO nanorods as depicted in Figure 4.1(e).

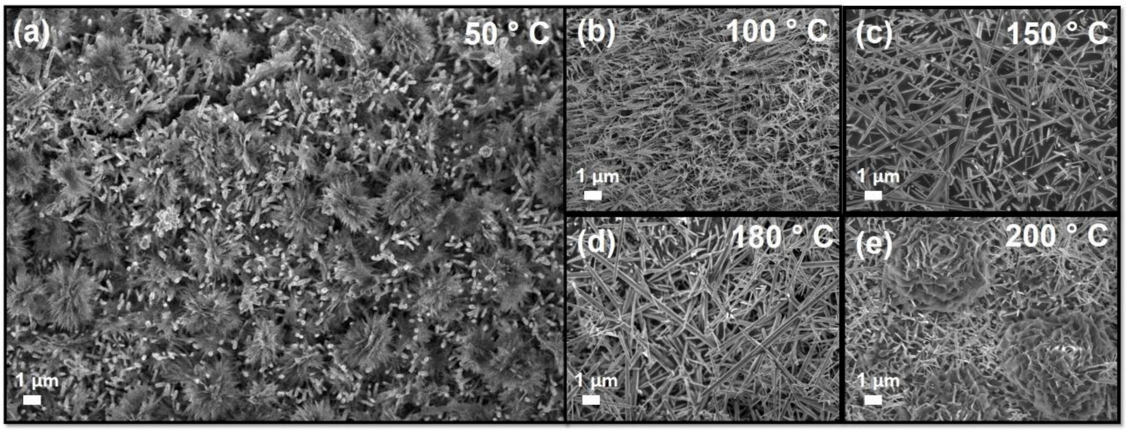

Figure 4.1: FESEM morphology of ZnO nanostructures at varied temperature: (a) 50 °C, (b) 100 °C, (c) 150 °C, (d) 180 °C and (e) 200 °C

The phase composition and crystal structure of ZnO nanostructures with varied reaction temperature are revealed by XRD as demonstrated in Figure 4.2. All of the samples were well-crystallized and can be perfectly indexed to the hexagonal wurtzite ZnO (JCPDS no: 36-1451). The red-star labelled which can be assigned to Zn peaks were exhibited in all samples indicating that ZnO nanostructures were grown on zinc substrate. It can be observed that one of Zn peak was overlapped with ZnO (101) peak in which both of them were located at ~36 °. Furthermore, no impurities peak were detected and this confirms that all samples were high purity.

Most of ZnO diffraction peaks were increased when reaction temperature was increased to 200 °C showing that the quantity of nanostructures formed are getting pronounced. The highest diffraction peak corresponding to the ZnO (002) crystal plane revealed that all samples showed preferred orientation growth along *c*-axis except for sample heated at 200 °C. The diffractogram for this sample depicts its diffraction peak of (101) was higher if compared to ZnO peak (002), shows that other orientation growth has taken place.

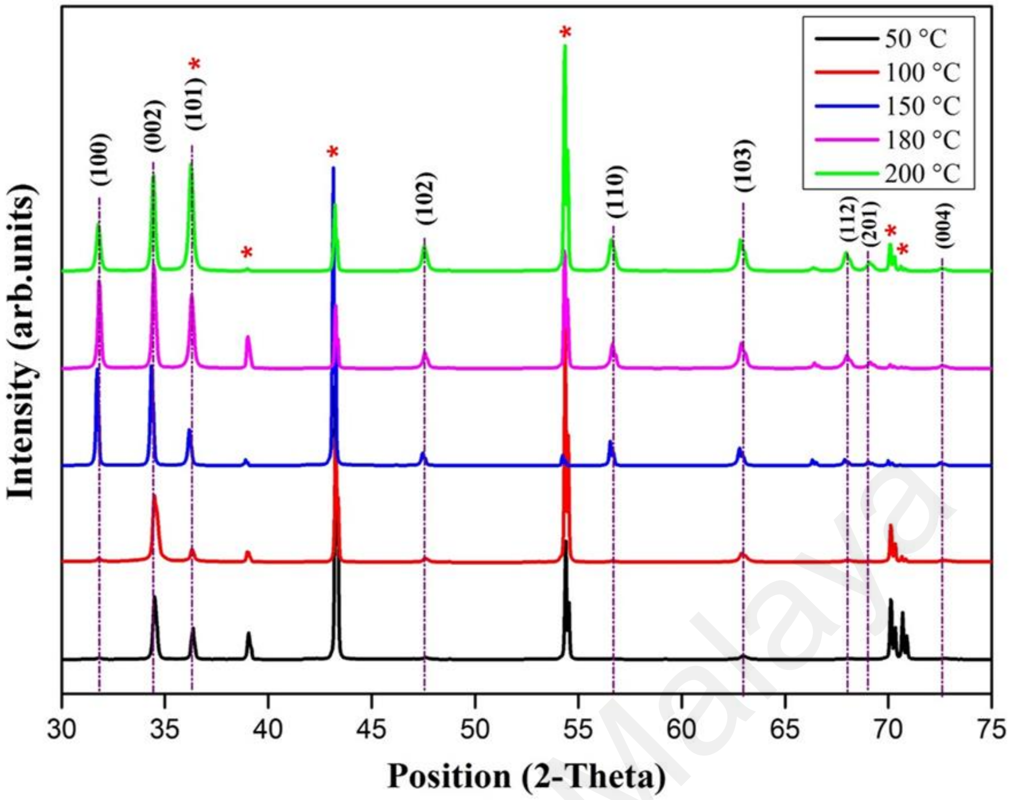

Figure 4.2: XRD pattern of ZnO nanostructures that hydrothermally grown at varied reaction temperature

As shown in FESEM micrographs, when reaction temperature was getting increased the morphology of ZnO nanostructures was transformed to longer horizontal rod-like and larger flower-like ZnO in which these kinds of morphologies were not appropriate to be sensitized with noble metal nanoparticles. In addition, the aim of this study is to obtain rod-like structure with no formation of additional ZnO nanostructures on top of them. The sample heated at 100 °C produced rod-like structure. However, their tips were too smooth and tapered to be decorated with Ag nanoparticles and the rod-like ZnO structure have higher potential to be collapsed.

The rod-like ZnO structures that grown at 50 °C seems to be acceptable to be decorated with Ag nanoparticles due to their larger and round tips. However, optimization has to be continued by changing other parameters as this sample generated flower-like structures on the tips of rod-like ZnO. Therefore, temperature 50 °C was chosen as fixed parameter for the rest of other optimization experiments. This parameter had been chosen in order to comply with initiative in developing an energy efficient yet cost-effective synthesis scheme. In fact, ZnO nanostructures were already formed at 50 °C.

4.3 Morphology Optimization via Synthesis Duration

The optimization was further conducted by varying the synthesis duration in which the duration to synthesize ZnO nanostructures was reduced. Other parameters such as temperature, vol. of DI water and heating rate were fixed at 50 °C, 40 % vol. of DI water and 5 °C.min^{-1}, respectively. The synthesis duration was reduced to 20 H and was compared with the sample that heated at 24 H. Figure 4.3 shows the XRD pattern of ZnO nanostructures that synthesized at 24 H and 20 H.

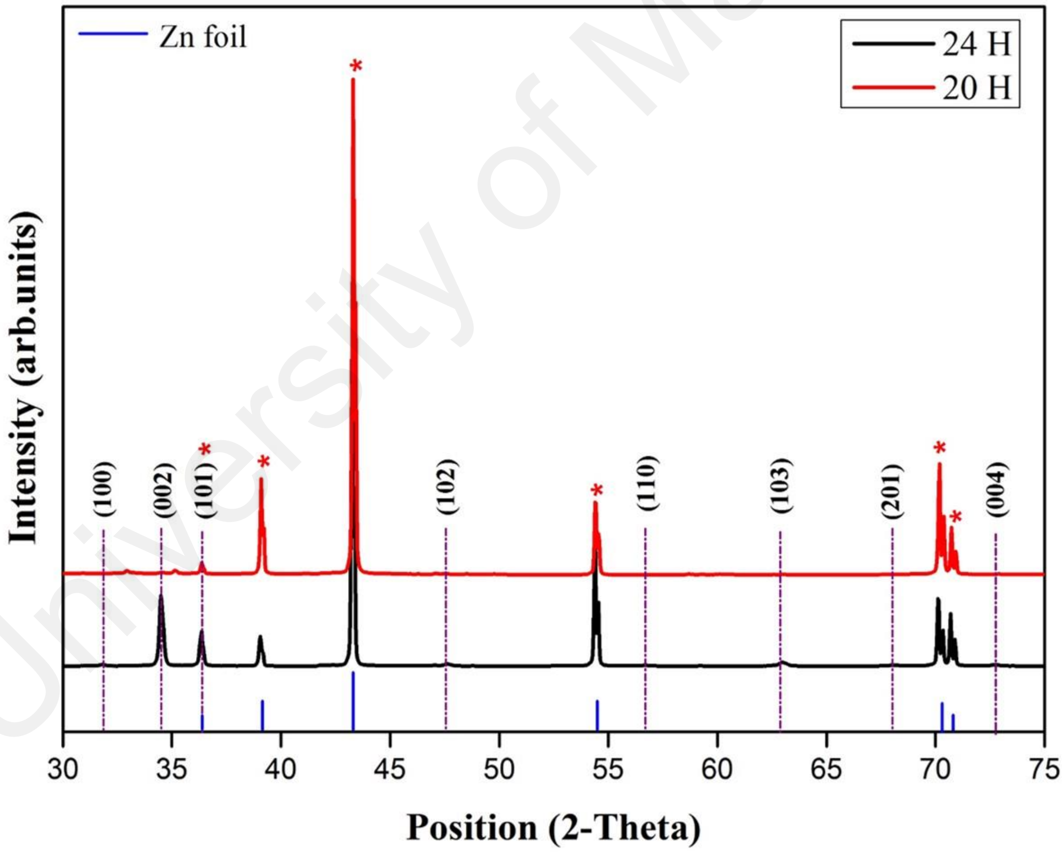

Figure 4.3: XRD pattern of ZnO nanostructures at 24 H and 20 H synthesis duration, respectively

As can be depicted in Figure 4.3, there is no any ZnO diffraction peaks were formed when synthesis duration was reduced to 20 H. The peak located at 36° probably belongs to Zn peak as this peak overlaps with ZnO (101) peak. Since ZnO was not formed at 20 H, thus this sample was not characterized by FESEM and further analysis is through XRD only. From the Figure 4.3, it has been confirmed that synthesis duration was fixed at 24 H throughout the optimization experiments.

In order to obtain desired ZnO structure, morphology optimization by varying other parameters such as vol. of DI water and heating rate will be further conducted and will be discussed in next section.

4.4 Morphology Optimization via Volume of DI Water

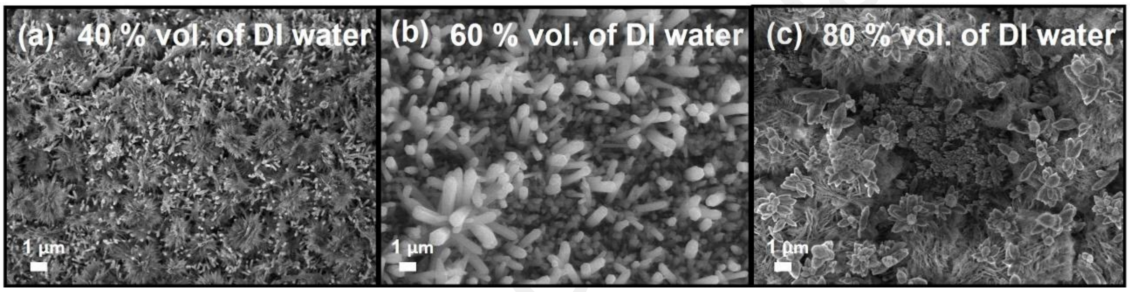

Figure 4.4: FESEM morphologies of ZnO nanostructures at varied vol. of DI water (a) 40 %, (b) 60 % and (c) 80% with heating rate of 5 °C.min^{-1}

As discussed in section 4.2 and 4.3, the reaction temperature and synthesis duration were already fixed at 50 °C and 24 H, respectively. The ZnO morphology optimization was further performed by varying the vol. of DI water parameter from 40 % (20 mL) – 80 % (40 mL) and the heating rate was fixed at 5 °C.min^{-1}.

Herein, DI water acted as precursor to grow ZnO on Zn foil. As depicted in Figure 4.4(a), it is showed that flower-like structures are grown on the tips of rod-like ZnO nanostructures at 40 % vol. of DI water (this sample is same with sample in Figure 4.1(a) because the used parameters were similar and this sample acted as controlled sample in this optimization experiment). As DI water vol. was increased to 60 %, the flower-like structure disappeared and longer ZnO rods were continually grown. However, the length and size of rods were not uniform as displayed in Figure 4.4(b). Finally, irregular shape of flower-like structures were further grown on Zn foil when vol. of DI water was increased to 80 % as viewed in Figure 4.4(c).

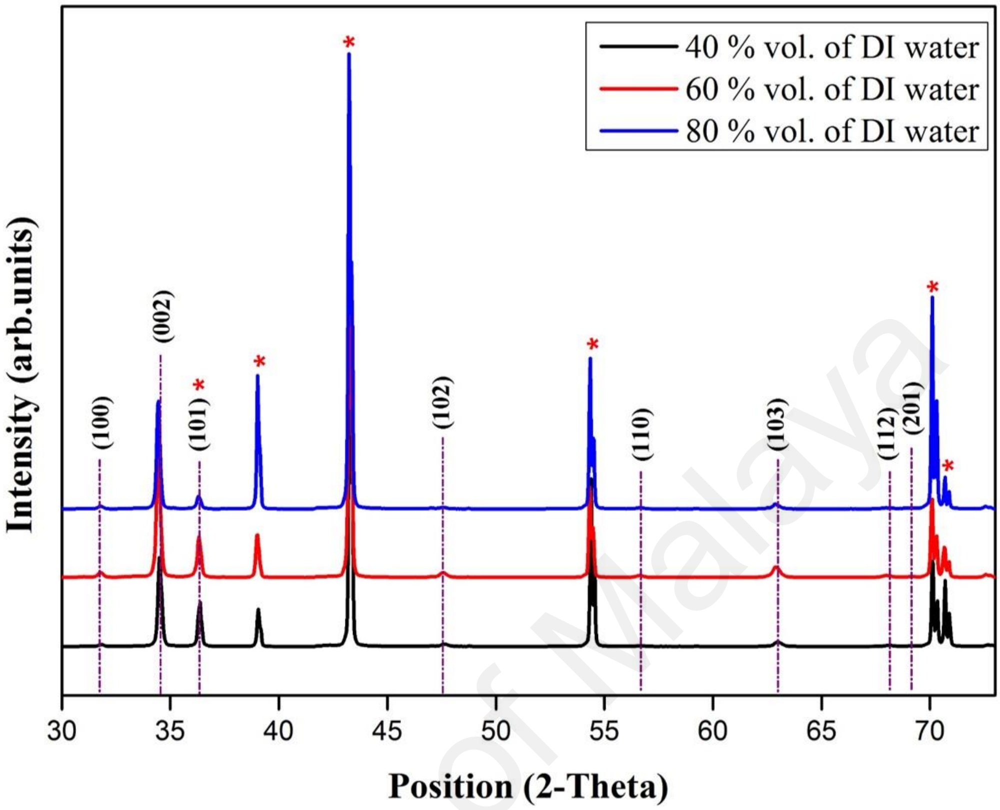

Figure 4.5: XRD pattern of ZnO nanostructures with varied vol. of DI water at 5 °C.min^{-1} heating rate

The phase composition and crystal structure of ZnO nanostructures with varied vol. of DI water are shown in Figure 4.5. All of the samples are exhibited Zn foil peaks and well-indexed to the hexagonal wurtzite phase of ZnO. In addition, there is no impurities peak detected, indicating all of samples are high purity. The highest diffraction peak corresponding to (002) plane showed that all samples have preferred growth orientation along *c*-axis which is this outcomes are similar to the previous result.

The morphology optimization of ZnO through varied heating rate was further continued in order to achieve one of the study objective for obtaining desired pillar-like structure of ZnO. The results will be discussed in the next Section 4.5.

4.5 Morphology Optimization via Heating Rate

By fixing the synthesis temperature and duration at 50 °C and 24 H, the ZnO morphology optimization was conducted in vol. of DI water at 40 % (20 mL) – 80 % (40 mL) whereby the heating rate was varied to 1°C.min^{-1}. However, in this section the optimization experiment was executed at 50 % (25 mL) and 70 % (35 mL) vol. of DI water as well to precisely observe the morphological transformation of ZnO nanostructures and at the same time to obtain the desired pillar-like structure.

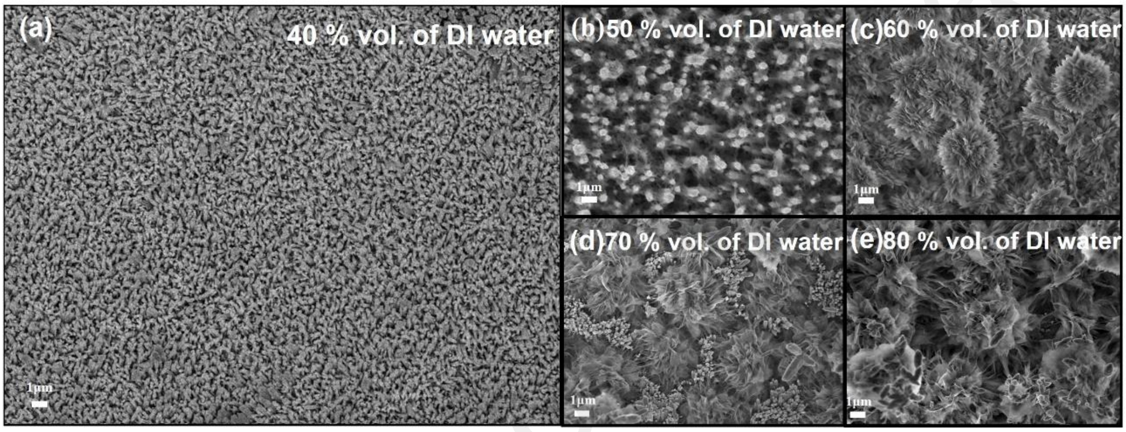

Figure 4.6: FESEM morphologies of ZnO nanostructures at vol. of DI water (a) 40 %, (b) 50 %, (c) 60 %, (d) 70 % and (e) 80% with heating rate 1 °C.min^{-1}

FESEM micrographs of ZnO nanostructures that heated at different vol. of DI water (with heating rate 1°C.min^{-1}) are depicted in Figure 4.6. As observed in Figure 4.6(a), rod-like structure are formed at 40 % vol. of DI water. When vol. of DI water is increased to 60 %, thin layer-like interconnected mesh (Figure 4.6(b)) are originated from the tips of ZnO nanorods, where these meshes are connected to the tips of the adjacent nanorods to form a randomly linked-hierarchical nanostructures. Interestingly, as vol. of DI water are added up to 60 %, these meshes are self-assembled into flower-like structure (Figure 4.6(c)). With further increasing vol. of DI water to 70 %, the density of nanoflowers coverage further increased and they are highly-compacted with each other. Moreover, for the sample produced with 80 % vol. of DI water, it is found that the individual pedal of the nanoflowers further expand and create an interconnection topology with its neighbouring nanoflowers as shown in Figure 4.6(e).

Figure 4.7 shows the XRD pattern of ZnO nanostructures that were prepared with heating rate of 1 °C.min^{-1} for vol. of DI water from 40 % - 80 %. It is observed that all of the as-prepared samples can be well-assigned to the hexagonal wurtzite phase of ZnO whereby the present of Zn foil peaks indicates that Zn foil functions as substrate to direct grow the ZnO nanostructures. The present of impurities peak cannot be detected confirming that as-prepared samples are well-crystalline and high purity. Diffraction peak of (002) is the strongest peak indicates that as-synthesized samples are preferred to grow along the *c*-axis orientation.

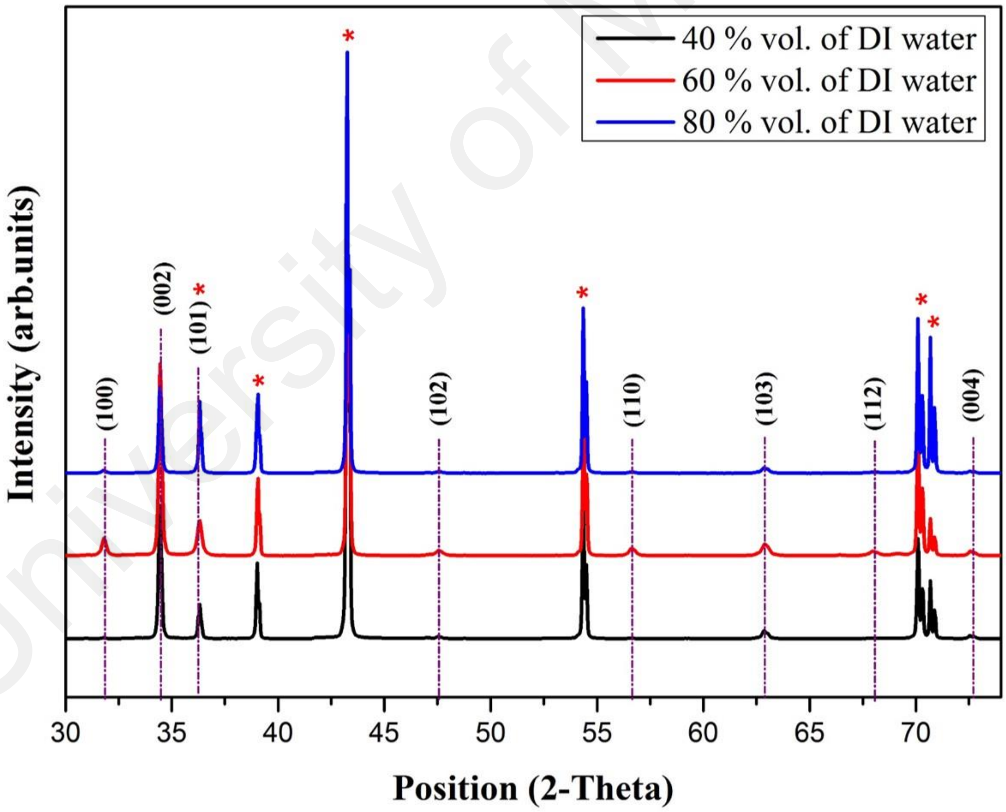

Figure 4.7: XRD pattern of ZnO nanostructures with different vol. of DI water that heated at 1 °C.min^{-1}

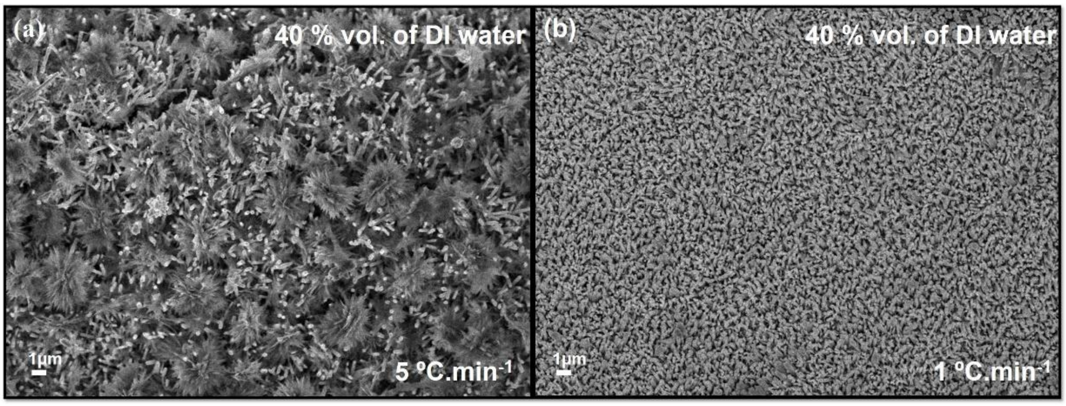

Figure 4.8: FESEM micrographs of ZnO nanostructures that were prepared with heating rate of (a) 5 °C.min^{-1} and (b) 1 °C.min^{-1} in 40 % vol. of DI water

From the morphological view of Figure 4.8, it is demonstrated that when heating rate was reduced to 1 °C.min^{-1}, rod-like structure of ZnO were formed. It is hypothesized that at higher heating rate, the nucleation process occurs faster which finally render the formation of flower-like structure on the tips of ZnO rods. Hence, heating rate was reduced to 1 °C.min^{-1} to enable the nucleation process to occur slower. As a result, the formation of desired rod-like structure, or so-called ZnO nanopillars structure can be realized (Figure 4.8(b)). With respect to all of the morphology optimization results, the optimized parameters in order to grow the desired ZnO nanopillars structure are compiled in Table 4.1 below:

Table 4.1: Optimized parameter for ZnO nanopillars growth

Parameters	Temperature (°C)	Duration (H)	Volume of DI water (%)	Heating Rate (°C.min^{-1})
	50	24	40	5
	100	20	60	1
	150	-	80	-
	180	-	-	-
	200	-	-	-
Optimized Parameter	50	24	40	1

After obtained the desired ZnO nanopillars via the optimized parameter, the as-synthesized ZnO nanopillars will be further integrated with noble metal, Ag and the results will be discussed in Chapter 5. In addition to these results, effect towards the ZnO morphology transformation when Zn salts are used as precursor was studied as well and the outcomes will be explained in the next section.

4.6 Effect of Additional Zn Salts towards the ZnO Morphology

The effect towards the ZnO morphology was further investigated when Zn salts were used as an additional precursor. The procedure can be referred in Chapter 3 (Section 3.3.2). Herein, synthesis temperature, duration and heating rate were fixed at 50 °C, 24 H, 1 $°C.min^{-1}$. The vol. of Zn nitrate aqueous solution was varied from 40 % (20 mL) – 80 % (40 mL) with fixed concentration of 12.5 mM. Figure 4.9 shows the morphology of ZnO nanostructures grown in additional Zn source via one step hydrothermal method.

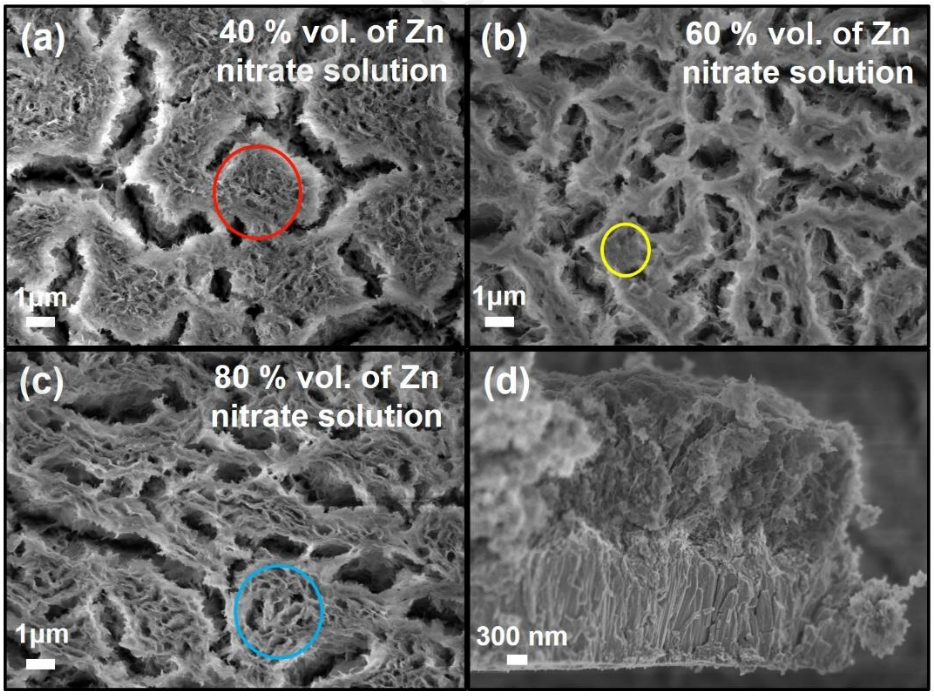

Figure 4.9: FESEM micrographs of ZnO nanopillars/nanowalls in vol. of Zn nitrate aqueous solution of (a) 40 %, (b) 60 %, (c) 80 % with concentration of 12.5 mM and (d) cross section image of sample (a)

As displayed in Figure 4.9(a), it is clearly seen that sheet-like structure of ZnO were grown when Zn foil was heated in 40 % vol. of 12.5 mM Zn nitrate aqueous solution. ZnO sheet-like structure developed an area that analogous to an island-like structure which is composed of compact yet small pores as marked with red-circle in Figure 4.9(a). As vol. of Zn nitrate aqueous solution was increased to 60 %, the area of island-like structure is reduced and the pores within it are hardly seen as shown with yellow-circle in Figure 4.9(b). Interestingly, at 80 % vol. of Zn nitrate aqueous solution, the area of island-like structure is disappeared in which the pores are getting widely opened (blue-circle) as depicted in Figure 4.9(c).

After a careful examination on the cross-section image of sample that heated in 40 % vol. of Zn nitrate aqueous solution, the sheet-like of ZnO structures were actually agglomerated to each other and render formation of wall-like structure of ZnO. As depicted in Figure 4.9(d), nanopillars are firstly grown on Zn foil with the formation of nanowalls on top of nanopillars. Upon the addition of Zn nitrate, the length of pillars is estimated to be ~2.10 – 2.14 μm, while the nanowalls possess thickness of ~2.6 μm. The presence of Zn nitrate render an excessive concentration of Zn ions that promote dual-layer morphology, which is composed of nanopillars/nanowalls. This process is deduced to secondary nucleation process that takes place on the performed nanopillars.

The phase composition and crystal structure of ZnO nanopillars/nanowalls with different vol. of Zn nitrate aqueous solution at fixed concentration of 12.5 mM are revealed by XRD as depicted in Figure 4.10. All of the as-prepared samples are well-indexed to the hexagonal wurtzite ZnO. As mentioned earlier, the red-star labelled can be assigned to the Zn peaks which proof that ZnO nanopillars/nanowalls were grown on the Zn substrate. There is no other impurities peak, confirmed that all as-synthesized samples are well-crystalline and indeed consist of high purity. In addition, the highest diffraction peak corresponding to the ZnO (002) crystal plane revealed that all as-obtained samples showed preferred orientation growth along *c*-axis.

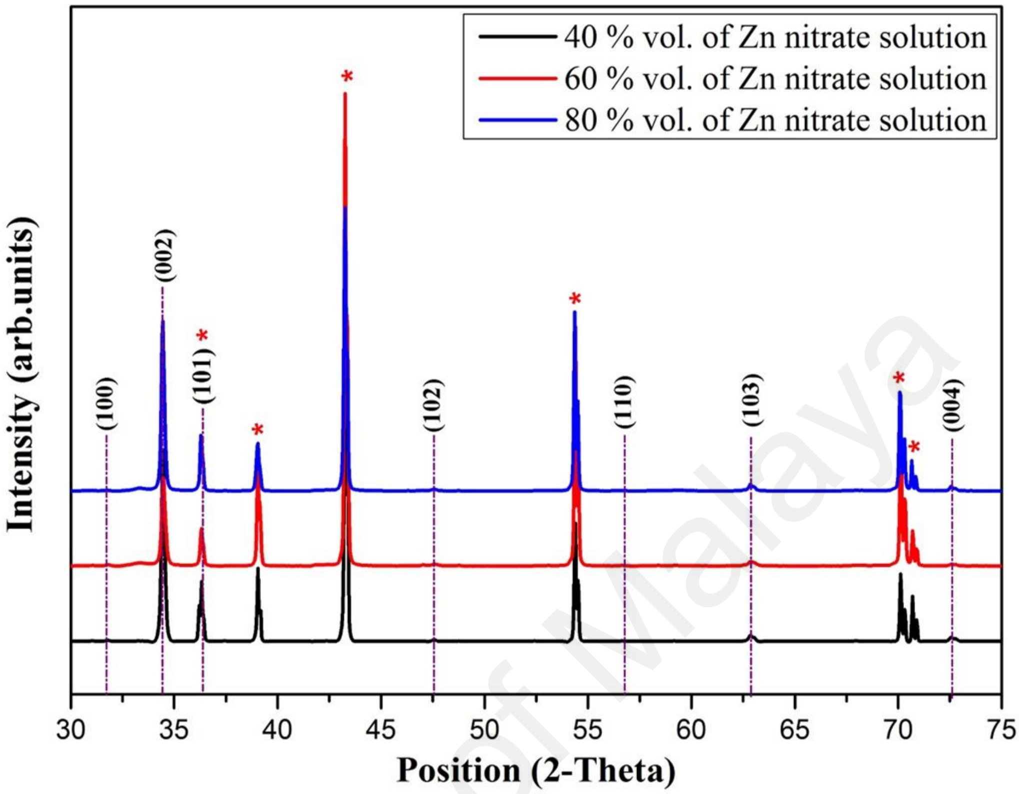

Figure 4.10: XRD pattern of ZnO nanopillars/nanowalls with different vol. of Zn nitrate aqueous solution at fixed concentration of 12.5 mM

4.7 Effect of Different Zn Salts Concentration towards the ZnO Morphology

The study of an effect towards ZnO morphology via the different Zn salts concentration was further performed. Herein, concentration of Zn nitrate aqueous solution was varied from 3.125 – 18.75 mM whereby the as-prepared ZnO nanopillars/nanowalls _12.5 mM plays the role as control sample. Synthesis temperature, duration, heating rate and vol. of Zn nitrate aqueous solution were fixed at 50 °C, 24 H, 1 $°C.min^{-1}$ and 40 % vol.

FESEM micrographs of ZnO nanopillars/nanowalls in 40 % vol. of Zn nitrate aqueous solution with different concentration are depicted in Figure 4.11. As revealed in Figure 4.11(a), the red-circle shows that the walls-like structures of ZnO have wide and bigger pores when Zn foil was heated in 3.125 mM of Zn nitrate aqueous solution. Additionally, when the concentration was increased to 6.25 mM, an island-like structure is reconstructed and bridged with adjacent island-like structures to form interconnected network analogous to sheet-like nanostructures (orange-circle) as depicted in Figure 4.11(b). Interestingly, this sheet-like nanostructures are merged together to form larger island area, which appeared to be compact and possess small pores (yellow-circle) when concentration was increased to 12.5 mM as shown in Figure 4.11(c). Finally, at concentration of 18.75 mM an island-like structures are getting larger while their pores are found to be more compact and getting smaller (blue-circle) if compared to that of sample with 12.5 mM concentration. It is postulated that ZnO nanopillars/nanowalls have wide and open pores at low concentration, yet the pores will get compact and small when the concentration was increased.

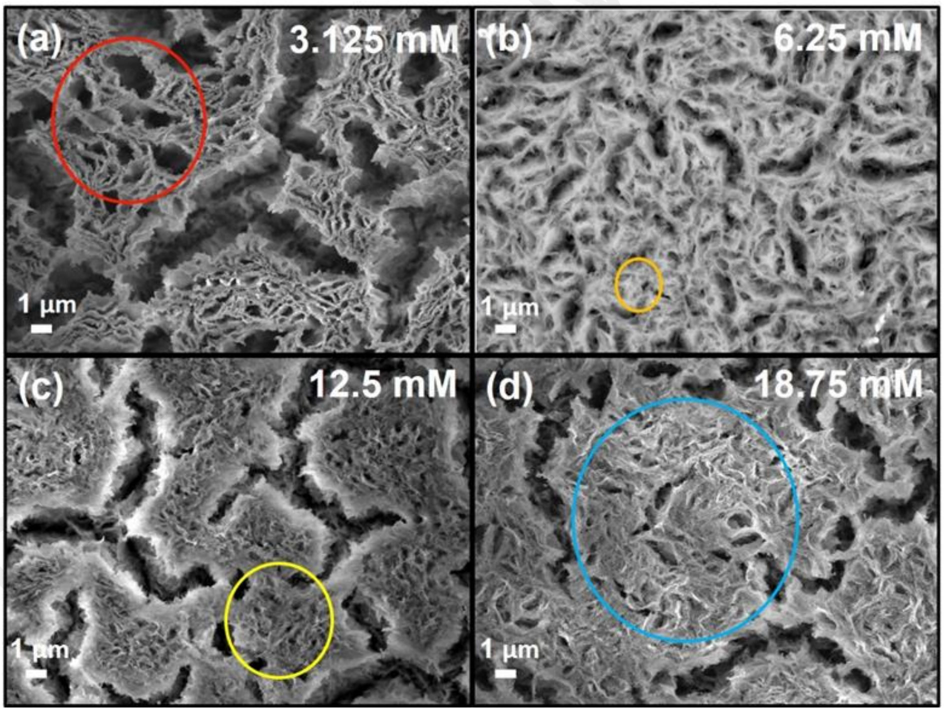

Figure 4.11: FESEM micrographs of ZnO nanopillars/nanowalls with different concentration of Zn nitrate at (a) 3.125 mM, (b) 6.25 mM, (c) 12.5 mM and (d) 18.75 mM in 40 % vol. of Zn nitrate aqueous solution

Figure 4.12 demonstrated the XRD pattern of ZnO nanopillars/nanowalls which is grown in different concentration of Zn nitrate aqueous solution. All of the as-prepared samples are well-crystalline and can be well-assigned to hexagonal wurtzite phase of

ZnO. Additional Zn peaks appear in all samples indicate that they were grown on the Zn substrate. The crystal planes are increased when concentration of Zn nitrate aqueous solution was increased, in which ZnO diffraction peak that correspond to (002) crystal plane is the highest peak showing that all of the as-prepared samples have the tendency to grow along the c-axis orientation. Furthermore, no other impurities peaks are observed, confirmed that the samples are composed of high purity.

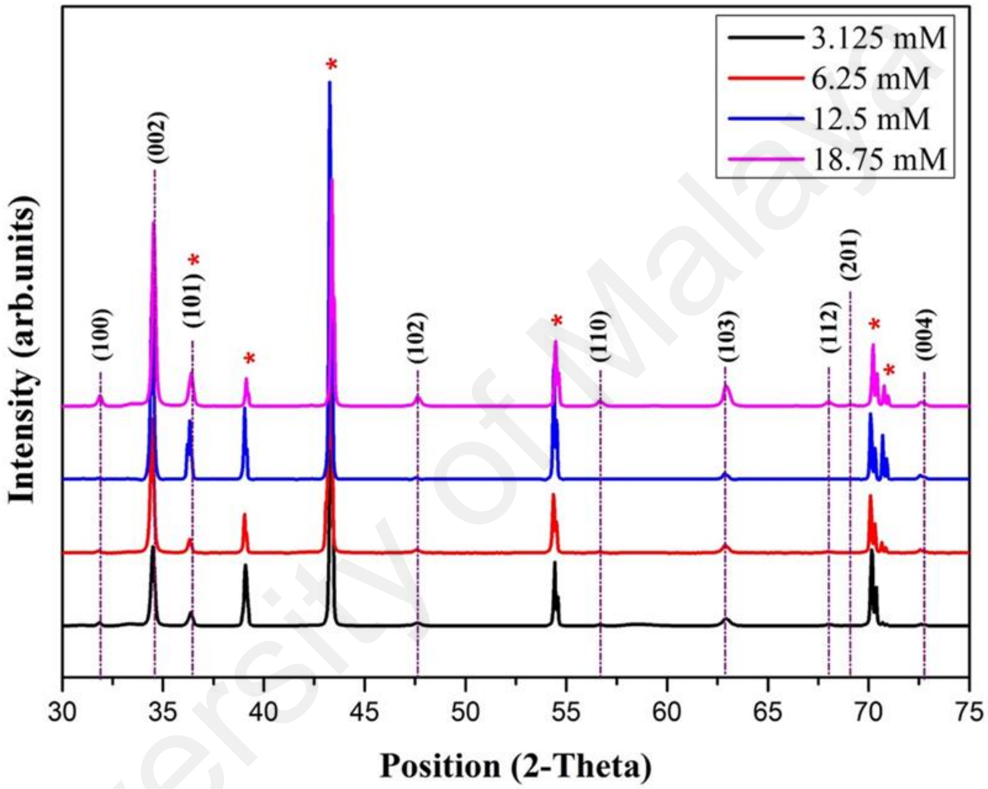

Figure 4.12: XRD pattern of ZnO nanopillars/nanowalls at different concentration of Zn nitrate aqueous solution

However, at current stage, ZnO nanopillars/nanowalls samples are not proceeded to sensitize with noble metal as these samples possess dual-layer morphology that will impede the pathway of incident solar light especially the bottom layer of ZnO nanopillars during PEC process. Hence, we prefer to sensitize noble metal with ZnO nanopillars in order to fully utilize this structure to enhance the photocurrent generation via PEC water splitting process. The analysis of ZnO nanopillars/nanowalls are only a predetermined factor for following steps, where the ideal parameter from this chapter will be used for

Ag nanoparticles integration process to develop into metal/semiconductors (Ag/ZnO) photoelectrode. Nevertheless, this preliminary results have enable the understanding of the morphology behaviour of ZnO that grown on Zn foil with an additional Zn source via an optimized parameter. This study might be further investigated and will be beneficial for future works.

4.8 Summary

All of the morphology optimization to obtain the desired pillar-like structures of ZnO via an optimized parameter have been discussed. In addition, the study of an effect towards ZnO morphology with an additional and different concentration of Zn nitrate aqueous solution have been explained. The ZnO nanopillars will be hydrothermally sensitized with noble metal through two optimized parameter which all the characterizations will be discussed in Chapter 5.

CHAPTER 5: ARGENTUM NANOPARTICLES SENSITIZED ZINC OXIDE NANOPILLARS PHOTOELECTRODE

5.1 Introduction

In this chapter, the sensitization of noble metal (Ag) on the surface of ZnO nanopillars via two optimized parameters will be discussed in detailed. Meanwhile, the structural- and optical-properties of Ag sensitized ZnO photoelectrode will be further explained in depth and the growth mechanism of the photoelectrodes will be proposed.

5.2 Sensitization of Ag nanoparticles on ZnO nanopillars via Ag^+ Ions Reduction Period

Ag nanoparticles were incorporated on the surface of ZnO nanopillars via the varied Ag^+ ions reduction period through two step hydrothermal method at 50 °C in 40 % vol. of $AgNO_3$ with concentration of 1 mM. The full procedure can be referred in Chapter 3.3.3.1. The characterization of these samples and the growth mechanism are discussed in the following section.

5.2.1 FESEM Analysis

The morphological evolution of pure ZnO nanopillars and Ag nanoparticles integrated ZnO nanopillars which were synthesized with different Ag^+ ions reduction period via hydrothermal method can be depicted in Figure 5.1. By utilizing DI water as the growth medium and without the presence of any surfactant, ZnO nanopillars were formed on the Zn foil as displayed in Figure 5.1(a). The optimization parameter to obtain this so-called desired pillar-like structure can be referred in Chapter 4. From the topological view of Figure 5.1(a), it is clearly seen that ZnO nanopillars are densely covered on the Zn foil. The nanopillars are found to possess an average length of ~ 600 – 700 nm with a blunt-terminated tip as observed in inset of Figure 5.1(a). Reaction parameters are crucial for the formation of intriguing nanoarchitectures. Thus, in order to investigate the influence of reduction period of Ag^+ ions towards the morphology of ZnO nanopillars, time-dependent study was systematically conducted by varying the reduction period of Ag^+ ions from 30 – 360 min. The morphology evolution of Ag nanoparticles decorated ZnO nanopillars are revealed in Fig. 1(b-f) with their respective cross section images are shown in the inset images.

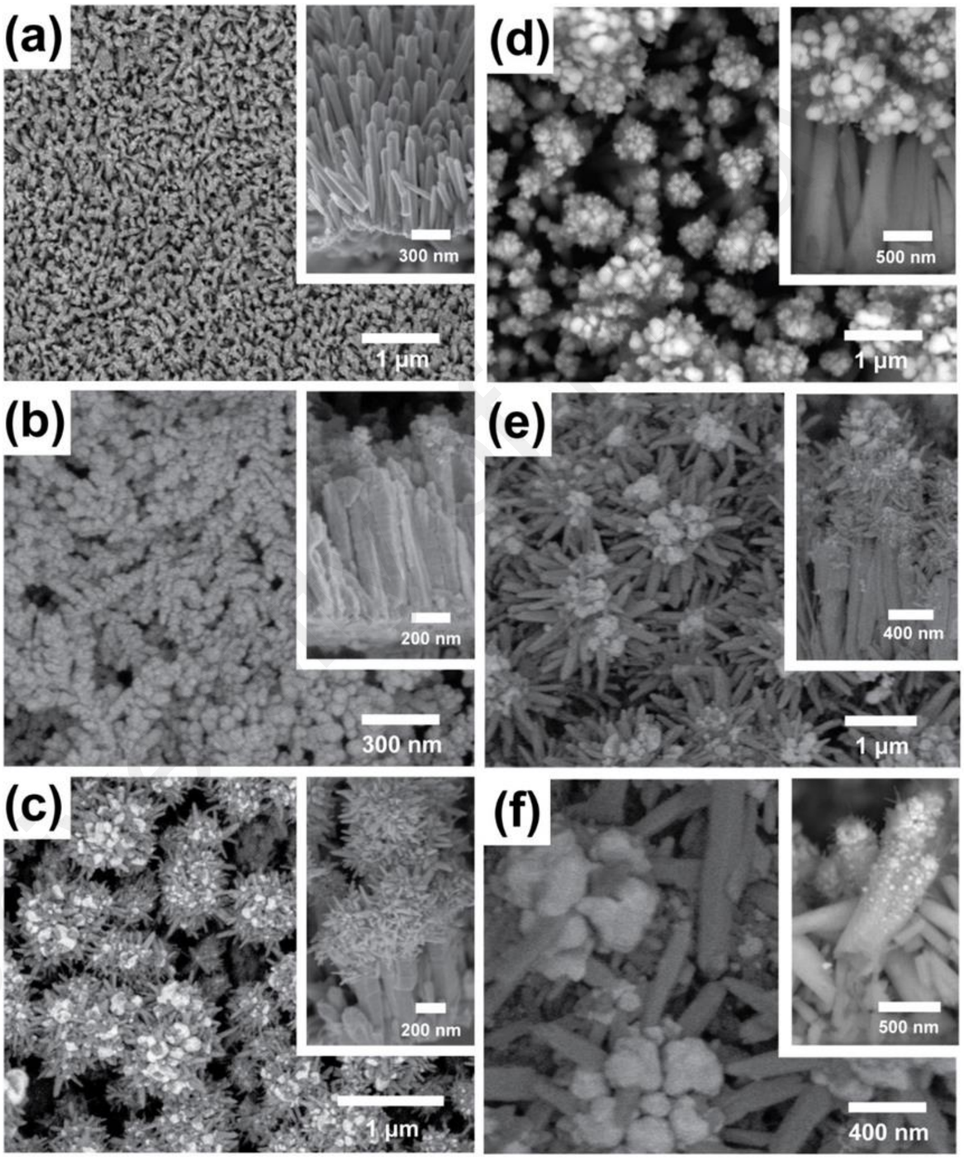

Figure 5.1: FESEM micrographs of (a) ZnO nanopillars, (b) Ag/ZnO_30 min, (c) Ag/ZnO_60 min, (d) Ag/ZnO_120 min, (e) Ag/ZnO_240 min and (f) Ag/ZnO_360 min. Inset is cross-section view of respective samples

High angle backscattered electron (HABSE) mode was employed during the FESEM scanning of Ag nanoparticles integrated ZnO nanopillars in order to observe the compositional contrast of materials, in which darker sites represent ZnO nanopillars while that of brighter spots represent Ag nanoparticles. Figure 5.1(b) depicts poor contrast on the image, thus it shows that Ag nanoparticles are densely deposited on the tips of ZnO nanopillars upon 30 min Ag^+ ions reduction period. As the reaction time increased, the length of ZnO nanopillars is increased to ~1.00 – 1.10 μm as measured from the cross section view of sample Ag/ZnO_30 min (inset of Figure 5.1(b)). When the reduction time was prolonged to 60 min, branched of short, tiny and blunt tips of pillar shape were sprouted out along the edges on the upper half of primary ZnO nanopillars according to high-magnification FESEM cross section image (inset Figure 5.1(c)). This indicates that primary ZnO nanopillars had underwent secondary nucleation with Ag nanoparticles were randomly deposited on the interstices among the premature secondary nanopillar. From the morphological point of view of Figure 5.1(c), these Ag nanoparticles decorated ZnO nanopillars heterostructures can be described to be analogous to the “broccoli-like” structure.

As revealed in Figure 5.1(d), the branched of tiny secondary ZnO nanopillars are hardly observable when reduction period was further increased to 120 min and the density of coverage for Ag nanoparticles is significantly dominates the surface of preformed nanopillars, whereby there is an obvious increment of the diameter for Ag nanoparticles concurrently. Based on this observation, it is postulated that pre-deposited Ag nanoparticles had experienced coarsening effect to form larger grain under the environment that were contained with abundance of $AgNO_3$ aqueous solution. Further prolonging the hydrothermal duration up to 240 min had caused the length and size of secondary ZnO nanopillars progressively lengthened approximately two times in contrast to the secondary ZnO nanopillars at 60 min reduction period. These phenomenon might be due to the so-called Ostwald ripening process and the mechanism will be discussed later. There are no any significant changes on the length of secondary ZnO nanopillars when reduction period was prolonged to 360 min as shown in Figure 5.1(f). Nevertheless, there is an increment on the diameter of Ag nanoparticles for this sample with interparticles agglomeration, particularly in between Ag nanoparticles. The size of Ag nanoparticles are hardly to be measured precisely as they were aggregated to each other, but qualitatively the size of Ag nanoparticles were getting larger as the reduction time was extended. Meanwhile, the lengths of ZnO nanopillars were increased ~0.35 – 0.40 μm at 360 min reduction period if compared to that of the sample Ag/ZnO heterostructures which heated at 30 min.

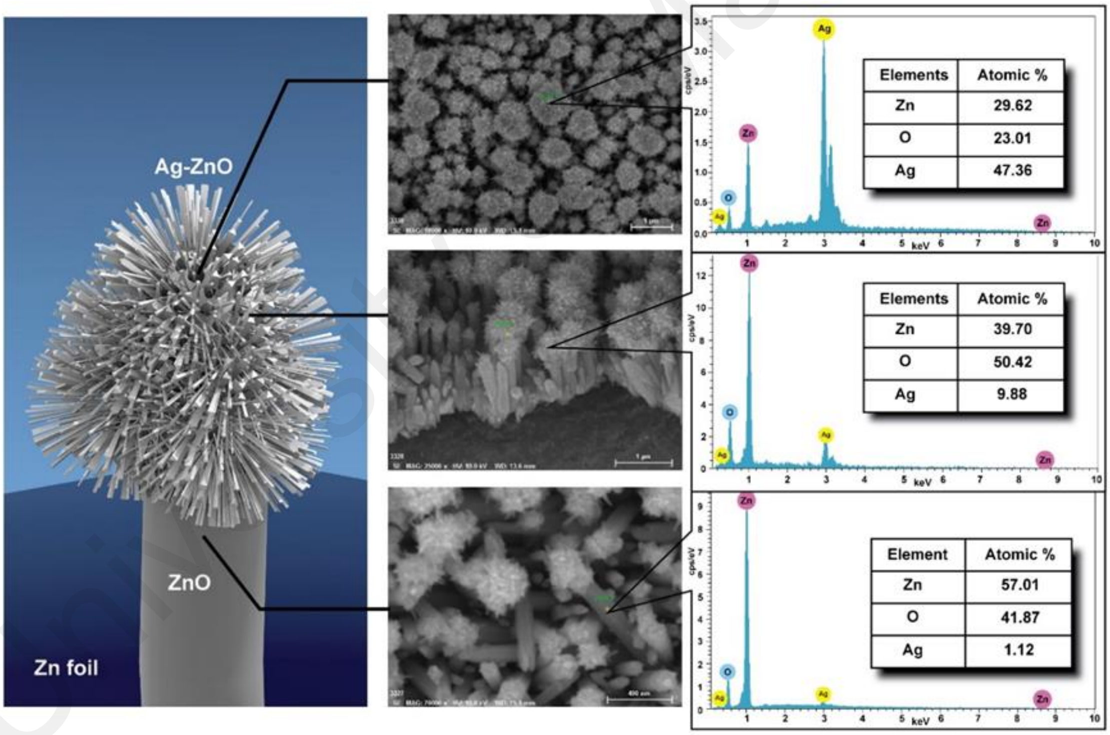

Elements	Atomic %
Zn	29.62
O	23.01
Ag	47.36

Elements	Atomic %
Zn	39.70
O	50.42
Ag	9.88

Element	Atomic %
Zn	57.01
O	41.87
Ag	1.12

Figure 5.2: EDX-FESEM analysis of Ag/ZnO_60 min at (a) top of branched secondary pillars, (b) side of branched secondary pillars and (c) primary pillars

As a complement, energy-dispersive X-ray (EDX) analysis has been carried out to study the elemental composition of Ag/ZnO_60 min sample as shown in Figure 5.2. According to the top of branched secondary pillars scan (Figure 5.2(a)), highest atomic concentration are detected and this implies abundance of Ag element is occupying this area as a result of highly-agglomerated Ag nanoparticles. The side scan of branched secondary pillars (Figure 5.2(b)) and primary pillar scan (Figure 5.2(c)) indicate that Zn and O elements represent the highest atomic concentration and these further confirm that branched secondary pillars and primary pillars are composed of ZnO. Furthermore, the relative atomic ratios of Zn:O are determined to be 1:1, which is consistent to the stoichiometry ratio of ZnO.

5.2.2 HRTEM Analysis

Detail analysis was further carried out by characterizing Ag/ZnO_60 min sample via HRTEM technique. The justification to select Ag/ZnO_60 min as target of HRTEM analysis due to the reason that 60 min of Ag^+ ions reduction period was the starting point where branching of secondary ZnO nanopillars begin to take place. The high-magnification of bright field transmission electron microscope image of Ag nanoparticles decorated ZnO nanopillars at 60 min reduction period is depicted in Figure 5.3(a) together with corresponding inset image that shows the overview under low-magnification mode. With referring to the image, Ag nanoparticles are randomly distributed over the surface and tips of primary as well as secondary ZnO nanopillars. High-angle annular dark filed (HAADF) TEM image (Figure 5.3(b)) that corresponding to Figure 5.3(a) has been collected to distinguish the existence of Ag nanoparticles on the ZnO nanopillars that serve as matrix.

The dark filed image depicts a clear contrast between the Ag nanoparticles and the primary as well as secondary nanopillars, where there is a difference in terms of contrast for both materials. This is due to the differences in the electron scattering effects that results of the variation in the mean atomic number (Z). Therefore, the earlier hypothesis about the existence of Ag nanoparticles that coupled onto the surface of ZnO nanopillars are proven hereon. With respect to this, Ag nanoparticles possess higher Z value if compared to ZnO pillars and thus had rendered brighter contours while the darker contours appear to be ZnO as it has lower *Z* value (Haw et al., 2016).

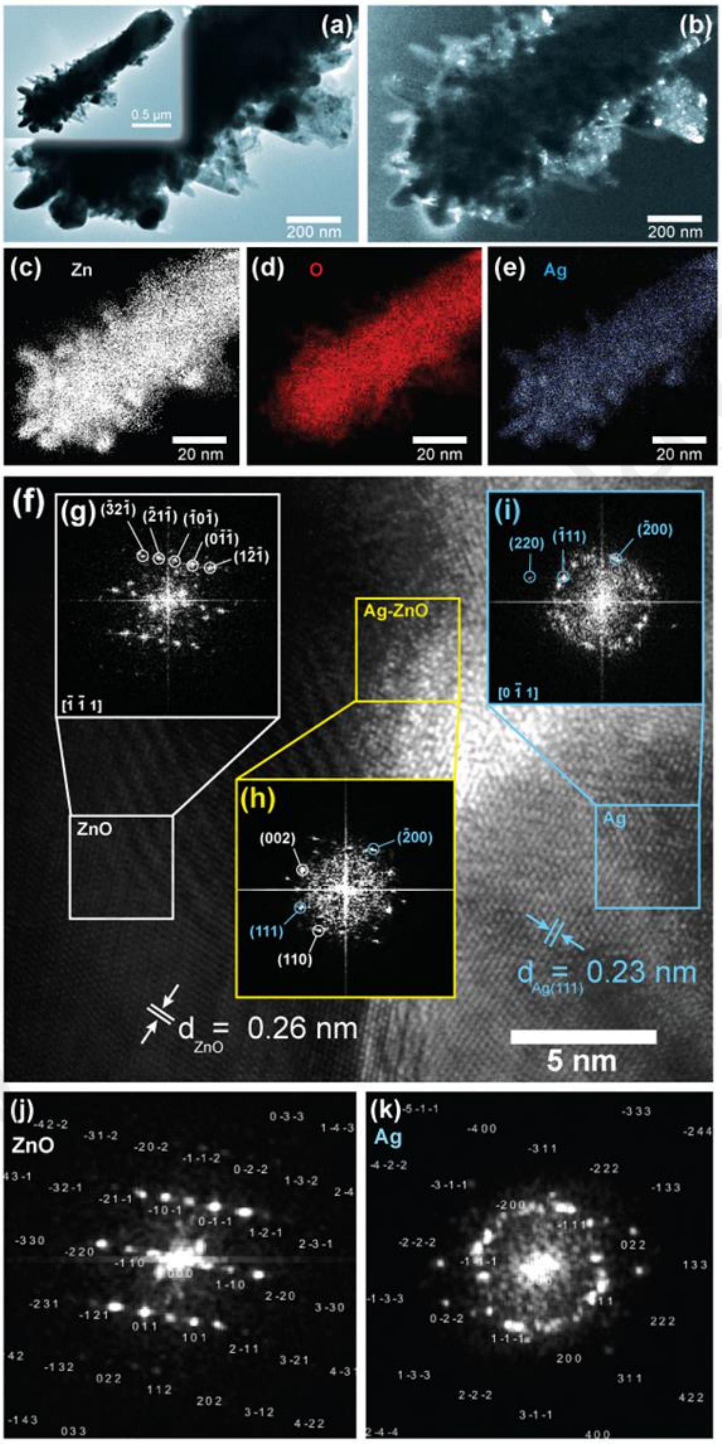

Figure 5.3: (a) Bright field TEM image of Ag/ZnO_60 min, inset shows the overall picture of the (a), (b) dark field TEM image of Ag/ZnO_60 min, (c-e) elemental mapping of Zn, O and Ag, respectively, (f) high resolution TEM image of selected regions indicate the interfacial distance of ZnO, interface of Ag-ZnO and Ag, respectively, (g-i) FFT analysis pattern taken from each individual region in (f) and (j, k) Respectively show the simulated for ZnO and Ag

In order to further affirm the distribution of Ag nanoparticles on ZnO nanopillars, elemental mapping were conducted onto this sample during TEM analysis and the results is depicted in Figure 5.3(c-e). As displayed in Figure 5.3(c) and 5.3(d), Zn and O are well-distributed along the primary and secondary pillars, while intense blue colour in Figure 5.3(e) indicates the presence of Ag nanoparticles that randomly distributed on the branched of secondary pillars and on the upper half of primary pillars edge. High-resolution TEM image is provided in Figure 5.3(f) for a better comprehension of the interfacial bonding between the face-centred cubic phase and the hexagonal wurtzite phase. Three distinctive regions have been selected to view the lattice fringes as shown in Figure 5.3(g-i). With respect to white square area, the interplanar spacing is estimated to be 0.26 nm which corresponds to the (002) lattice fringes of hexagonal wurtzite structure of ZnO. FFT analysis at this spot can be assigned to zone axis of $[\bar{1}\bar{1}1]$ as displayed in Figure 5.3(g). At the same time, yellow square area shows the interface in between ZnO nanopillars and Ag nanoparticles and its corresponding FFT analysis pattern (Figure 5.3(h)) reveals the presence of combination of diffraction for both of the ZnO and Ag crystal structure.

By referring to the diffraction spots, the white colour circled spots can be ascribed to the diffraction signal that belongs to ZnO hexagonal wurtzite structure for (002) plane and (110) plane. Moreover, the blue colour circled spots represent the diffraction signal of Ag face-centred cubic phase for the crystal planes of (111) and $(\bar{2}00)$. Hence, all these cruel have further confirmed that Ag nanoparticles are indeed attached onto the surface of ZnO nanopillars. Further analysis in bluish square area clearly indicates the structure of Ag with an interplanar distance of 0.23 nm that corresponds to (111) lattice fringes, whereby this area belongs to $[0\bar{1}1]$ zone axis as depicted in Figure 5.3(i). In addition, both of simulated pattern for ZnO and Ag are respectively depicted in Figure 5.3(j) and 5.3(k). With respect to both of the TEM and FESEM analysis, it is proven that the current approach has successful in integrating Ag nanoparticles onto the surface of ZnO nanopillars. Interestingly, this method also succeed in producing advanced nanoarchitectural analogous to “broccoli-like” morphology.

5.2.3 XRD Analysis

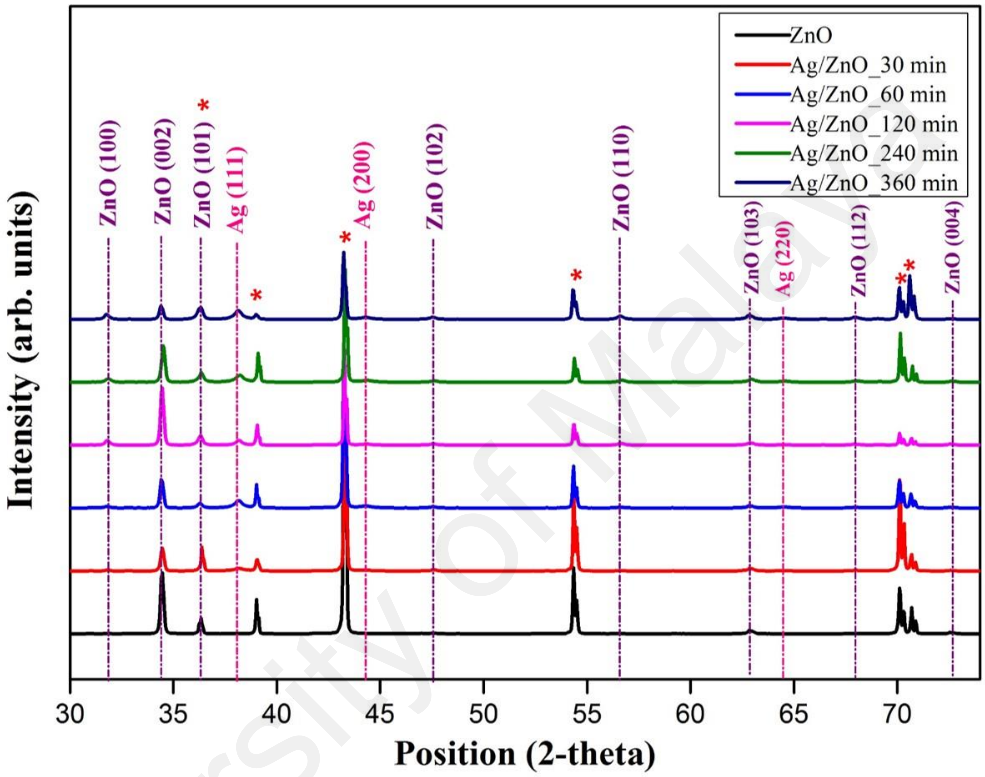

Figure 5.4: XRD pattern of Ag sensitized ZnO photoelectrode at different reduction period of Ag^+ ions by using two steps hydrothermal method

The phase composition and bulk crystal structure of ZnO nanopillars and Ag/ZnO heterostructures that synthesized with varied reduction period of Ag^+ ions are revealed by XRD analysis as displayed in Figure 5.4. All of the samples are well-crystallized and the diffraction peaks could be perfectly indexed to both of the hexagonal wurtzite ZnO (JCPDS no: 36-1451) and face-centred cubic Ag (JCPDS no: 04-0783). The peaks located at 38.1°, 44.2° and 64.4° are belong to Ag with crystal planes of (111), (200) and (220), respectively. Furthermore, peak of Zn foil which is labelled with star also present in all of the samples. Such distinguishable crystal spectrum with multiple peaks that contributed by different constituent compounds imply that all the as-integrated samples are indeed heterostructures without alloying as complement to the observation by FESEM and HRTEM. Also, there is no any impurity peaks detected, which further confirmed that the as-obtained heterostructures are pure.

5.2.4 Raman Analysis

The hexagonal wurtzite ZnO is belonged to the C6v4 space group with Raman active modes of $1A_1 + 1E_1 + 2E_2$. A_1 and E_1 modes are polar which split into traverse optical and longitudinal optical phonons. While, the E_2 mode consists of two modes (low- and high- frequency phonons) (Khan, 2010). Figure 5.5(a) depicts the Raman spectra of ZnO nanopillars and Ag/ZnO heterostructures with different reduction period of Ag^+ ions in the range of 100 – 1200 cm^{-1}.

In order to clearly distinguish the Raman spectrum of pure ZnO nanopillars, magnified spectra has been plotted in Figure 5.5(b). According to the Raman spectra, peak located at 100 cm^{-1} and 438 cm^{-1} can be assigned to E_2 (low) and E_2 (high) peaks of hexagonal wurtzite ZnO, respectively. This indicates the highly crystalline nature of the sample. While, peak 330 cm^{-1} can be attributed to the $3E_{2H-2L}$ multi-phonon vibration in which this peak is related to multi-phonon process, or it is also described to second order Raman spectrum arising from the zone boundary phonon (Deng et al., 2012).

In addition, peak located in the range of 550 – 600 cm^{-1} and 1050 – 1100 cm^{-1} can be attributed to polar mode A_1 symmetry with 1LO and 2LO, respectively (Yin et al., 2012; Chia et al., 2015). After the integration of Ag nanoparticles, the characteristics peaks that belong to pure ZnO nanopillars remain exist except there is a broad band peak located ~225 cm^{-1} is present for all of Ag/ZnO heterostructures samples. This broad band peak can be assigned to the Ag-O_2 of the molecular oxygen species that chemisorbed on the defects of metallic Ag (Millar et al., 1995). This is further proved by Deng et al., in which their Ag nanoparticles decorated ZnO mircorods also have similar characteristic peak (Deng et al., 2012).

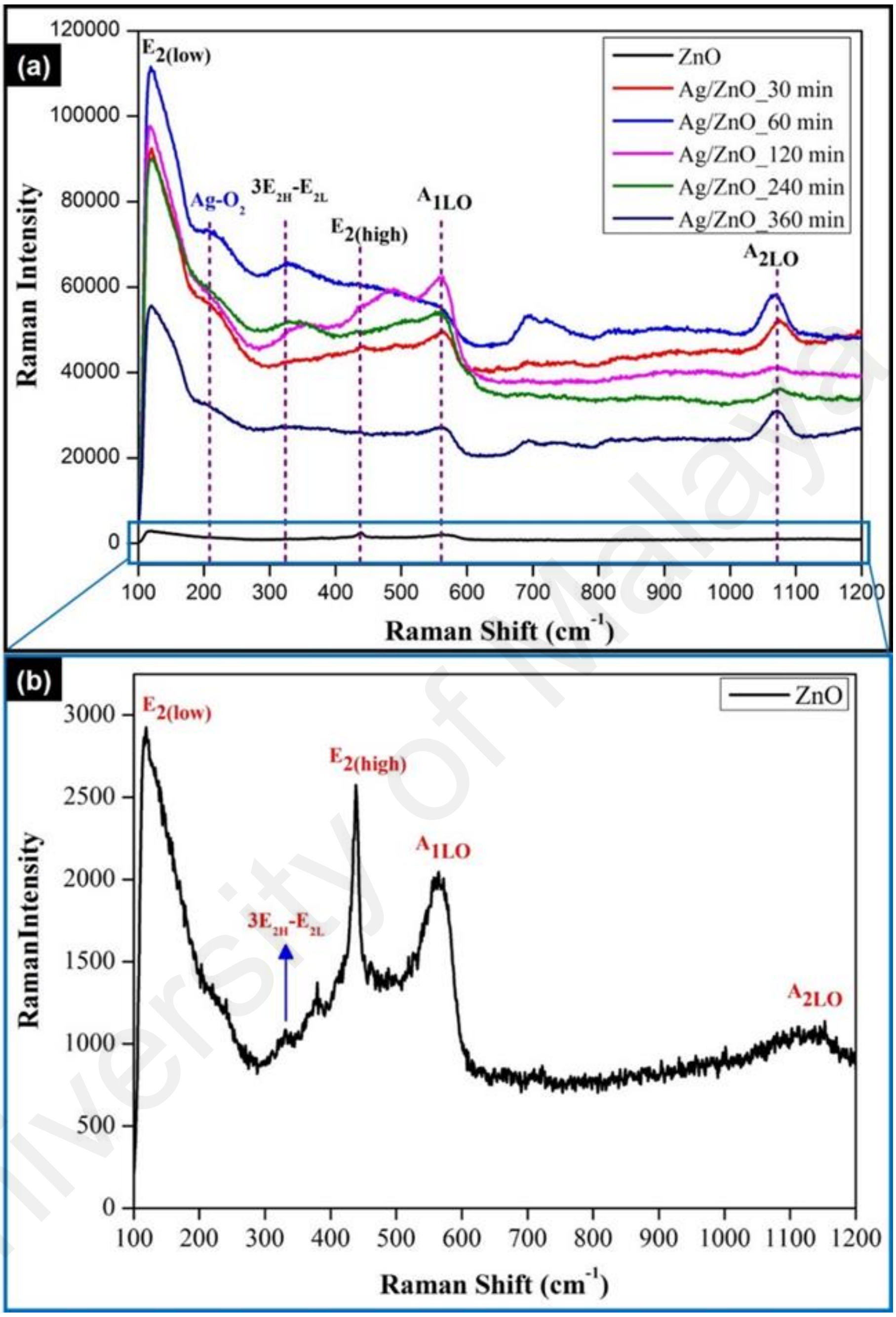

Figure 5.5: (a) Raman spectrum of ZnO nanopillars and Ag/ZnO heterostructures and (b) magnified Raman spectra of ZnO nanopillars

In addition, it is obviously seen that the Raman intensity of Ag/ZnO heterostructures have enhancement 40 times if compared to the Raman intensity of ZnO nanopillars. The enhancement of Raman intensity can be explained by two theories: (1) the electromagnetic theory which is based on the excitation of the localized surface plasmons and (2) chemical theory of the charge transfer which is only applies for species that formed a bond with the surface (Zamiri et al., 2014). Since the Raman intensity is relative to the intensity of the local *E*-field which can interact with optical phonons via enhancement of the scattering intensity of active phonons, thus the higher Raman intensity of Ag/ZnO heterostructures may due to the strong local E-field at the interface between ZnO and Ag. Since the work function of Ag (4.26 eV) is lower than the work function of ZnO (5.2 eV), electrons will be migrated from the Ag to the conduction band (CB) of ZnO to achieve Fermi level equilibrium. Hence, this will cause the formation of a strong polarization induced local *E*-field at the interface of Ag and ZnO due to the improved charge separation (Deng et al., 2012; Zamiri et al., 2014).

5.2.5 Diffuse Reflectance Analysis

UV-visible diffuse reflectance spectra of ZnO nanopillars and Ag/ZnO heterostructures at varied reduction period of Ag^+ ions are demonstrated in Figure 5.6(a). The absorption peak of ZnO nanopillars can be detected at UV region with the maximum absorption edge 370 nm, which is attributed to the intrinsic band gap absorption of ZnO due to the electron transition from the valance band to conduction band or specifically due to the electron transition from O_{2p} orbital to Z_{3d} orbital (Zak et al., 2011). Upon the integration of Ag nanoparticles on ZnO nanopillars, about 5 nm red-shift in absorption edge is observed for all Ag/ZnO heterostructures samples. The shifting of the absorption edge indicates a reduction in band gap energy as reported by Liang et al. and Whang et al. (Liang et al., 2016; Whang et al., 2015). Ag/ZnO_30 min sample has the highest absorption as observed in magnified region of Ag/ZnO heterostructures spectra in Figure 5.6(a). This is attributed to the so-called surface plasmonic resonance (SPR) of Ag nanoparticles (Wei et al., 2013; Dong et al., 2014; Liang et al., 2015).

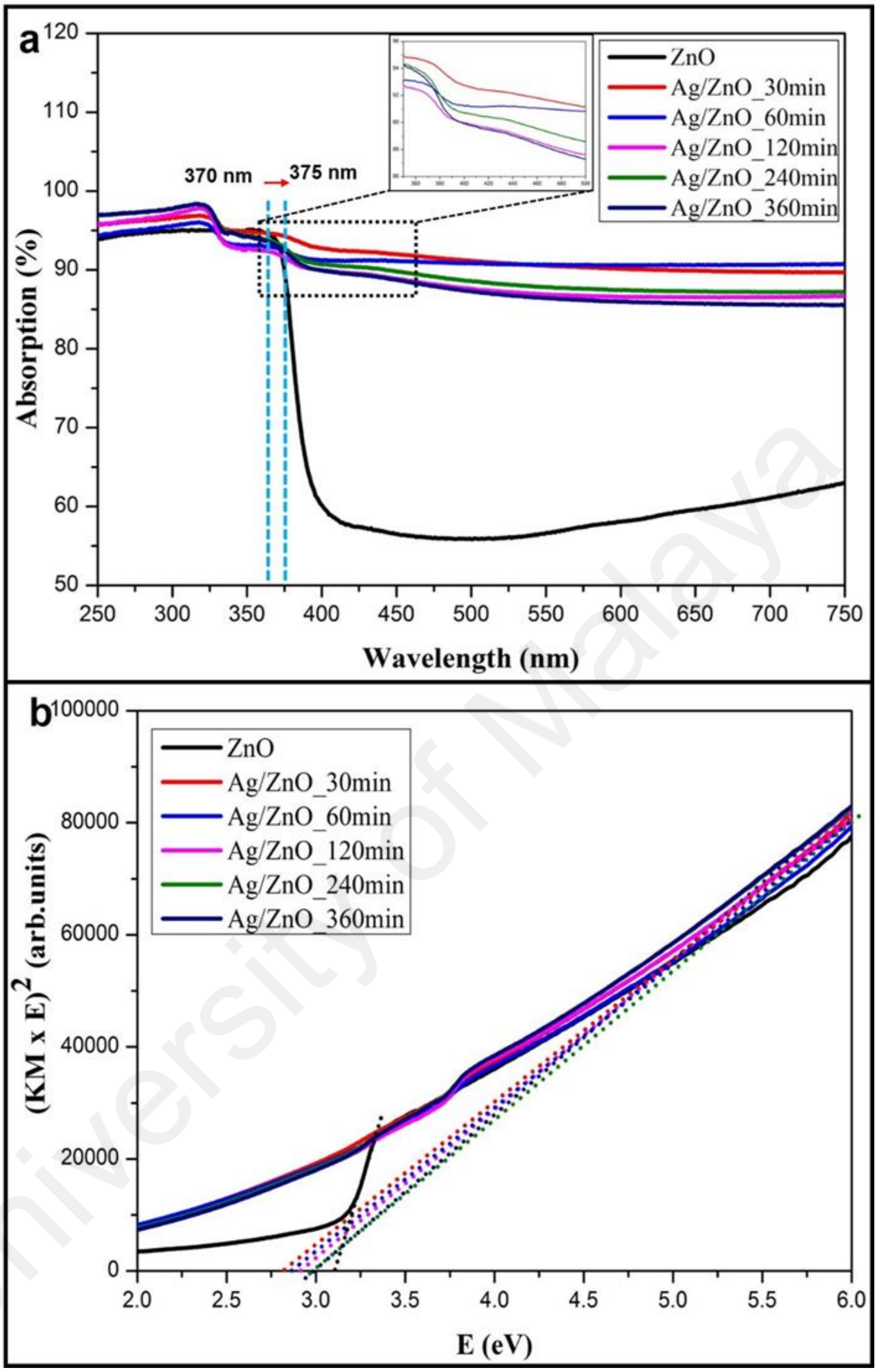

Figure 5.6: (a) UV-visible diffuse reflectance spectra of ZnO nanopillars and Ag/ZnO heterostructures, inset is the magnified region of Ag/ZnO heterostructures and (b) Energy band gap estimation through the Kubelka-Munk treatment

The interaction between the incident light and the smallest size of Ag nanoparticles decorated ZnO nanopillars at 30 min has enhanced the light scattering from SPR effect which then further aid to increase the path optical length. Thus, more light can be trapped resulting in the enhancement of absorption in the visible range (Wei et al., 2013). The absorption intensity for all samples that heated after 30 min reduction period is reduced and this may due to the larger sizes of Ag nanoparticles embedded on the surface of ZnO nanopillars. Also, due to agglomeration of Ag nanoparticles on the secondary branches of ZnO nanopillars, the SPR peaks could not be clearly seen and appeared as broad hump around 425 nm – 475 nm (Zamiri et al., 2014).

The energy band gap estimation of the samples through Kubelka-Munk treatment is presented in Figure 5.6(b) by extrapolating the linear region of absorption towards the intercepts with *x*-axis, the energy band gap of ZnO nanopillars is calculated to be 3.2 eV while for Ag/ZnO heterostructures samples, their energy band gap are gradually red-shifted from 3.0 eV to 2.88 eV as the reduction period of Ag^+ ions is reduced, in which Ag/ZnO_30 min appear to have lowest energy band gap. The estimated E_g for all samples are shown in Table 5.1. Such visible light active nature has rendered current sample as an ideal candidature to be utilized for visible light enhanced photoelectrochemical (PEC) water splitting application in producing a photoelectrochemical device that shows improved photocurrent density and hydrogen gas yield.

Table 5.1: Energy band gap estimation of ZnO nanopillars and Ag/ZnO heterostructures with different reduction period of Ag^+ ions

Sample	**Estimated energy band gap, E_g (eV) (± 0.05 eV)**
ZnO nanopillars	3.20
Ag/ZnO_30 min	2.88
Ag/ZnO_60 min	2.92
Ag/ZnO_120 min	2.94
Ag/ZnO_240 min	2.96
Ag/ZnO_360 min	3.00

5.2.6 PL Analysis

Figure 5.7 depicts the PL spectra of ZnO nanopillars and Ag/ZnO heterostructures with varying reduction period of Ag^+ ions that had been excited by 325 nm He – Cd laser. It is noticeably showed that ZnO nanopillars exhibits intense PL peak at the range of 550 nm – 650 nm in addition to the obvious peaks located at ~ 380 nm and 765 nm. Both of these peaks have been commonly assigned to the violet and red luminescence. Violet luminescence is originally emitted from near band edge resulting from the exciton recombination, while red luminescence is originated from the doubly oxidized oxygen vacancy (Peralta et al., 2012; Boppella et al., 2013; Daud et al., 2016). Meanwhile, the intense and slightly broad peak at the visible range has been attributed to the superposition of green and yellow emissions. ZnO commonly exhibits luminescence at visible region due to the recombination of photogenerated carriers with singly ionized charge states of the intrinsic defects consisted of oxygen vacancy, oxygen interstitial and Zn interstitial (Peralta et al., 2012; Zhang et al., 2014).

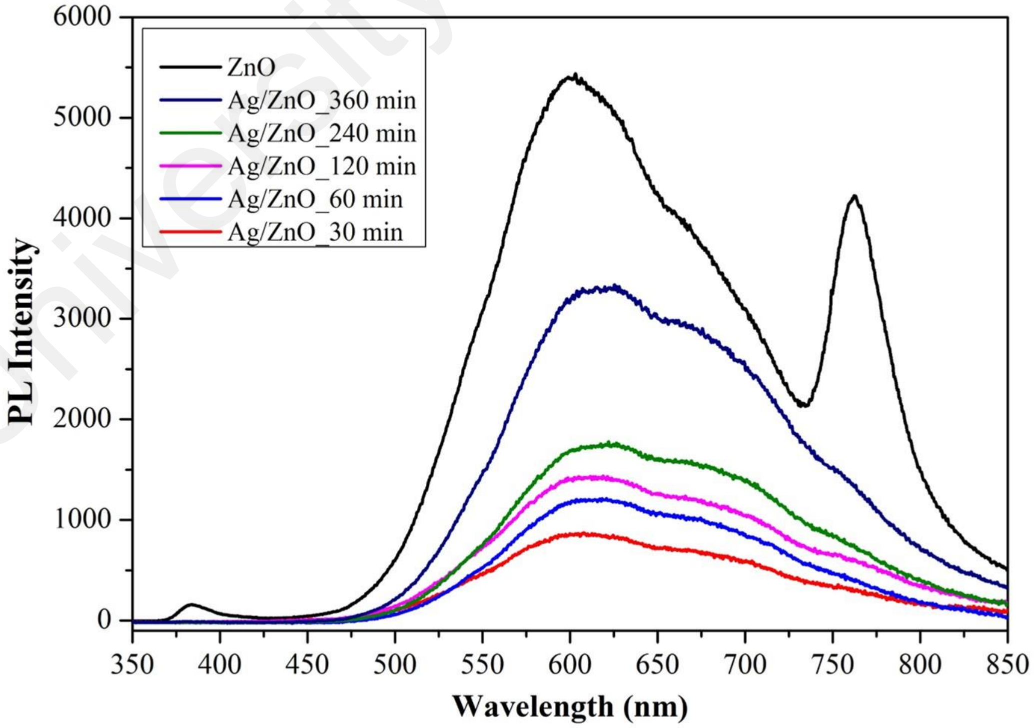

Figure 5.7: Photoluminescence spectra of ZnO nanopillars and Ag/ZnO heterostructures at varying reduction period of Ag^+ ions by two step hydrothermal approach

On the other hand, in contrast to that of pure ZnO nanopillars, all Ag/ZnO heterostructures depicts a progressive increment in the PL intensity (in violet-, red- and superposition of green and yellow emissions) with respect to the increment of reduction period. Such phenomena is attributed to the enhancement of charge transfer that contributed by the electron sink effect of noble metal (Ag nanoparticles on the surface of ZnO nanopillars), in which the Ag nanoparticles are proved to be able in functioning as a "electron pool" to collect and gather the photoexcited electron of ZnO nanopillars that will subsequently refrain the recombination. This deduction is well-complement with numerous of similar studies (Peralta et al., 2012; Cheah et al., 2015), where noble metals nanoparticles have been integrated onto the surface of semiconductors nanostructures to further promote the efficient electron-hole separation. Moreover, the progressive increment of PL intensity has direct correlation with the size of Ag nanoparticles as FESEM result reflects the increment of size of Ag nanoparticles in accordance to the extent of reduction period. It is expected the effect of SPR is greatly reduced with respect to the Ag nanoparticles size increment (Lerme, 2011; Mogensen & Kneipp, 2014). Therefore, larger size Ag nanoparticles produce less electric field that is essential to activate the migration of photoexcited electron from ZnO nanopillars to Ag nanoparticles. As a consequence, when the size of Ag nanoparticles increase, the charge separation efficiency is impeded and the intensity of PL is getting dominant.

With respect to the Figure 5.7, it is observed that the violet emission for all the Ag/ZnO heterostructures are diminished totally in comparison to that of pure ZnO nanopillars. This implies that little photoexcited electrons are being excited into conduction band and all these photoexcited electrons are tunnelled towards Ag nanoparticles and renders diminishing of violet emission for Ag/ZnO heterostructures in contrast to the pure ZnO nanopillars. Instead of conduction band of ZnO nanopillars, most of the photoexcited electrons are trapped into deep levels that can be associated to the native defects such as oxygen vacancy, oxygen interstitial and Zn interstitial, which finally renders superposition of green- and yellow- as well as red-emission. However, there is stepwise increment for superposition of green- and yellow-emission as well as red emission with respect to the prolonged of the reduction period. Eventually, all the photoelectrons that existed in the deep levels also will transfer towards Ag nanoparticles since the native defect energy level in ZnO nanopillars is proved to be higher than the Fermi energy level of Ag (Lu et al., 2008). Thus, facile charge separation remains take place but it is subjected to the contribution by SPRs effect that can be fine-tuned by manipulating the reaction duration.

5.2.7 Growth Mechanism

In order to understand the morphological evolutionary 3D hyperbranched ZnO nanopillars heterostructures, a possible crystallization process is proposed in Figure 5.8. The morphology formation can be attributed to the thermodynamic-driven effect where the growth mechanism of ZnO nanopillars could be explained by the following reaction routes (Kar & Santra, 2008; Li et al., 2009):

$$Zn \rightarrow Zn^{+} + e^{-} \tag{5.1}$$

$$H_2O \rightarrow H^{+} + OH^{-} \tag{5.2}$$

$$Zn^{+} + OH^{-} \rightarrow Zn(OH)_4^{2-} + H_2 \tag{5.3}$$

$$Zn(OH)_4^{2-} \rightarrow ZnO + H_2O + OH^{-} \tag{5.4}$$

During the nucleation process, the dissolution of Zn atoms in DI water causes the concentration gradient of Zn^+ ions in the area adjacent to the Zn foil. $Zn(OH)_4^{2-}$ ions are formed upon the reaction between Zn^+ and OH^- ions in DI water, in which these ions normally acts as the basis growth unit in the formation of ZnO nanostructures. The decomposition of these intermediate $Zn(OH)_4^{2-}$ ions will promote the nucleation of ZnO nuclei. The deposition and assembly of ZnO nuclei on the surface of Zn foil are driven by the electrostatic interaction from the polar charges in order to minimize the energy contributed by polar charges and surface area (Li et al., 2009). The ZnO nuclei functions as the building blocks for the formation of final products. Basically, due to the crystalline nature of ZnO that having hexagonal phase crystal structure, those nuclei possess the hexagonal shape (Ahsanulhaq et al., 2007; Cai et al., 2014; Hsu et al., 2015).

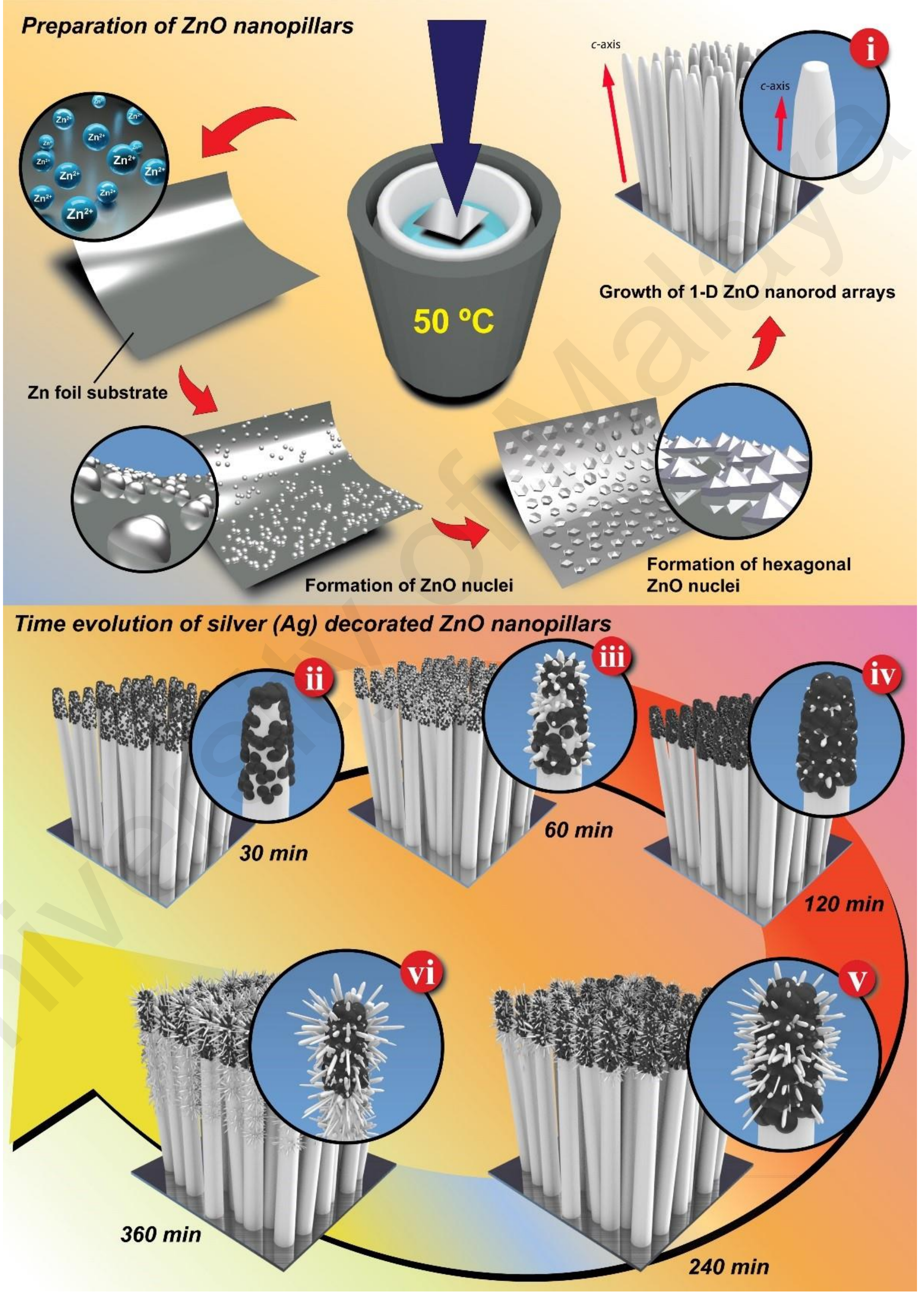

Figure 5.8: Schematic diagram of growth mechanism of (i) ZnO nanopillars and (ii-vi) Ag nanoparticles integrated ZnO nanopillars at different Ag^+ ions reduction time

Structurally, ZnO crystal lattice can be described as alternating planes that composed of Zn^{2+} and O^{2-}, which is stacked along *c*-axis. Polarization along *c*-axis is resulted by the oppositely charged ions that create an alternatively-stacking positively-charged Zn (0001) and negatively-charged O $(000\bar{1})$ surfaces. The growth rate of different planes in the ZnO crystal can influence the growth of final product, whereby the slowest growing faces will determine the morphology of a particular crystal. For hydrothermal synthesis condition, the growth of ZnO crystals are following [0001] > $[01\bar{1}\bar{1}]$ > $[01\bar{1}0]$ > $[01\bar{1}1]$ > $[000\bar{1}]$, stating that the polar (0001) facet has the most rapid growth as compared to the other growth facets. Hence, this has explained that the most stable ZnO crystalline structure should be a prism grown along the *c*-axis whereby the side facet of the prism are consisted of six equivalent non-polar crystal planes which is $(10\bar{1}0)$, $(1\bar{1}00)$, $(0\bar{1}10)$, $(\bar{1}010)$, $(\bar{1}100)$ and $(01\bar{1}0)$ (Cai et al., 2014). As proven in Figure 5.1(a), the nanopillars synthesized in DI water medium at 50 °C are consistent with the typical growth habit of ZnO crystal in which exhibiting polar Zn-terminated (0001) on the top and O-terminated $(000\bar{1})$ at the bottom of surfaces with bounded with six crystallographic non-polar planes.

Additionally, hexagonal ZnO nuclei can act as the seed layer in which these primary nuclei can serve as nucleation sites for desired pillar-like structure of ZnO. The interfacial energy between the ZnO crystal nuclei and the substrate (Zn foil) can be lowered by the induction of seed layer, whereby decreases the nucleation barriers and finally facilitates the growth of ZnO nanopillars. Furthermore, the ZnO seed layer also enhances the surface roughness of Zn foil and increases the formation of more vacancies which is assisting the promotion of ZnO nanopillars (Warule et al., 2011). In addition to the role of the ZnO seed layer which is helping in the formation of ZnO nanopillars, the intrinsic electric field of polar ZnO lattice could be also responsible for the further growth of hexagonal ZnO nuclei into pillar-like structure (Kar & Santra, 2008). Moreover, the presence of excess

OH^- ions and continual dissolution of Zn atoms at constant 50 °C for 24 hours duration further maintains the uniform growth of ZnO nanopillars along the *c*-axis.

It is important to know the orientation mechanism of 1D ZnO nanostructures since their orientation on the substrate is crucial for most device applications. As evidenced in FESEM results, ZnO nanopillars are appeared to be unidirectional and vertically oriented. The formation of vertical orientation of ZnO nanopillars could be due to the interaction between nanopillars and their coupling to the substrates. According to theoretical analysis of Titov and Král, a single nanopillar will preferentially orient in a horizontal manner because its side-to-substrate coupling (van der Waals interaction between the side of the rod and substrate) is significantly stronger than its face-to-substrate coupling (van der Waals interaction between end face of the rod and the substrate) and vice-versa (Titov & Král, 2008; Zhang et al., 2014). On the other hand, van der Waals interaction between end face of ZnO nanopillars and the Zn foil is stronger enough to render the formation of vertical orientation of ZnO nanopillars.

As depicted in Figure 5.1(c) and illustrated in Figure 5.8(iii), when reduction time was prolonged to 60 min, branched of tiny pillars are grown and sprouted on the edges of the upper half of primary ZnO nanopillars which render the formation of “broccoli-like” morphology of ZnO. This indicates that primary ZnO nanopillars are underwent secondary nucleation process and the mechanism formation of secondary ZnO nanopillars are almost similar to the primary ZnO nanopillars. In order to gain more mechanistic insight into how the secondary nucleation takes place and the reason of branching that only grow on the edges of the upper half of primary ZnO nanopillars, a careful examination on the magnified region of primary ZnO nanopillars (Figure 5.9(a)) was conducted.

With respect to the magnified FESEM of primary ZnO nanopillars, it depicts that the formation of rough surface or defects at the tip and upper half of primary ZnO nanopillars.

It is believed that these rough surfaces or defects were served as a pin-point or nucleation sites for the secondary nucleation to be realized and resulting in the formation of branching pillars at these areas (Sounart et al., 2007; Kar & Santra, 2008). However, the length of branched and sprouted secondary ZnO pillars are reduced when reduction period was prolonged to 120 min (as evident in Figure 5.1(d) and illustrated in Figure 5.8(iv)) and become even longer at 240 min reduction time (shown in FESEM result of Figure 5.1(e)). This growth mechanism is analogous to the Ostwald ripening process whereby the most energetically favourable orientation ZnO nuclei that grown at the expense of the misaligned crystals are dissolved and recrystallized by epitaxial growth on the oriented crystals and further grow larger at a higher rate along the *c*-axis (due to higher energy of (0001) plane). This process is occurred in order to minimize the interfacial energy between the new ZnO crystals and the secondary ZnO nanopillars, in which this process lowers the overall energy of the system after the nucleation burst (Sounart et al., 2007). There are no significant any changes on the length of branched secondary ZnO nanopillars at 360 min reduction time (as depicted in Figure 5.1(f)) due to the supersaturation of Zn^+ ions concentration.

The fundamental formation of Ag nanoparticles on the tips of ZnO nanopillars with preferred reduction period of Ag^+ ions are illustrated in Figure 5.10 with the reaction mechanism of Ag nanoparticles can be expressed by using following equations:

$$AgNO_3 \rightarrow Ag^+ + NO_3^- \tag{5.5}$$

$$Ag^+ + e^- \rightarrow Ag \tag{5.6}$$

$$NO_3^- + H^+ \rightarrow HNO_3 \tag{5.7}$$

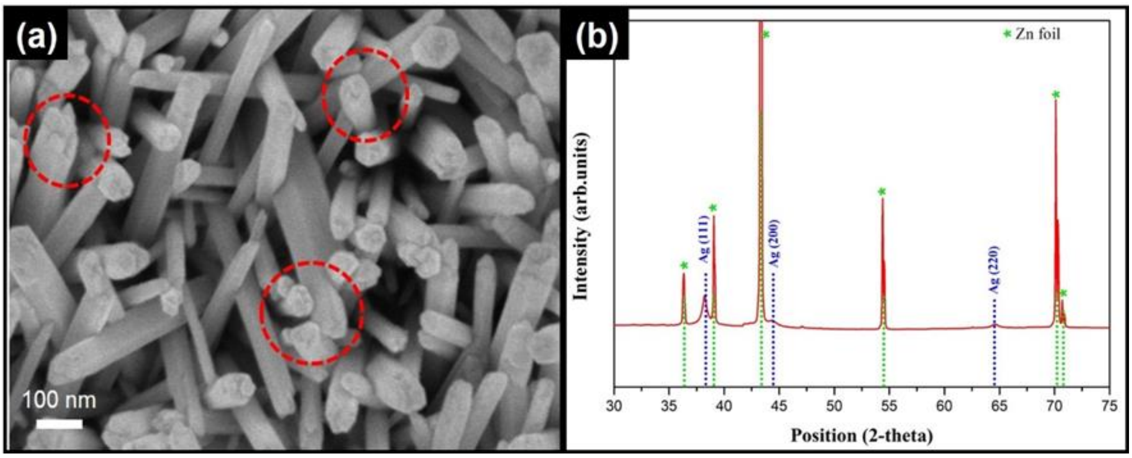

Figure 5.9: (a) Magnified region of primary ZnO nanopillars where the red dotted-circles show the rough surface or defects formed on the tips and upper half edges of nanopillars and (b) XRD pattern of metallic Ag on the surface of Zn foil

$AgNO_3$ precursor with 1mM concentration is decomposed to form Ag^+ ions and NO_3^- ions at constant 50 °C. By referring to the Equation 5.1, the dissolution of Zn foil also generate the electrons whereby the electrons assist in the reduction of Ag^+ ions to become metallic Ag nuclei. It is hypothesized that Zn foil can act as reducing agent of Ag^+ ions by releasing electrons that later will react with Ag^+ ions. In order to further confirm this hypothesis, an experiment was conducted by dipping Zn foil inside the $AgNO_3$ aqueous solution for a few minutes. As a results, black precipitates are deposited on the surface of Zn foil. After that, this sample was measured by XRD to confirm the elemental composition. The XRD result as depicted in Figure 5.9(b) shows that the black precipitates are Ag and also with the presence of Zn peaks, indicating Zn as a substrate. This further confirmed that Zn foil can be a reducing agent to reduce Ag^+ ions to form metallic Ag. The role of generated electrons that aiding the reduction of Ag^+ ions also reported by Li et al. and Ansari et al (Li et al., 2013; Ansari et al., 2013). Additionally, these generated electrons also aid in anchoring metallic Ag nanoparticles on the tips of primary ZnO nanopillars at 30 min reduction time (Ansari et al., 2013).

As illustrated in Figure 5.10, Ag^+ ions are reduced by Zn foil with the assistance of generated electrons to form the Ag nuclei (Equation (5.6)). Ag will then randomly deposited on the tip of ZnO as depicted in FESEM result (Figure 5.1(b)). When the reduction period was increased, the Ag nanoparticles will further grow due to aggregation and coalescence process, in which two smaller crystals with similar size are attaching together to produce larger crystals (Thanh et al., 2014).

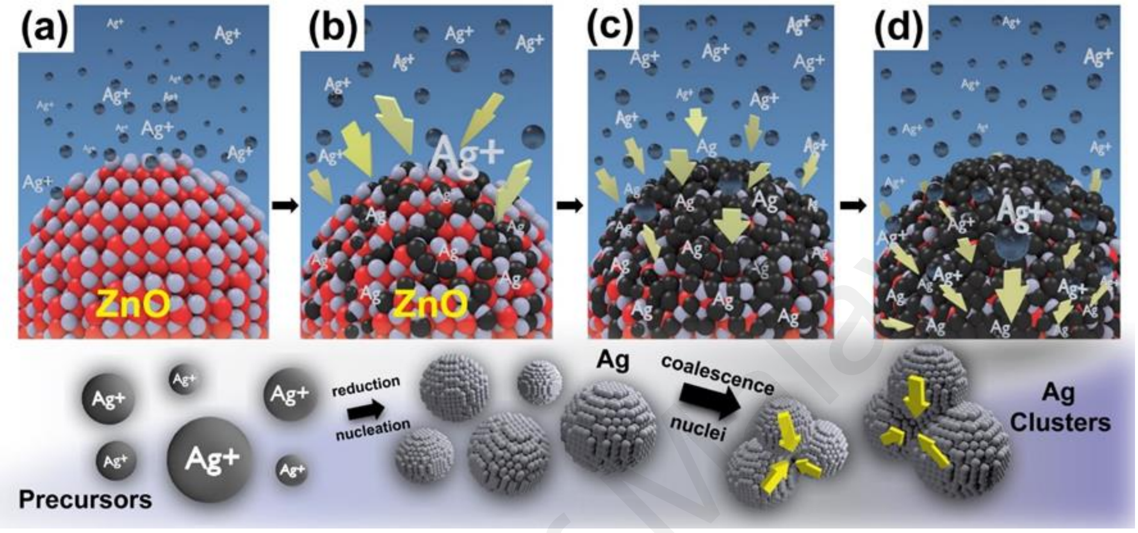

Figure 5.10: Fundamental formation of Ag nanoparticles on tips of ZnO nanopillars with (a-b) preferred reduction period of Ag^+ ions selectively focusing on the top regions of the ZnO tips and (c-d) Formation of Ag clusters as a result of nuclei coalescence takes place on as-deposited Ag nanoparticles due to high surface energy of Ag nanoparticles

According to general principle of coalescence mechanism, if aggregation barrier is below the thermal energy of crystals, then the crystal will aggregates and subsequently coalesce with each other. On the other hand, if the aggregation barrier is above the crystals thermal energy, the colloidal stability is sufficient enough to prevent further growth (Polte, 2015). It is postulated that the aggregation barrier is lower than the Ag nanoparticles thermal energy, then Ag was coalesced to from larger nanoparticles. As proven in FESEM analysis, the size of Ag nanoparticles that deposited on ZnO nanopillars were increasing when the reduction time was extending. At prolonged time of 240 min and 360 min, more electrons were released and resulting in more Ag^+ ions were reduced. This caused more Ag metal sites formed on the surface of ZnO nanopillars which then finally produce a bigger size of Ag nanoparticles and agglomeration occurred

(Wu et al., 2013). Ag metal sites could be referred as site-specific deposition of Ag nanoparticles that involve a preferentially small lattice mismatch between Ag and ZnO at respective crystallographic plane (Pacholski et al., 2004; Wang et al., 2013).

5.3 Sensitization of Ag Nanoparticles on ZnO Nanopillars via the $AgNO_3$ Salt Concentration

The study is further continued by fabricating Ag/ZnO heterostructures with different $AgNO_3$ salt concentration. All samples were synthesized via two facile steps hydrothermal method at 50 °C for 30 minutes. The full procedure can be referred in Chapter 3.3.3.2. The characterization for all samples as well as the growth mechanism will be discussed in the following section.

5.3.1 FESEM Analysis

The morphology micrograph of bare ZnO nanopillars as well as Ag nanoparticles integrated ZnO nanopillars that were hydrothermally prepared with varied $AgNO_3$ salt concentration are depicted in Figure 5.11. ZnO nanopillars underwent the crystallization process in DI water medium and densely direct grown on Zn foil as displayed in Figure 5.10(a). ZnO nanopillars that possessed blunt-terminated tip with average length of ~600 – 700 nm will be sensitized with Ag nanoparticles, in which the concentration-dependent study was systematically conducted by varying $AgNO_3$ salt concentration from 0.2 mM – 5 mM and their morphology evolution are shown in Figure 5.11(b-f). Figure 5.11(b) depicts Ag nanoparticles sensitized ZnO nanopillars at 0.2 mM concentration where Ag nanoparticles are randomly decorated on the blunt-terminated tips of ZnO nanopillars. As the $AgNO_3$ salt concentration was increased up to 0.4 mM, Ag nanoparticles are abundantly crystallized on the as-deposited Ag nanoparticles and smaller nanoparticles are clearly seen integrated on the upper half of ZnO nanopillars as well as depicted in Figure 5.11(c).

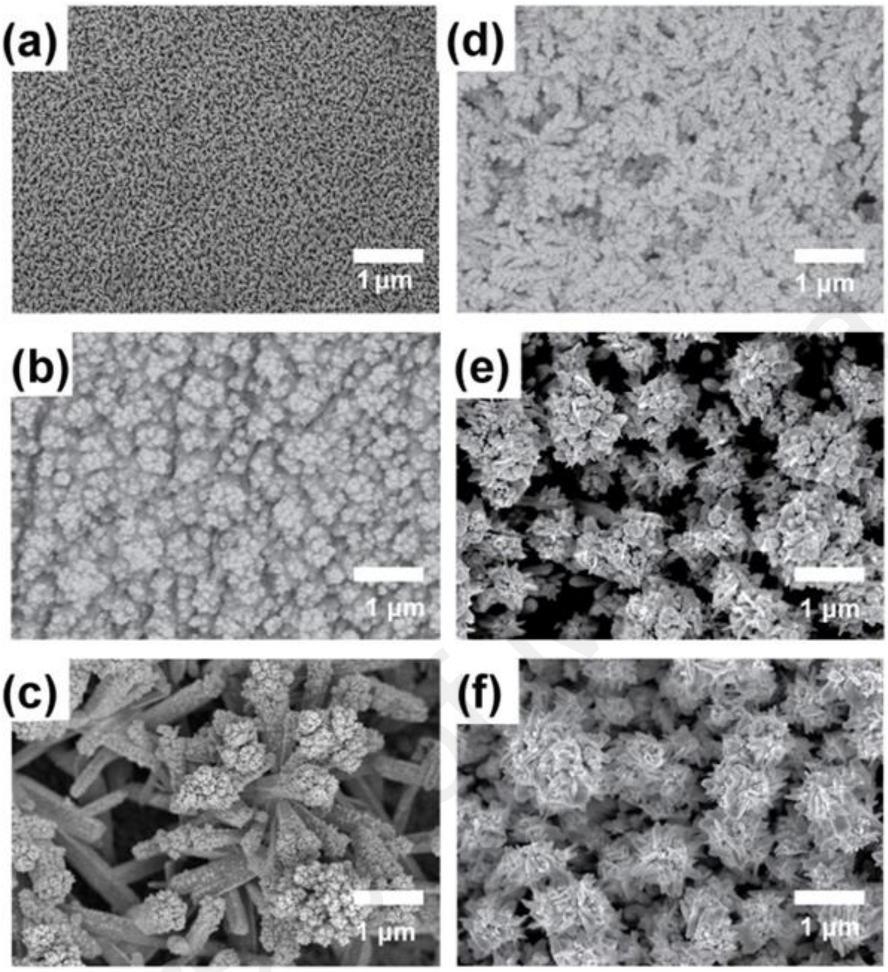

Figure 5.11: FESEM micrograph of (a) ZnO nanopillars, (b) Ag/ZnO_0.2 mM, (c) Ag/ZnO_0.4 mM, (d) Ag/ZnO_1 mM, (e) Ag/ZnO_2 mM and (f) Ag/ZnO_5 mM

Due to the aggregation of Ag nanoparticles, the particle size of the nanoparticles cannot be precisely measured but qualitatively the size of particle is increased when the concentration of $AgNO_3$ is increased. At 1 mM of $AgNO_3$ salt concentration, the quantity of Ag nanoparticles are increased and densely covered the surface of ZnO nanopillars as shown in Figure 5.11(d). Surprisingly, an irregular shape of ZnO tiny branches are secondarily grown at the upper half of primary ZnO nanopillars with bigger particle size of Ag nanoparticles are randomly deposited on them at concentration of 2 mM. When the concentration is increased up to 5 mM, an irregular shape of ZnO branches were getting larger with the integration of increment on the diameter of Ag nanoparticles makes those morphologies can be visualized as flower-like structure as depicted in Figure 5.11(f).

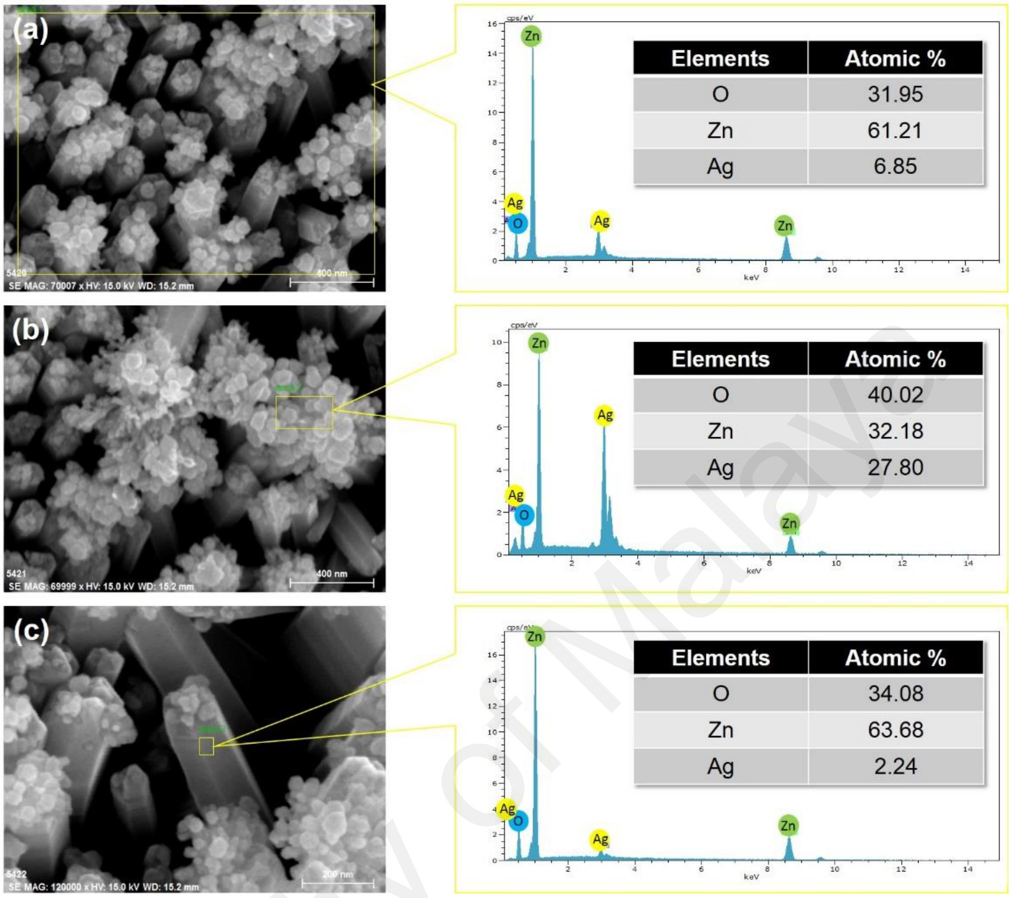

Elements	Atomic %
O	31.95
Zn	61.21
Ag	6.85

Elements	Atomic %
O	40.02
Zn	32.18
Ag	27.80

Elements	Atomic %
O	34.08
Zn	63.68
Ag	2.24

Figure 5.12: EDX-FESEM analysis of Ag/ZnO_1 mM at (a) overall surface, (b) area of Ag nanoparticles and (c) primary nanopillars

As a complement, EDX analysis has been conducted as well to study the elemental composition of sample Ag/ZnO_1 mM as depicted in Figure 5.12. According to the overall scan of Ag/ZnO_1 mM sample (Figure 5.12(a)), it is proven that the as-prepared consisted of ZnO and Ag elements. Figure 5.12(b) shows the scan of Ag nanoparticles whereby Zn and O elements have higher atomic percentage if compared to that of Ag element. During the measurement, signal of Zn and O are collected as well as Ag nanoparticles are deposited on the tips of ZnO nanopillars. The scan at the area of pillar-like structure (Figure 5.12(c)) shows that Zn and O element have the highest atomic percentage in which, this further confirm that nanopillars are consisted of ZnO.

Furthermore, the relative atomic ratios of Zn:O are determined to be 1:1, which is consistent to the stoichiometry ratio of ZnO.

5.3.2 HRTEM Analysis

Detail analysis was further conducted by characterizing Ag/ZnO_1 mM sample through HRTEM technique. The low-magnification image of sample is depicted in Figure 5.13(a) where Ag nanoparticles are randomly deposited on the surface of ZnO nanopillars. In order to clearly observe the distribution of Ag nanoparticles, high-magnification image has been collected and shown in Figure 5.13(b). With respect to the image, various size of Ag nanoparticles are distributed over the surface of ZnO nanopillars. High-resolution TEM image is provided in Figure 5.13(c) for a better comprehension of the interfacial bonding between the face-centred cubic phase and the wurtzite hexagonal phase. In order to clearly view the lattice fringes, three distinctive regions have been selected as depicted in Figure 5.13(c). With respect to the square area of d, the interplanar spacing is estimated to be 0.26 nm which corresponds to the (002) lattice fringe of hexagonal wurtzite structure of ZnO nanopillars. Electron diffraction at this spot can be assigned to zone axis of $[\bar{1}\bar{1}1]$ as illustrated in Figure 5.13(d). At the same time, region e shows the interface in between ZnO nanopillars and Ag nanoparticles and its corresponding FFT analysis pattern (Figure 5.13(e)) reveals the presence of combination of diffraction for both ZnO and Ag crystal structure. According to the diffraction spots, the yellow colour circled spots can be attributed to the diffraction signal that belongs to ZnO hexagonal wurtzite structure for (002) and (110) planes.

Furthermore, the white colour circled spots indicate the diffraction signal of Ag face-centred cubic structure phase for the crystal planes of (111) and $(\bar{2}00)$. Hence, all these cruel have further confirmed that Ag nanoparticles are attached onto the surface of ZnO nanopillars. Further analysis in region (f) clearly represents the structure of Ag with an interplanar distance of 0.23 nm that corresponds to (111) lattice fringe, whereby this area belongs to $[0\bar{1}1]$ zone axis as depicted in Figure 5.13(f).

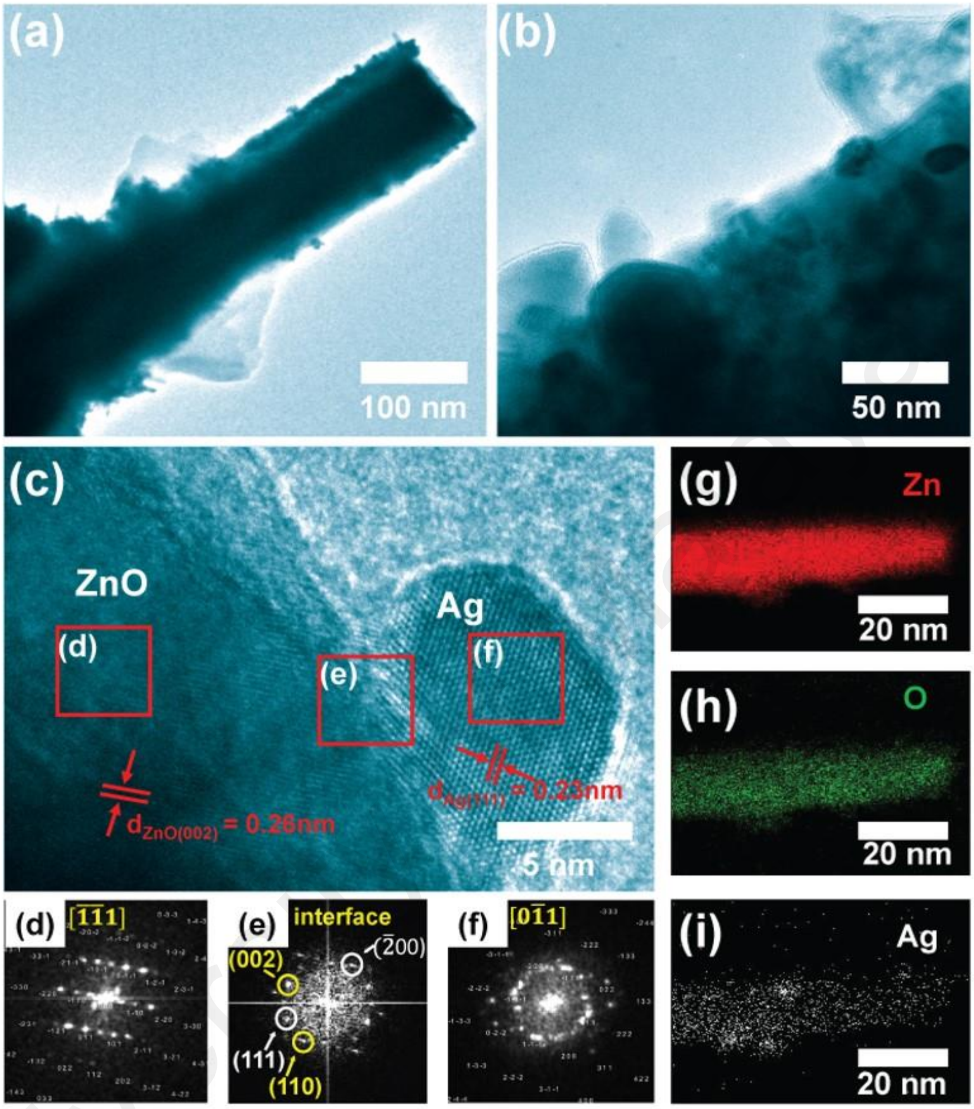

Figure 5.13: HRTEM image of Ag/ZnO_1 mM with (a) low-magnification image, (b) high-magnification image, (c) high-resolution TEM image of three selected regions indicate the interfacial distance of ZnO, interface of Ag/ZnO and Ag, respectively, (d-f) FFT analysis of ZnO, interface Ag/ZnO and Ag, respectively and (g-i) respectively show the elemental mapping of Zn, O and Ag

In addition, elemental mapping was conducted onto this sample during TEM analysis and the outcomes are displayed in Figure 5.13(g-i). According to those images, Zn and O are well-distributed along the pillar-like structure with Ag nanoparticles are randomly distributed on the surface of pillar-like structure of ZnO. With respect to the TEM and FESEM analysis, it is proven that the current approach with varying $AgNO_3$ salt concentration has successful in integrating Ag nanoparticles onto the surface of ZnO nanopillars as well.

5.3.3 XRD Analysis

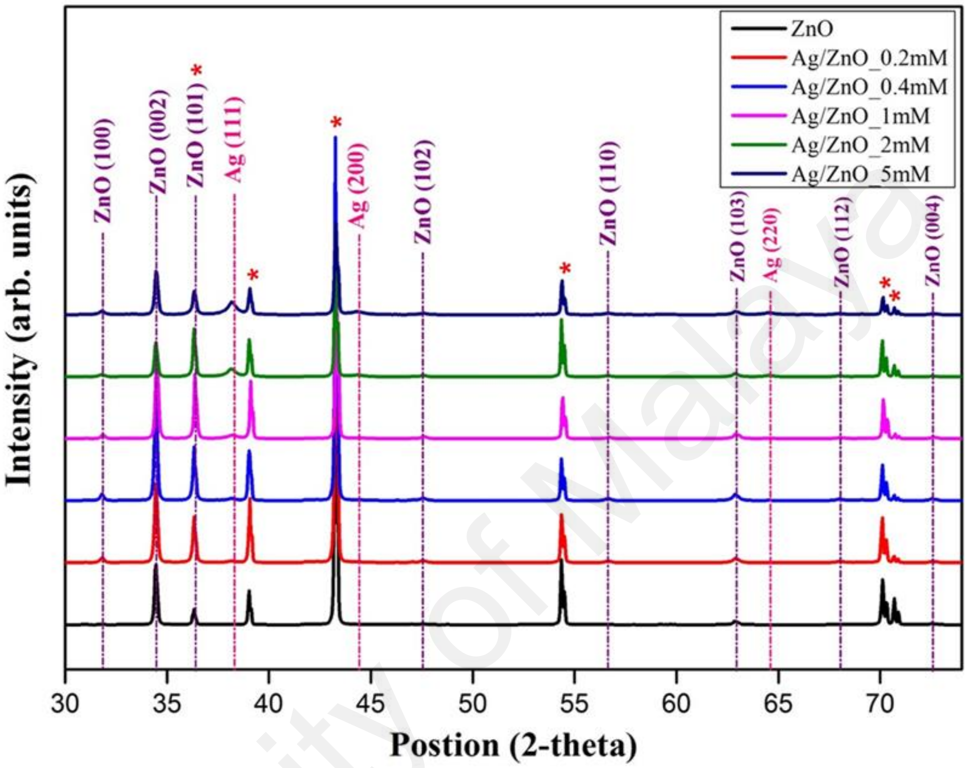

Figure 5.14: XRD pattern of ZnO nanopillars and Ag/ZnO heterostructures that synthesized with different concentration of $AgNO_3$ salt

The phase composition and bulk crystal structure of ZnO nanopillars and Ag/ZnO heterostructures that synthesized with varied $AgNO_3$ salt concentration are analyzed by XRD and displayed in Figure 5.14. All of the samples are well-crystallized and the diffraction peaks could be perfectly indexed to both of the hexagonal wurtzite ZnO (JCPDS no: 36-1451) and face-centred cubic Ag (JCPDS no: 04-0783). The peaks located at 38.1°, 44.2° and 64.4° are belong to Ag with crystal planes of (111), (200) and (220), respectively. Furthermore, peak of Zn foil which is labelled with star also present in all of the samples. Such distinguishable crystal spectrum with multiple peaks that contributed by different constituent compounds imply that all the as-integrated samples are indeed heterostructures without alloying as complement to the observation by FESEM and HRTEM. Also, there is no any impurity peaks detected, which further confirmed that the as-obtained heterostructures are pure.

5.3.4 Raman Analysis

Raman analysis of ZnO nanopillars and Ag nanoparticles decorated ZnO nanopillars with different $AgNO_3$ salt concentration are depicted in Figure 5.15(a) in the range of 100 – 1200 cm^{-1}. In order to clearly distinguish the Raman pattern of pure ZnO nanopillars, magnified spectra has been plotted as shown in Figure 5.15(b). The Raman results of this study are almost similar to the previous study (refer to Section 5.2.4) where peak of 100 cm^{-1} and 438 cm^{-1} are assigned to E_2 (low) and E_2 (high) peaks of hexagonal wurtzite ZnO, respectively which indicates the highly crystalline nature of the sample. Meanwhile, peak 330 cm^{-1} can be attributed to the $3E_{2H-2L}$ multi-phonon vibration in which this peak is related to multi-phonon process, or it is also described to second order Raman spectrum arising from the zone boundary phonon (Deng et al., 2012).

In addition, peak located in the range of 550 – 600 cm^{-1} and 1050 – 1100 cm^{-1} can be attributed to polar mode A_1 symmetry with 1LO and 2LO, respectively (Yin et al., 2012; Chia et al., 2015). Upon the integration of Ag nanoparticles, the characteristic peaks that possessed by ZnO nanopillars remain exist except there is a broad band peak located ~225 cm^{-1} is observed for all Ag/ZnO heterostructures samples where this peak can be assigned to the $Ag-O_2$ of the molecular oxygen species that chemisorbed on the defects of Ag (Millar et al., 1995). This is further proved by Deng et al., in which their study also reported the similar characteristic peak (Deng et al., 2012). With respect to the Figure 5.15, it is obviously depict that the Raman intensity of Ag/ZnO heterostructures have enhancement 100 times if compared to the Raman intensity of ZnO nanopillars and the explanation of Raman intensity enhancement can be referred to Chapter 5.2.4.

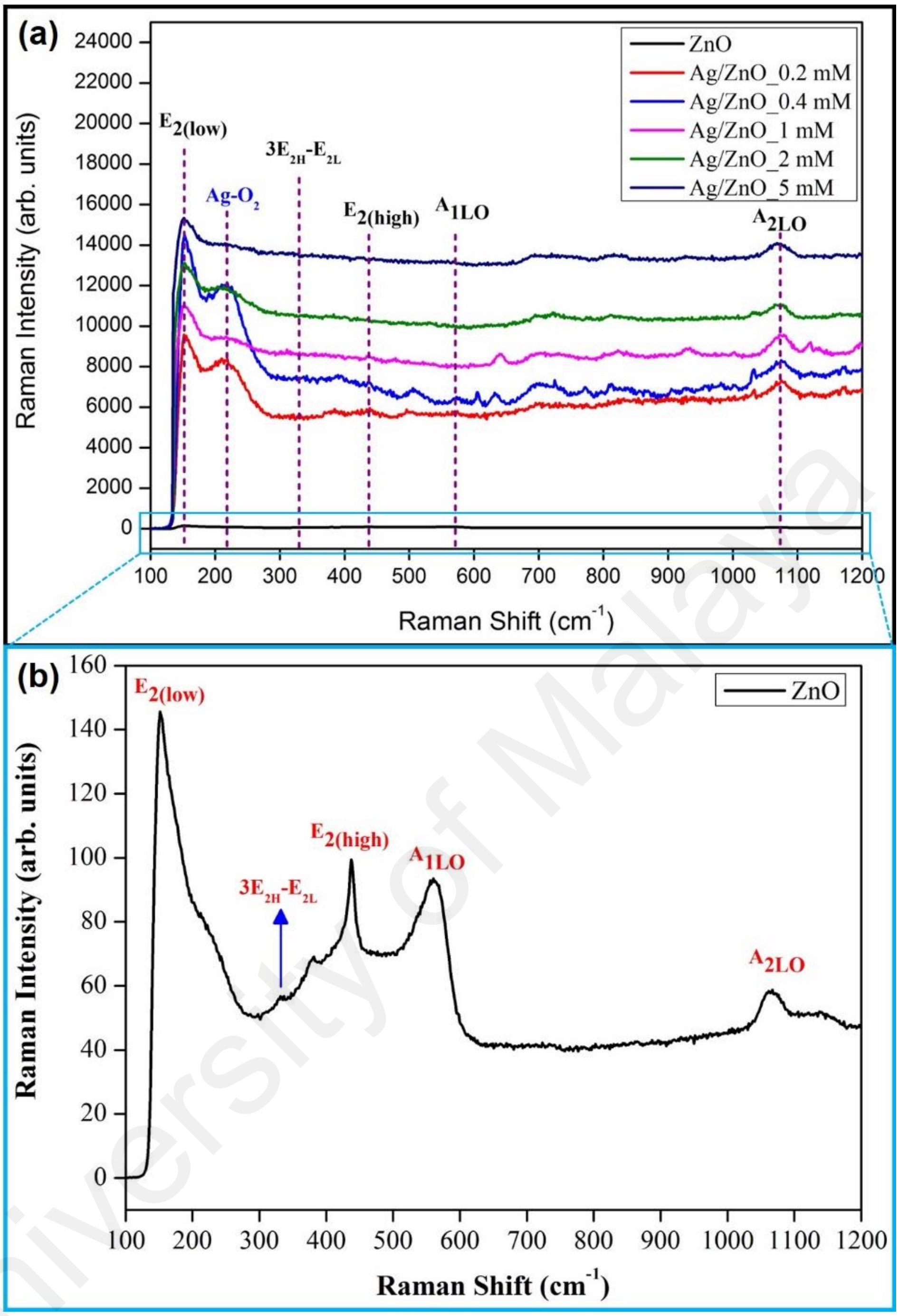

Figure 5.15: (a) Raman spectrum of ZnO nanopillars and Ag/ZnO heterostructures with varied $AgNO_3$ salt concentration and (b) magnified spectra of ZnO nanopillars

5.3.5 Diffuse Reflectance Analysis

The absorption spectra of ZnO nanopillars and Ag nanoparticles sensitized ZnO nanopillars with different $AgNO_3$ salt concentration are shown in Figure 5.16(a). The absorption peak of ZnO nanopillars can be detected at UV region with the maximum absorption edge 370 nm, which is attributed to the intrinsic band gap absorption of ZnO due to the electron transition from the valance band to conduction band or specifically due to the electron transition from O_{2p} orbital to Z_{3d} orbital (Zak et al., 2011).

After the integration of Ag nanoparticles, all of the samples show the absorption in the visible range which Ag/ZnO_1 mM sample has the highest absorption. The enhancement is due to the SPR of Ag nanoparticles (Wei et al., 2013; Dong et al., 2014; Liang et al., 2015). Meanwhile, Ag/ZnO sample with 0.2 mM concentration depicts the lowest absorption increment due to the lower Ag loading on the pillars surface (Zhang et al., 2014). Also, due to increase Ag loading and agglomeration on ZnO nanopillars, the SPR peaks could not be clearly seen and appeared as broad hump around 425 nm – 475 nm (Zamiri et al., 2014).

The estimation of energy band gap for all samples via Kubelka-Munk treatment is demonstrated in Figure 5.16(b). Regarding to the analysis, energy band gap of ZnO nanopillars is estimated to be 3.10 eV while energy band gap of Ag/ZnO heterostructures are reduced from 2.95 eV to 2.80 eV, in which Ag/ZnO_1 mM has the lowest energy band gap. The estimated E_g for all samples are shown in Table 5.2.

Table 5.2: Energy band gap estimation of ZnO nanopillars and Ag/ZnO heterostructures with different $AgNO_3$ salt concentration

Sample	Estimated energy band gap, E_g (eV) (± 0.04 eV)
ZnO nanopillars	3.10
Ag/ZnO_0.2 mM	3.00
Ag/ZnO_0.4 mM	2.85
Ag/ZnO_1 mM	2.80
Ag/ZnO_2 mM	2.90
Ag/ZnO_5 mM	2.95

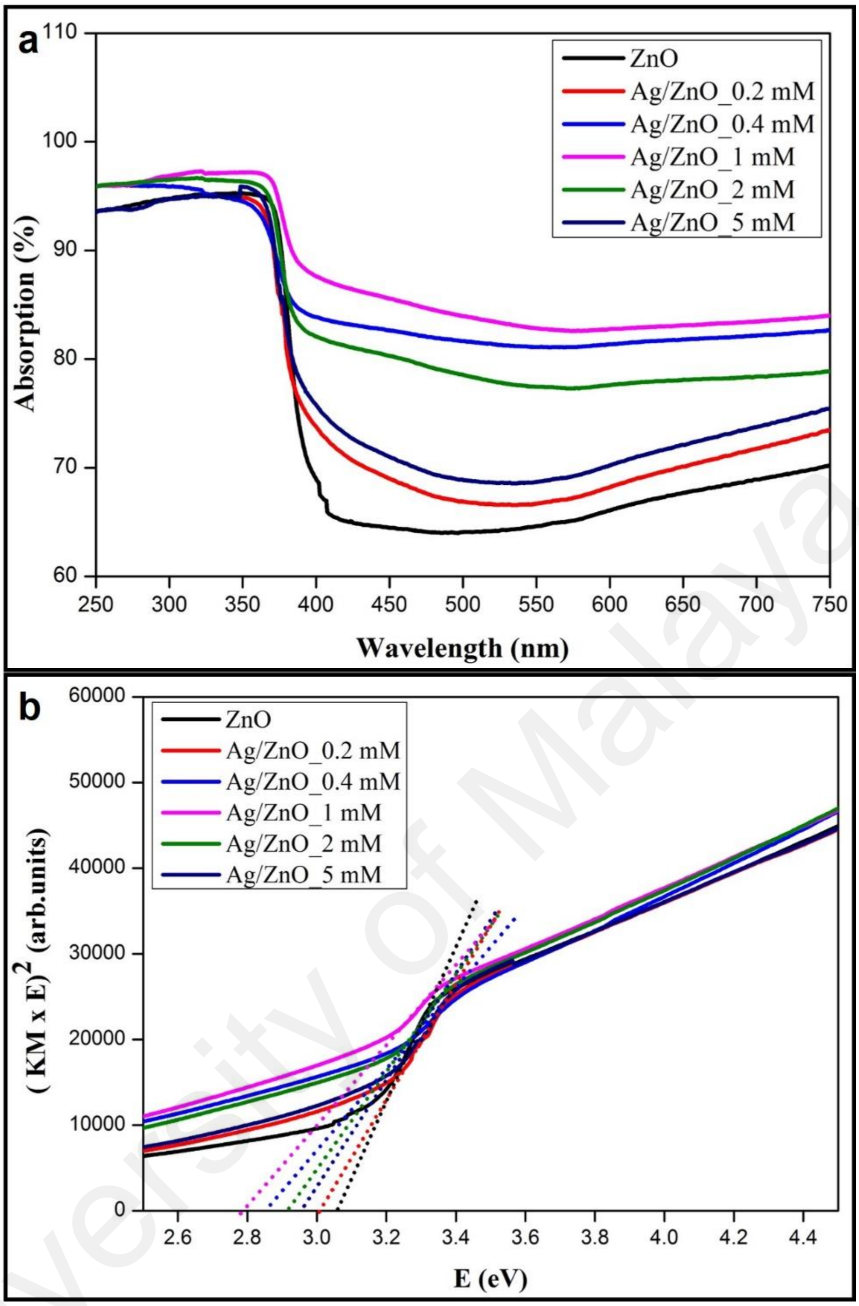

Figure 5.16: (a) UV-visible diffuse reflectance of ZnO nanopillars and Ag nanoparticles decorated ZnO nanopillars at different AgNO$_3$ salt concentration and (b) Energy band gap estimation via Kubelka-Munk treatment

5.3.6 PL Analysis

PL spectra of ZnO nanopillars and Ag nanoparticles decorated ZnO nanopillars at different AgNO$_3$ salt concentration are displayed in Figure 5.17. It is obviously depicted that ZnO nanopillars exhibits most intense PL peak in the range of 550 – 700 nm in addition to the noticeable peaks located at ~380 nm and 760 nm. Both of these peaks have been commonly attributed to the violet and red luminescence, in which violet luminescence is emitted from near band edge resulting from the recombination of exciton, while red luminescence is originated from the doubly oxidized oxygen vacancy (Peralta et al., 2012; Bopella et al., 2013; Daud et al., 2016). Meanwhile, the intense and slightly broad peak in the visible range can be assigned to the superposition of green and yellow luminescence. ZnO exhibited emission in the visible region commonly due to the recombination of photogenerated carriers with singly ionized charge states of the intrinsic defects such as oxygen vacancy, oxygen interstitial and Zn interstitial (Peralta et al., 2012; Zhang et al., 2014).

In contrast to that of pure ZnO nanopillars, all Ag/ZnO heterostructures depict a reduction in the PL intensity (in violet-, red- and superposition of green and yellow emissions) with respect to the sample of Ag/ZnO 0.2 mM to 1 mM. This can be contributed by the electron sink effect that functioned as an “electron pool” which collect and gather the photoexcited electrons of ZnO nanopillars that will subsequently further promote the efficient electron-hole separation. It is also observed in Figure 5.17 that the violet emission for all Ag/ZnO heterostructures are totally diminished if compared to that of pure ZnO nanopillars (similar with the previous PL result). This can be associated that little photoexcited electrons are tunnelled towards Ag nanoparticles and rendered the diminishing of violet emissions.

However, as the concentration of $AgNO_3$ salt was further increased to 2 mM and 5 mM, the red- and superposition of green and yellow emissions are enhanced in comparison to that of Ag/ZnO_1 mM. As evident in FESEM, the size of Ag nanoparticles are getting larger at higher concentration and this is expected that the effect of SPR is greatly reduced with respect to the size increment of Ag nanoparticles (Lerme, 2011; Mogensen & Kneipp, 2014). Therefore, these larger size of Ag nanoparticles generate less electric field which results in the recombination of the electron/hole pairs and the intensity of PL is enhanced. In addition, most of the photoexcited electrons can be trapped into deep level of ZnO defects which can render the superposition of green and yellow emission. Eventually, these photoexcited electrons in the deep levels also have potential to be transferred as well to Ag nanoparticles since the defect energy level in ZnO nanopillars is proved to be higher than the Fermi energy level of Ag (Lu et al., 2008). This explains the inconsistent PL intensity of green and yellow emission as depicted in Figure 5.17 for sample Ag/ZnO with concentration of 1 mM, 2 mM and 5 mM. Thus, facile charge separation remains take place but it is still subjected to the contribution by SPR effect and the electron migration from ZnO to Ag; which this charge separation can be fine-tuned by manipulating the concentration of $AgNO_3$ salt.

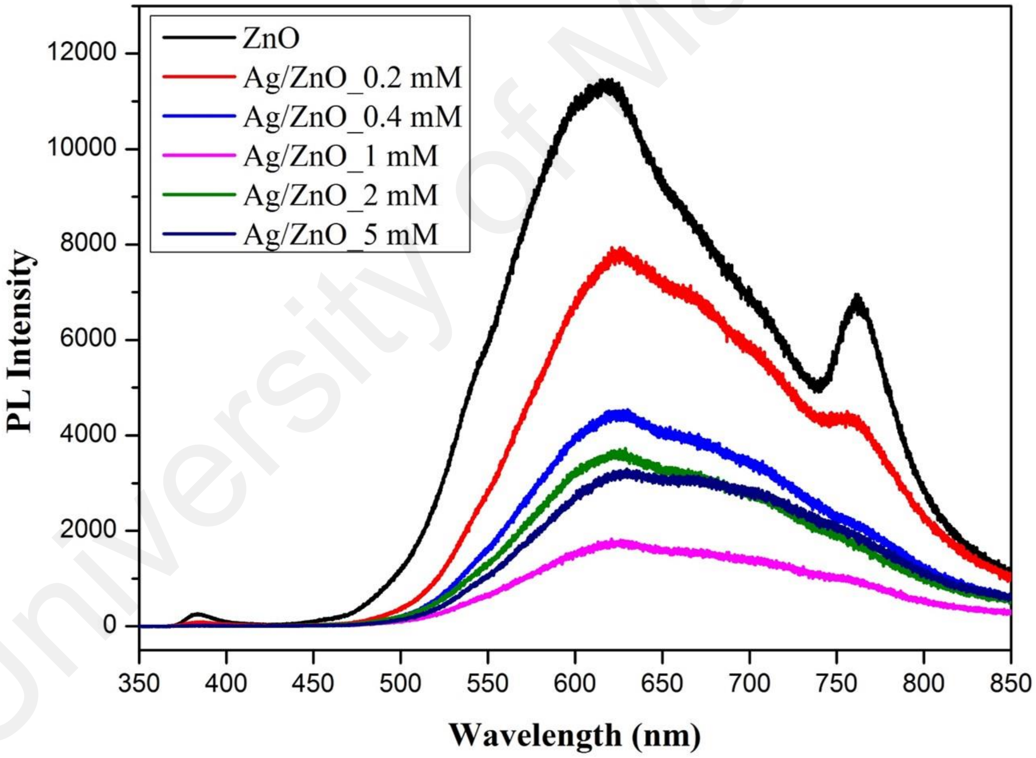

Figure 5.17: Photoluminescence spectra of ZnO nanopillars and Ag nanoparticles sensitized ZnO nanopillars at different $AgNO_3$ salt concentration

5.3.7 Growth Mechanism

The growth mechanism of ZnO nanopillars and Ag/ZnO heterostructures on Zn foil can be referred in Section 5.2.7. The growth mechanism of sensitization of Ag nanoparticles on ZnO nanopillars with different $AgNO_3$ salt concentration is almost similar to the one with different Ag^+ ions reduction time. Hence, their mechanism also can be referred in the same section. With the increment of $AgNO_3$ salt concentration, the size of Ag nanoparticles are increased and agglomerated to each other as shown in FESEM. Surprisingly, an irregular shape of ZnO tiny branches are secondarily grown on the upper half of primary ZnO nanopillars with bigger particle size of Ag nanoparticles are randomly deposited on them at concentration of 2 mM. When the concentration of $AgNO_3$ salt is increased up to 5 mM, an irregular shape of ZnO branches were getting larger with the integration of increment on the diameter of Ag nanoparticles makes those morphologies can be visualized as flower-like structures. This probably due to excessive Ag^+ ions and electrons that trigger the secondary growth to be realized.

Lastly, the strategy to synthesize Ag nanoparticles sensitized ZnO nanopillars heterostructures via two optimized parameters is successful and gives a lot of advantages which is: (1) facile synthesis due to easy sample preparation, low synthesis temperature and save the time-consuming; (2) low cost synthesis where only consume DI water, Zn foil and $AgNO_3$ precursor with very low concentration; (3) environmental-friendly route where the final waste of synthesis merely water and mild nitric acid produced; (4) three in one role of Zn foil which serves as a substrate, zinc source to grow ZnO nanopillars and as reducing agent to reduce Ag^+ ions by generating electron.

5.4 Summary

The structural- and optical-properties as well as growth mechanism of Ag nanoparticles sensitized ZnO nanopillars with different Ag^+ ions reduction time and $AgNO_3$ salt concentration are explained comprehensively. Upon this, their performance in PEC water splitting application will be discussed in Chapter 6.

CHAPTER 6: PHOTOELECTROCHEMICAL WATER SPLITTING BY USING ARGENTUM NANOPARTICLES SENSITIZED ZINC OXIDE NANOPILLARS PHOTOELECTRODE

6.1 Introduction

In this chapter, the performance of Ag sensitized ZnO photoelectrode in photoelectrochemical water splitting application through the analysis of LSV, photoconversion efficiency, Nyquist plot and Mott-Schottky plot will be discussed in detailed. The full procedure of PEC experiment can be referred in Chapter 3.4.2.

6.2 PEC Water Splitting of Ag/ZnO via Reduction Period of Ag^+ Ions

The PEC behaviour of Ag sensitized ZnO photoelectrode that fabricated through hydrothermal method at 50 °C in 1 mM $AgNO_3$ concentration with varied Ag^+ ions reduction period will be demonstrated and described one by one in the following section.

6.2.1 Linear Sweep Voltammetry Analysis

In order to realize the PEC performance via water splitting process, three-electrode system was setup, in which Ag sensitized ZnO photoelectrodes were used as working electrode (WE), platinum (Pt) rod and silver/silver chloride (Ag/AgCl) were respectively functioned as counter electrode (CE) and reference electrode (RE). Prior to the analysis of LSV, it is better to explain the behaviour of n-type semiconductor in LSV pattern for easing the understanding. Figure 6.1 shows the J-V curve of ZnO nanopillars, whereby there is three divided regions at the voltage range of -1.5 V to 0.5 V. There is no current produced at Region II (this region is known as flat band potential, E_{fb}), since there is no electric field to separate the generated charge carriers. At Region I, an accumulation layer forms and electrode acts as cathode. Hence, electrode is referred as dark cathode under this condition. Meanwhile, depletion layer exists at Region III and photocurrent density,

J_{ph} can be observed due to energy provided by the radiation. Thus, it can be shown that n-type semiconductors are dark cathode and photoanode (Bott, 1998).

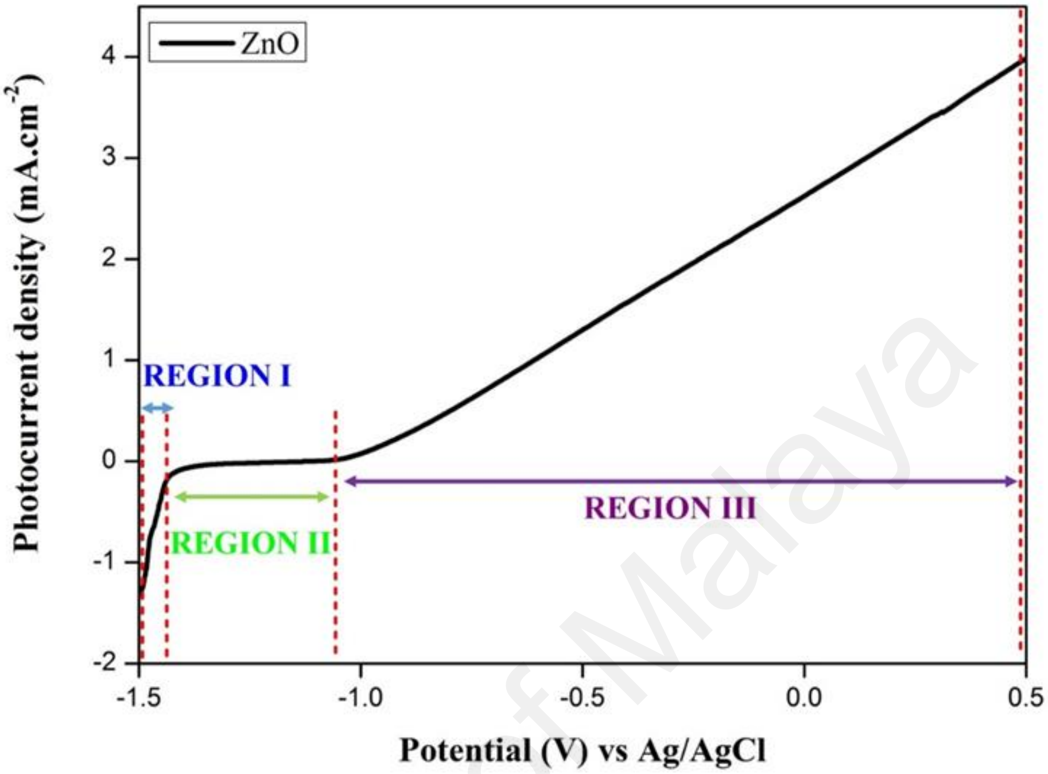

Figure 6.1: Behaviour of n-type semiconductor electrode via LSV (the LSV result obtained from this work)

Another important concept in this discussion is the Fermi level, which is defined as energy level where the probability to be occupied by an electron is half. Redox potential of semiconductor is determined by the Fermi level. If the redox potential of the solution and the Fermi level do not lie at the same energy, the movement of charges are required in order to achieve equilibrium. By changing the applied potential, the magnitude and direction of semiconductor band edges will change. However, the energy of band edges is not influenced with varied applied potential (Bard & Faulkner, 1980; Bott, 1998). Figure 6.2 depicts the changes on the band edges towards the varied applied potential for n-type semiconductor electrode. At a certain potential, the Fermi energy lies at the same energy with the solution redox potential as shown in Figure 6.2(b). Thus, there is no net charge transfer and band bending does not occur in this condition. Therefore, this potential can be referred as flat band potential, E_{fb} (as shown in Region II in Figure 6.1).

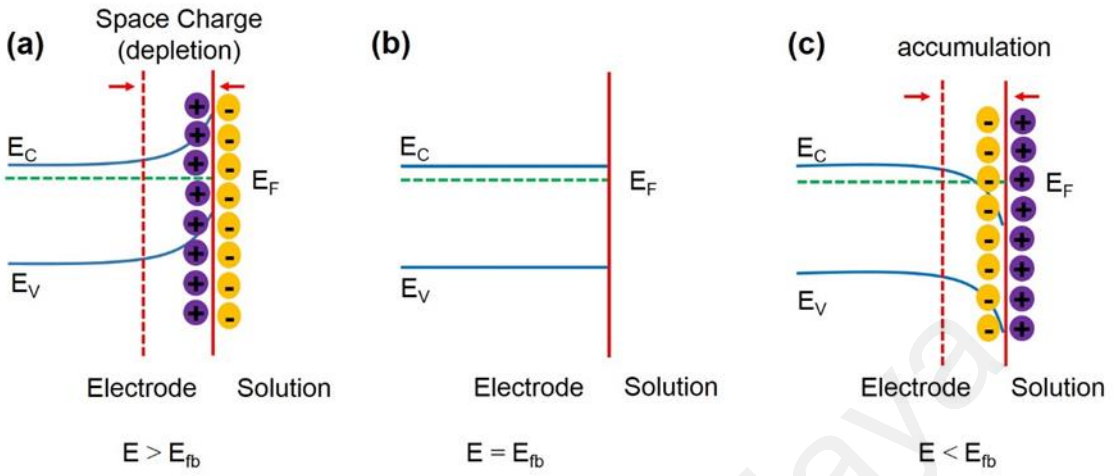

Figure 6.2: Influence of varying applied potential on the band edges for n-type semiconductor electrode at (a) $E > E_{fb}$, (b) $E = E_{fb}$ and (c) $E < E_{fb}$ (Re-illustrated from Bott, 1998)

At open circuit, the Fermi level is higher than the solution redox potential, hence electrons will be transferred from the electrode into the solution to achieve equilibrium. Therefore, positive charge generated in the interior semiconductor and space charge or depletion layer forms at potential higher than E_{fb} (Region III in Figure 6.1). This is reflected in an upward bending of the band edges as illustrated in Figure 6.2(a). At potential lower than E_{fb} (Region I in Figure 6.1), majority of the electrons will move from the solution into the electrode and subsequently cause downward band bending of band edges and can be referred as accumulation layer (Bard & Faulkner, 1980; Bott, 1998) as shown in Figure 6.2(c). This explanation is applied on the p-type semiconductor electrode as well, but in the opposite way.

The charge transfer ability depends on whether there is an accumulation or a depletion layer. The behaviour of the semiconductor electrode is similar to that of metallic electrode if an accumulation layer is formed, since an excess of majority of charge carriers are available for charge transfer. In contrast, if a depletion layer is generated, then few charge carriers are available for charger transfer, thus the electron transfer reactions occur slowly. However, if the electrode is irradiated with sufficient energy, electrons can be promoted to the CB. If the excitation process occurs in the interior semiconductor, the recombination of electron and hole are highly happened. But, if it occurs in the depletion region, the electric field in this region will separate the charge efficiently. Hence the band edges curve upwards, hole moves towards the interface, and the electron moves to the semiconductor interior. Then, n-type semiconductor can act as a photoanode to generate the photocurrent (Bard & Faulkner, 1980; Bott, 1998).

In LSV analysis, the two most important metrics of J_{ph} are the plateau current and the onset potential, E_{onset}. Basically, the plateau current depends on the photogenerated holes and electrons that reach the semiconductor/electrolyte interface and subsequently react with water to generate O_2 and H_2 gases. The higher plateau current means higher J_{ph} production in which suggests the more efficient of harvesting the solar light and converting it to electricity (Chen et al., 2014).

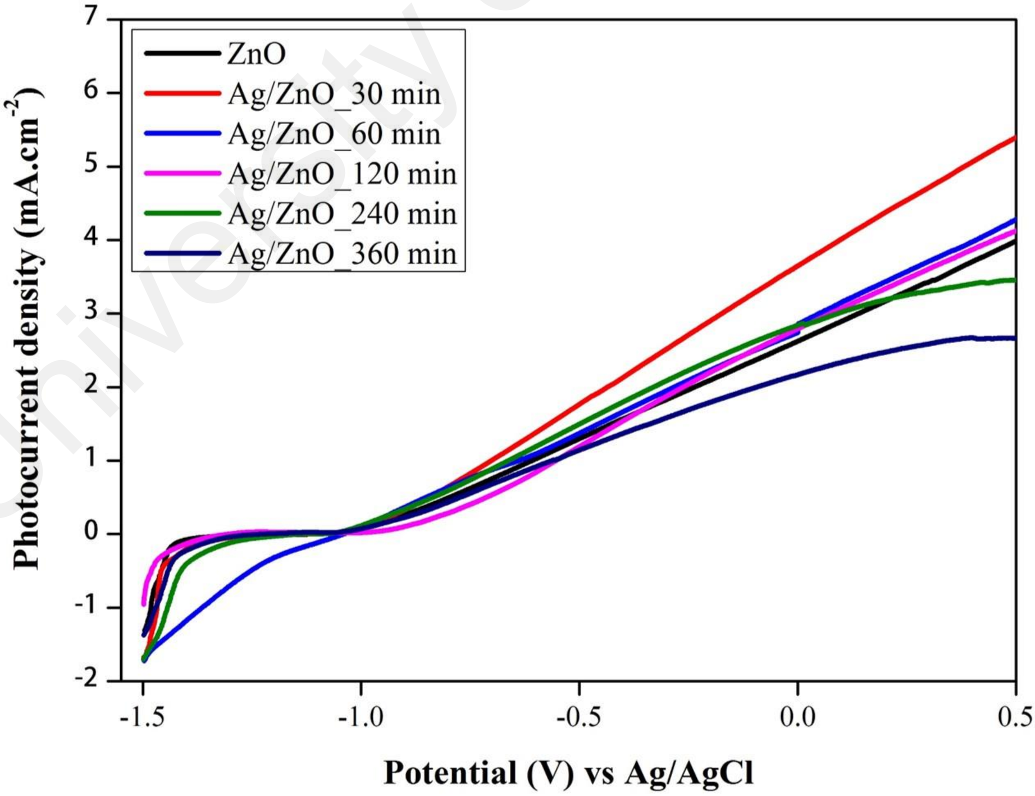

Figure 6.3: J-V curve of ZnO nanopillars and Ag sensitized ZnO photoanodes with different reduction period of Ag^+ ions

Figure 6.3 depicts the photocurrent density, J_{ph} against potential, E curves of ZnO nanopillars and Ag sensitized ZnO photoanodes. The photoinduced anodic currents that demonstrated in Figure 6.3 are resulted from the oxidation of water involving the photogeneration of holes. The photoinduced anodic current also give a quick information that all photoelectrodes are n-type semiconductor and normally n-type semiconductor is so-called photoanode. So, the word "photoanode" will be used throughout the discussion.

Under solar AM1.5G light illumination, Ag nanoparticles sensitized ZnO nanopillars photoanode at reduction period of 30 min exhibits the highest J_{ph} of ~5.4 mA.cm^{-2} at applied potential of 0.5 V vs Ag/AgCl, which is almost 1.4 times higher than that of pristine ZnO nanopillars photoanode which generates ~4.0 mA.cm^{-2} at applied potential of 0.5 V vs Ag/AgCl. The improvement of J_{ph} can be attributed to an increment of photogenerated electrons/holes production and their effective separation, facilitated by the excellent absorption of visible light (Upadhyay et al., 2014) as proven by PL and DRS analysis. Ag/ZnO_30 min photoanode has the lowest PL intensity and this shows that Ag nanoparticles act as an electron sinks that suppress the recombination rate of electron/hole pairs as well as prolong their lifetime. This can facilitate the improvement of PEC performance. Besides, Ag/ZnO_30 min photoanode also has the highest visible light absorption which could enhance the generation of J_{ph}. The comparison of J_{ph} at 0.5 V vs Ag/AgCl for all photoanodes are compiled in Table 6.1.

In addition, there is no saturation J_{ph} observed in ZnO nanopillars and Ag sensitized ZnO photoanodes except for the Ag/ZnO_240 min and Ag/ZnO_360 min. Saturation J_{ph} is due to the inefficient charge separation and collection (Sun et al., 2014; Li et al., 2014). If compared to ZnO nanopillars, both of these photoanodes generated lower J_{ph} as well. The lower J_{ph} generation may due to the agglomeration of bigger particle size of Ag nanoparticles (as viewed in FESEM results in Chapter 5.2.1) which acted as recombination center for photogenerated electron/hole pairs and finally resulted in the inefficient charge separation and collection (Wu et al., 2014). The incorporation of Ag nanoparticles onto ZnO nanopillars can create the electronic surface state at the interface which acts as trapping state to trap electrons or holes to prevent the recombination of the carrier charges. However, the energy of these surface states depend on the nature of noble metal, size of noble metal particle and properties of semiconductor (Zare et al., 2016). When the size of Ag nanoparticles is increased with respect to the extended reduction period, the depth of energy level of surface states also increased. Therefore, the electric interaction with CB becomes weak, the trapping life time of electron or hole become shorter. Consequently, charge carrier are easily to recombine and results in the lower production of J_{ph}.

Table 6.1: LSV characteristic of ZnO nanopillars and Ag sensitized ZnO at different reduction period of Ag^+ ions

Photoanode	Photocurrent density, J_{ph} (mA.cm^{-2}) at 0.5 V vs Ag/AgCl (1.1 V vs RHE) (± 0.2 mA.cm^{-2})	Onset potential, E_{onset} (V) vs Ag/AgCl (± 0.05 V)	Short circuit current density, J_{sc} (mA.cm^{-2}) (± 0.2 mA.cm^{-2})
ZnO nanopillars	4.0	-1.03	2.6
Ag/ZnO_30 min	5.4	-1.07	3.6
Ag/ZnO_60 min	4.3	-1.06	2.7
Ag/ZnO_120 min	4.1	-0.98	2.8
Ag/ZnO_240 min	3.4	-1.06	3.6
Ag/ZnO_360 min	2.6	-1.03	2.1

As mentioned before, the other important metric in J_{ph} is E_{onset}. The E_{onset} values for all photoanodes are shown in Table 6.1. The negatively shifting of E_{onset} demonstrates that the photoanodes have the outstanding electron/hole pair's separation and would benefit the solar decomposition of water at smaller voltage (Hsu et al., 2015; Yang et al., 2017). Ag/ZnO_30 min photoanode has the cathodic E_{onset} where this photoanode has produced the highest J_{ph}. Once the E_{onset} is determined, the overpotential must be considered. The overpotential can be occurred mainly due to the slow kinetic of water oxidation and results in the accumulation of electrons and holes on the surface (Chen et al., 2014). Since the overpotential is related to the flat band potential, E_{fb}, the analysis of the overpotential will be carried out after the determination of E_{fb} value and will be discussed in MS plot section.

Additionally, short circuit current, J_{sc} can be obtained from the J-V curve as well, whereby can be defined as the one at zero potential versus reference electrode (Wei et al., 2013). The value of J_{sc} for all photoelectrodes are shown in Table 6.1, in which Ag/ZnO_30 min has J_{sc} of 3.6 mA.cm^{-2} at 0 V vs Ag/AgCl. Ag/ZnO_240 min photoelectrode also has J_{sc} of 3.6 mA.cm^{-2} at 0 V vs Ag/AgCl, but it produced low J_{ph} of ~3.4 mA.cm^{-2} at an applied potential 0.5 V vs Ag/AgCl. Regarding to FESEM result, Ag/ZnO_240 min photoelectrode possessed longer and larger hyperbranched of secondary ZnO nanopillars which these morphologies facilitate the absorption of light and further enhanced the J_{ph} rate. However, due to the agglomeration of bigger size of Ag nanoparticles the separation of electron/hole pairs become less effective which then causes the J_{ph} decay.

The reduction period of Ag^+ ions was reduced to 15 min in order to investigate the trend of J_{ph} and the J-V curve of Ag/ZnO_15 min photoanode is compared with the J-V curve of Ag/ZnO_30 min photoanode as depicted in Figure 6.4. As revealed in the LSV measurement, when the reduction period of Ag^+ ions was reduced to 15 min the J_{ph} is decreased to ~4.7 mA.cm^{-2} at an applied voltage 0.5 V vs Ag/AgCl.

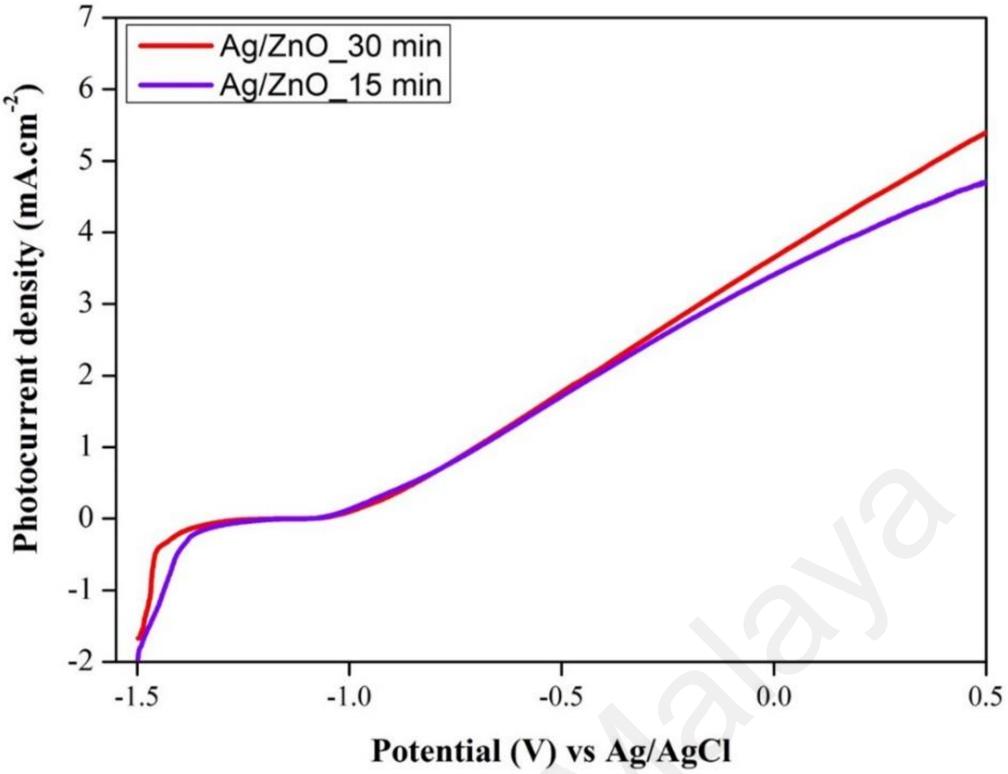

Figure 6.4: Comparison of J-V curve of Ag/ZnO_30 min and Ag/ZnO_15 min photoanodes

6.2.2 Photoconversion Efficiency Analysis

Photoconversion efficiency is the efficiency evaluation of light energy to chemical energy conversion in which it is calculated from J-V curve through Equation 3.5 that can be referred in Chapter 3.4.4. The photoconversion efficiencies for all as-synthesized photoanodes are demonstrated in Figure 6.5. The potential was measured against an Ag/AgCl reference and was converted to RHE potential by using Equation 3.6. The pristine ZnO nanopillars exhibits the optimal conversion efficiency of ~1.70 % at 0.45 V vs RHE. Significantly, Ag/ZnO_30 min photoanode achieves the highest photoconversion efficiency of ~2.40 % at 0.45 V vs RHE in which 140 % higher if compared to the pristine ZnO nanopillars. Maximum photoconversion efficiency for all as-prepared photoanodes are compiled in Table 6.2.

The sensitization of Ag nanoparticles on ZnO nanopillars has successfully improved the photoconversion efficiency except for Ag/ZnO_360 min photoanode. This may due to the agglomeration and excessive growth of Ag nanoparticles on the surface of ZnO nanopillars at 360 min reduction period that finally causes the inefficient separation of electrons/holes pairs and faster recombination rate. Though Ag/ZnO_240 min photoelectrode produced less J_{ph} rate than ZnO nanopillars, but it achieves maximum photoconversion efficiency of ~1.90 % at 0.38 V vs RHE, which is higher if compared to ZnO nanopillars, Ag/ZnO_60 min and Ag/ZnO_120 min. This may due to the longer and larger secondary branched ZnO nanopillars that provide larger surface area to absorb solar light at visible range.

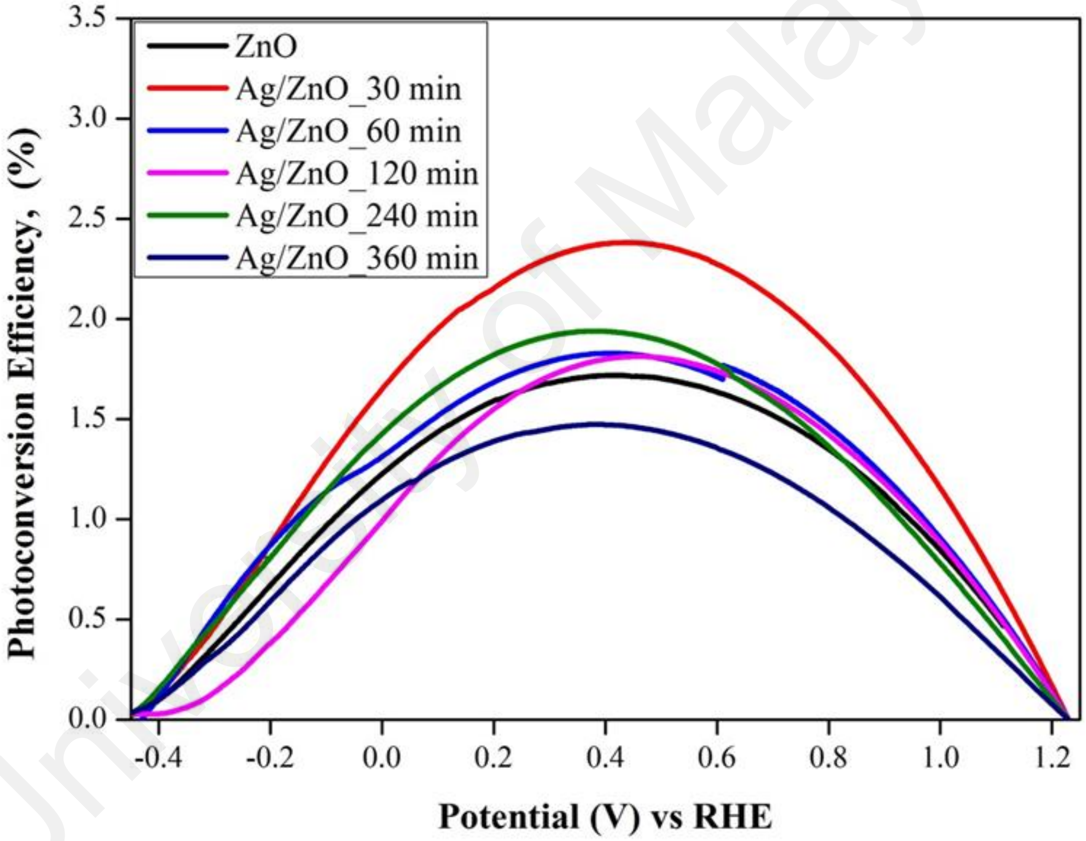

Figure 6.5: Photoconversion efficiency of Ag sensitized ZnO photoanodes at different reduction period of Ag$^+$ ions

Table 6.2: Compilation of maximum photoconversion efficiency of Ag sensitized ZnO at varied reduction period of Ag^+ ions

Photoanode	Maximum photoconversion efficiency, η (%) (± 0.04 %)
ZnO nanopillars	1.70 at 0.45 V vs RHE
Ag/ZnO_30 min	2.40 at 0.45 V vs RHE
Ag/ZnO_60 min	1.80 at 0.38 V vs RHE
Ag/ZnO_120 min	1.81 at 0.45 V vs RHE
Ag/ZnO_240 min	1.90 at 0.38 V vs RHE
Ag/ZnO_360 min	1.47 at 0.38 V vs RHE

The previous studies about photoconversion efficiency for ZnO sensitized with various materials are summarized in Table 6.3. This summary shows that the as-obtained photoconversion efficiency in current work is fallen within the range of efficiency that reported by other researchers. Making a comparison for all as-reported efficiency with current work is lack of confidence level, since the parameters that influence the PEC performance such as molarity and type of electrolyte, substrate used, morphology of photoelectrode, and type of materials that incorporated with ZnO are quite different. Nevertheless, the information in Table 6.3 can serve as reference or guideline in current study.

Table 6.3: Summary of previous reported photoconversion efficiency

Sample	Substrate	Reference and Counter electrode	Type and molarity of electrolyte	Maximum photoconversion efficiency (%)	Reference
Au/Branched ZnO	FTO	Ag/AgCl Pt coil	0.5 M Na_2SO_4	0.52 at 0.8 V_{RHE}	Zhang et al., 2014
ZnO/ZnS/Au	FTO	Ag/AgCl Pt coil	0.5 M Na_2SO_4	0.21 at 0.928 V_{RHE}	Liu et al., 2015
Ag/ZnO	PET	Ag/AgCl Pt foil	0.5 M Na_2SO_4	0.81 at 0.29 $V_{Ag/AgCl}$	Wei et al., 2012
Si/ZnO	Si wafer	SCE Pt sheet	0.5 M Na_2SO_4	0.035 at 0.54 V_{SCE}	Ji et al., 2013
H:ZnO/CdS/C	ITO	Hg_2Cl_2/Hg Pt grid	0.5 M Na_2SO_4 + 0.25 M Na_2S + 0.35 M Na_2SO_3	3.85 at -0.67 V_{SCE}	Vuong et al., 2015
Au/ZnO	Zn foil	Ag/AgCl Pt foil	0.1 M Na_2SO_4	0.48 at 1.05 V_{RHE}	Wu et al., 2014
N/ZnO	ITO	Ag/AgCl Pt coil	0.5 M $NaClO_4$	0.15 at 0.5 $V_{Ag/AgCl}$	Yang et al., 2009
PbS/ZnO	FTO	Ag/AgCl Pt plate	0.1 M Na_2SO_4	0.09 at 0.85 V_{RHE}	Li et al., 2016
ZnO/C/Ag	FTO	Ag/AgCl Pt foil	0.5 M Na_2SO_4	3.90 at 0.22 $V_{Ag/AgCl}$	Wei et al., 2013
ZnO/N/CdTe	FTO	Ag/AgCl Pt plate	0.5 M Na_2SO_4	0.90 at 0.5 $V_{Ag/AgCl}$	Chen et al., 2014
Ag/ZnO	Zn foil	Ag/AgCl Pt rod	0.1 M Na_2SO_4	2.40 at 0.45 V_{RHE}	This work

6.2.3 Nyquist Plot Analysis

EIS is a powerful technique to study the electrical behaviour of the semiconductor/electrolyte interface via the Nyquist plot, whereby the Nyquist plot for all as-synthesized photoanodes is demonstrated in Figure 6.6. The analysis of Nyquist plot spectrum provides the information of the charge transport process that occurs at the interface of semiconductor and electrolyte, which is the type of charge carriers that involves in this process is electronic charge (consisted of electrons and holes).

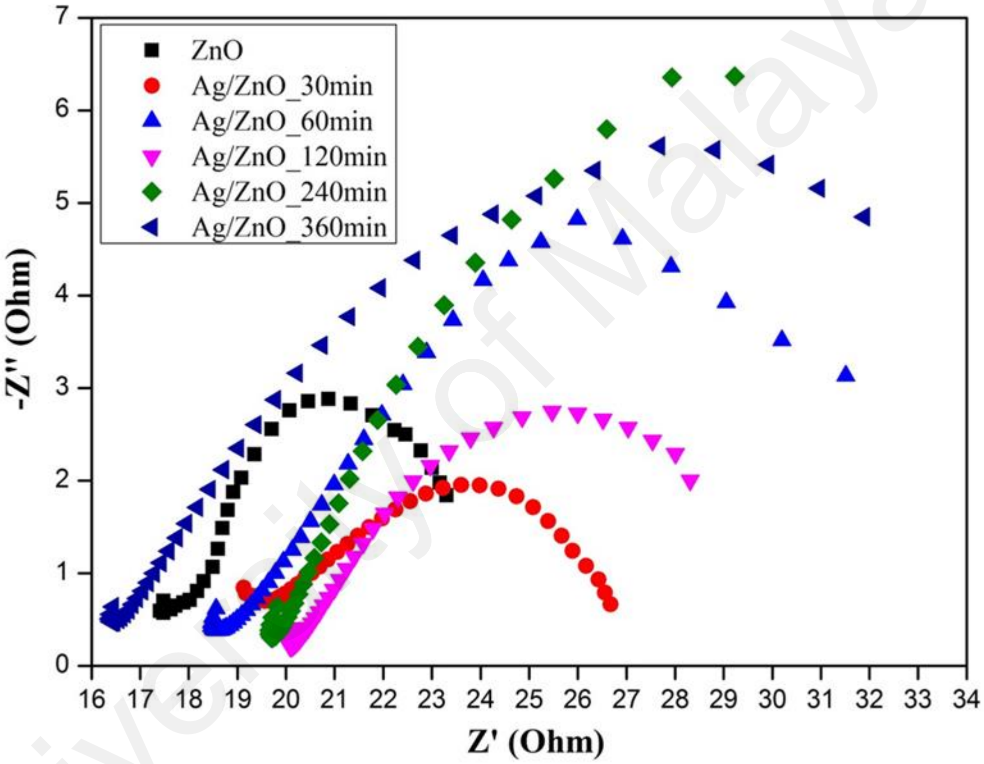

Figure 6.6: Nyquist plot of Ag sensitized ZnO photoanodes with different Ag^+ ions reduction period

The arc diameter of the semicircle can be associated to the charge transfer resistance, R_{CT} at the semiconductor/electrolyte interface. The electrolyte resistance can be related to the high-frequency range of semicircle and semicircle in the mid-frequency regions correspond to the charge transfer process. The smaller the impedance-related arc of semicircle in the mid-frequency, the charge transfer between the photoelectrode and electrolyte will be faster. On the other hand, larger arc diameter indicates the large charge transfer resistance (Sun et al., 2014; Wang et al., 2015).

As depicted in Figure 6.6, Ag/ZnO_30 min photoanode exhibits the smallest capacitive arc diameter suggesting that this photoanode possesses the fastest charge transfer at the semiconductor/electrolyte interface. The Ag nanoparticles enhance the electron mobility by suppressing the recombination of photogenerated electron/hole pairs in the Ag/ZnO heterostructures, thus enhance the J_{ph} rate. Hence, reduced charge transfer resistance is another key factor for improving the PEC performance (Wu et al., 2014).

6.2.4 Mott-Schottky Plot Analysis

The MS plot can also be generated from the EIS measurement, whereby the MS plot of Ag nanoparticles sensitized ZnO nanopillars photoanodes are depicted in Figure 6.7. All the photoanodes show positive slope which indicates that all the photoanodes have a characteristic of n-type semiconductor material. This directly shows that the space charge is populated with holes. In contrast, if the space charge is populated with electrons, then the slope will be negative resulting an indication that the semiconductor is a p-type materials. The intrinsic electronic properties of Ag nanoparticles sensitized ZnO nanopillars photoanodes such as the determination of flat band potential, E_{fb} as well as charge carrier density, N_D can be extracted from the MS plot. The value of E_{fb} can be determined by extrapolating the x-axis in MS plot, while N_D can be obtained from the slope of MS plot via the Equation of 3.17 (refer to Chapter 3.4.6). The obtained E_{fb} and $\boldsymbol{N_D}$ for all photoanodes are summarized in Table 6.4.

According to Bott (1998), E_{fb} can be determined by measuring the photopotential as a function of radiation intensity, the onset of the J_{ph}, or the capacitance of the space charge region through MS plot analysis. However, current work is adopting the third method (the capacitance of the space charge region through MS plot analysis). For the second method, although the onset of the J_{ph} might be simplistically considered to be the flat band potential, actually it is the potential at which the dark current and J_{ph} are equal (Bott, 1998). From the N_D calculation, Ag/ZnO_30 min photoelectrode has the highest N_D estimation which is almost 3.1 times higher than ZnO nanopillars photoanode. The sensitization of Ag nanoparticles is successfully enhance the donor density, whereby finally enhance the electrical conductivity as well as the charge transport (Kang et al., 2013). However, the N_D estimation is reduced when the reduction period was prolonged. This may attributed to the insufficient charge separation due to the agglomeration of bigger particle size of Ag nanoparticles that acted as recombination site (Kang et al., 2013).

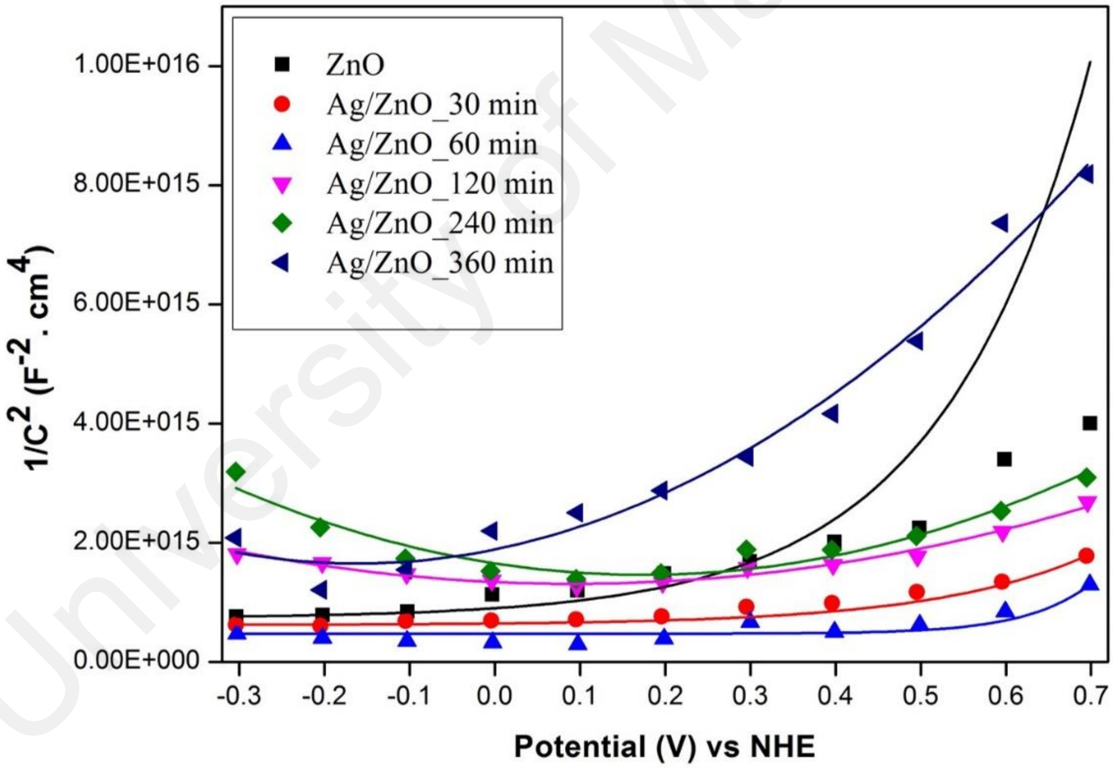

Figure 6.7: Mott-Schottky plot of Ag sensitized ZnO photoanodes with varied Ag$^+$ ions reduction time

Table 6.4: Intrinsic electronic values of Ag sensitized ZnO photoanodes with varied Ag^+ ions reduction time

Photoanode	Charge carrier density, N_D (cm^{-3})	Flat band potential, E_{fb} (V)		Onset potential, E_{onset} (V) vs Ag/AgCl (± 0.05 V)
		vs NHE (± 0.02 V)	vs Ag/AgCl (± 0.02 V)	
ZnO nanopillars	5.643×10^{15}	-0.40	-0.60	-1.03
Ag/ZnO_30 min	1.763×10^{16}	-0.56	-0.76	-1.07
Ag/ZnO_60 min	1.749×10^{16}	-0.44	-0.64	-1.06
Ag/ZnO_120 min	7.452×10^{15}	-0.43	-0.63	-0.98
Ag/ZnO_240 min	5.455×10^{15}	-0.40	-0.60	-1.06
Ag/ZnO_360 min	2.610×10^{15}	-0.38	-0.38	-1.03

In addition, Ag/ZnO_30 min photoanode also exhibits the most cathodic of E_{fb} value. The negatively shifting of E_{fb} value to the cathodic range indicates that the photoanode has the better ability to facilitate the charge separation in the heterostructures and increase the surface band bending (Kang et al., 2013; Upadhyay et al., 2014; Hsu et al., 2015). As a results, the J_{ph} density is enhanced. Thus, higher N_D value and further negative shift of E_{fb} are another key factor to improve the PEC performance.

As mentioned before, the E_{onset} is correspond to the E_{fb} and the analysis of overpotential can be carried out after the determination of E_{fb} value. By comparing the value of E_{onset} and E_{fb} against Ag/AgCl reference in Table 6.4, it is proven that all the photoanodes have more cathodic E_{onset} values if compared to that of E_{fb} values. Thus, this suggest that no overpotential occurred at negative potential range and faster charge transfer happened in this range (see Figure 6.3) which then facilitate the separation of photogenerated electron/hole pairs. Hence, J_{ph} is generated successfully.

6.3 PEC Water Splitting of Ag/ZnO via $AgNO_3$ Concentration

The PEC characteristic of Ag nanoparticles sensitized ZnO nanopillars photoanodes that synthesized via two steps hydrothermal approach at 30 min reduction period of Ag^+ ions with varied $AgNO_3$ concentration will be discussed in the following section.

6.3.1 Linear Sweep Voltammetry Analysis

The J-V curve of ZnO nanopillars and Ag/ZnO photoanodes that reduced at different $AgNO_3$ concentration is shown in Figure 6.8. Upon illumination of solar light, Ag sensitized ZnO nanopillars with $AgNO_3$ concentration of 1 mM exhibits the highest J_{ph} of ~5.4 mA.cm^{-2} at an applied potential of 0.5 V vs Ag/AgCl which is almost 1.4 times higher if compared to that of pure ZnO nanopillars that generates ~4.0 mA.cm^{-2} at an applied potential of 0.5 V vs Ag/AgCl. The enhancement of J_{ph} can be associated to extra number of photogenerated electrons/holes production that play the role as free carriers as well as their effective separation, which is facilitated by the enhanced absorption of visible light (Upadhyay et al., 2014) as proven by PL and DRS analysis. Ag/ZnO_1 mM photoanode has the lowest PL intensity and this shows that Ag nanoparticles act as an electron sinks which then suppress the recombination rate of electron/hole pairs as well as prolong their lifetime. Besides, Ag/ZnO_1 mM photoanode also has the highest visible light absorption which could enhance the generation of J_{ph}. The comparison of J_{ph} at 0.5 V vs Ag/AgCl for all photoanodes are compiled in Table 6.5.

According to Figure 6.8, saturation of J_{ph} which is due to the inefficient charge separation and collection (Sun et al., 2014; Li et al., 2014) cannot be observed in ZnO nanopillars and Ag sensitized ZnO photoanodes except for the Ag/ZnO_2 mM and Ag/ZnO_5 mM. If compared to ZnO nanopillars, both of these photoanodes generated lower J_{ph} as well. The lower J_{ph} generation may due to the aggregation of interparticles of Ag nanoparticles (as viewed in FESEM results in Chapter 5.2.1) which acted as recombination center for photogenerated electron/hole pairs. In addition, this also could be due to an irregular shape of secondary ZnO nanopillars formation as observed in FESEM analysis. As a results, charge separation and collection are occurred inefficiently (Wu et al., 2014).

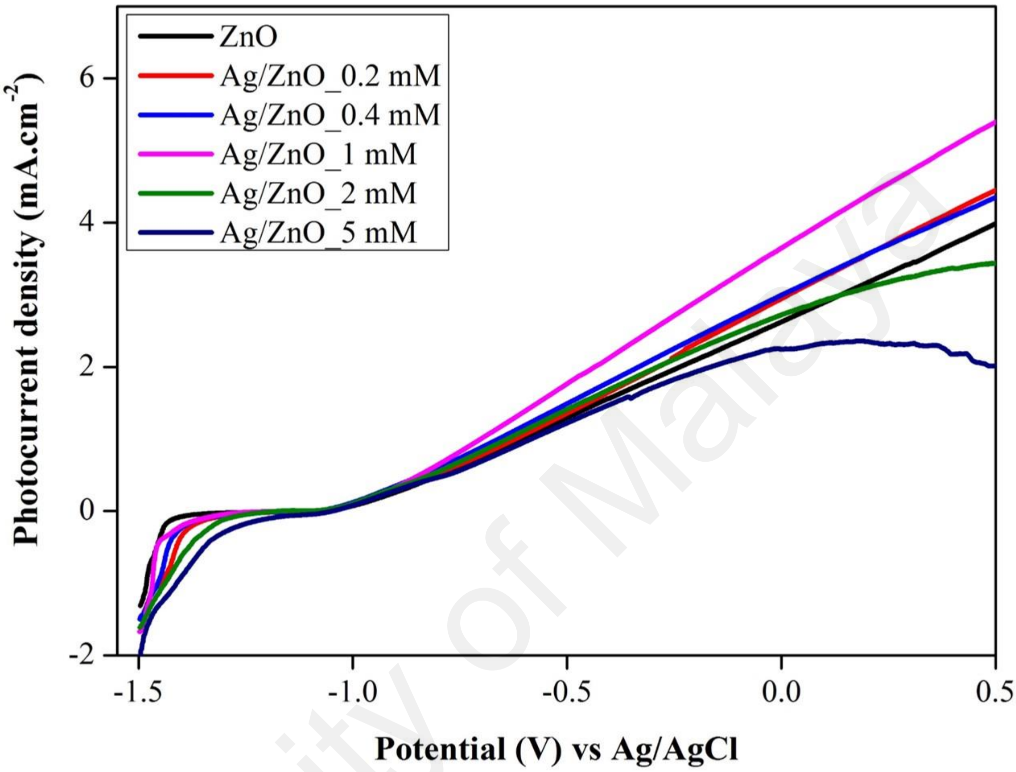

Figure 6.8: J-V curve of ZnO nanopillars and Ag sensitized ZnO photoanodes with different $AgNO_3$ salt concentration

The E_{onset} value for all photoanodes are demonstrated in Figure 6.4, whereby their values are shifted to the negative potentials and this shows that all photoanodes have the outstanding electron/hole pair's separation. This would benefit the solar decomposition of water at smaller voltage (Hsu et al., 2015; Yang et al., 2017). In comparison, Ag/ZnO_1 mM photoanode has the most cathodic E_{onset}, which supports the deduction that this photoanode produced the highest value of J_{ph}. Once the E_{onset} is determined, the overpotential must be considered. The overpotential can be occurred mainly due to the slow kinetic of water oxidation and results in the accumulation of electrons and holes on the surface (Chen et al., 2014). The overpotential analysis for the photoanode that reduced at different concentration of $AgNO_3$ will be made after the determination of E_{fb} value and will be discussed in MS plot section. Besides that, J_{sc} values for photoanodes of different $AgNO_3$ concentration can be found in Table 6.5.

Table 6.5: LSV characteristic of ZnO nanopillars and Ag sensitized ZnO at different $AgNO_3$ salt concentration

Photoanode	Photocurrent density, J_{ph} (mA.cm^{-2}) at 0.5 V vs Ag/AgCl (1.1 V vs RHE) (± 0.2 V)	Onset potential, E_{onset} (V) vs Ag/AgCl (± 0.05 V)	Short circuit current density, J_{sc} (mA.cm^{-2}) (± 0.2 V)
ZnO nanopillars	4.0	-1.03	2.6
Ag/ZnO_0.2 mM	4.4	-1.05	2.9
Ag/ZnO_0.4 mM	4.3	-1.04	3.0
Ag/ZnO_1 mM	5.4	-1.07	3.6
Ag/ZnO_2 mM	3.4	-1.03	2.7
Ag/ZnO_5 mM	2.0	-1.01	2.4

6.3.2 Photoconversion Efficiency Analysis

Figure 6.9 depicts the photoconversion efficiency of ZnO nanopillars and Ag nanoparticles sensitized ZnO nanopillars heterostructures that reduced at different $AgNO_3$ concentration. Photoconversion efficiency can be calculated from the J-V curve through Equation 3.5 (refer to Chapter 3.4.4). The potential was measured against an Ag/AgCl reference and was converted to RHE potential by using Equation 3.6. The pristine ZnO nanopillars exhibits the optimal photoconversion efficiency of ~1.70 % at 0.45 V vs RHE. Significantly, Ag/ZnO_1 mM photoanode achieves the highest photoconversion efficiency of ~2.40 % at 0.45 V vs RHE in which 140 % higher if compared to the pristine ZnO nanopillars. Maximum photoconversion efficiency for all as-prepared photoanodes are compiled in Table 6.6.

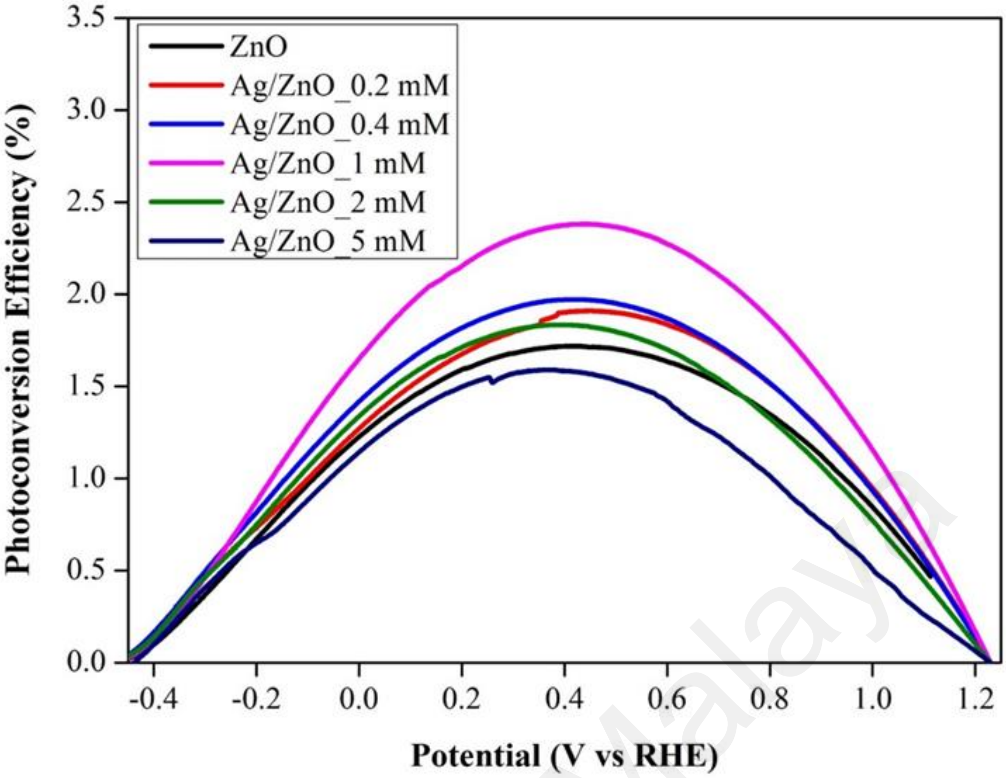

Figure 6.9: Photoconversion efficiency of ZnO nanopillars and Ag sensitized ZnO photoanodes at different concentration of $AgNO_3$ salt

Table 6.6: Compilation of maximum photoconversion efficiency of ZnO nanopillars and Ag sensitized ZnO photoanodes at different concentration of $AgNO_3$ salt

Photoanode	Maximum photoconversion efficiency, *η* (%) (± 0.04 %)
ZnO nanopillars	1.70 at 0.45 V vs RHE
Ag/ZnO_0.2 mM	1.85 at 0.45 V vs RHE
Ag/ZnO_0.4 mM	1.95 at 0.40 V vs RHE
Ag/ZnO_1 mM	2.40 at 0.45 V vs RHE
Ag/ZnO_2 mM	1.80 at 0.40 V vs RHE
Ag/ZnO_5 mM	1.60 at 0.39 V vs RHE

According to Table 6.6, all of the as-prepared photoanodes exhibit enhancement in photoconversion efficiency upon the sensitization with Ag nanoparticles except sample Ag/ZnO_5 mM that achieves only 1.60 % at 0.39 V vs RHE which is 1.06 times lower than bare ZnO nanopillars. This is due to the bigger particle size of Ag nanoparticles embedded on the surface of ZnO nanopillars as well as the irregular shape of secondary ZnO nanopillars that results in J_{ph} decay and subsequently reduce the photoconversion efficiency.

6.3.3 Nyquist Plot Analysis

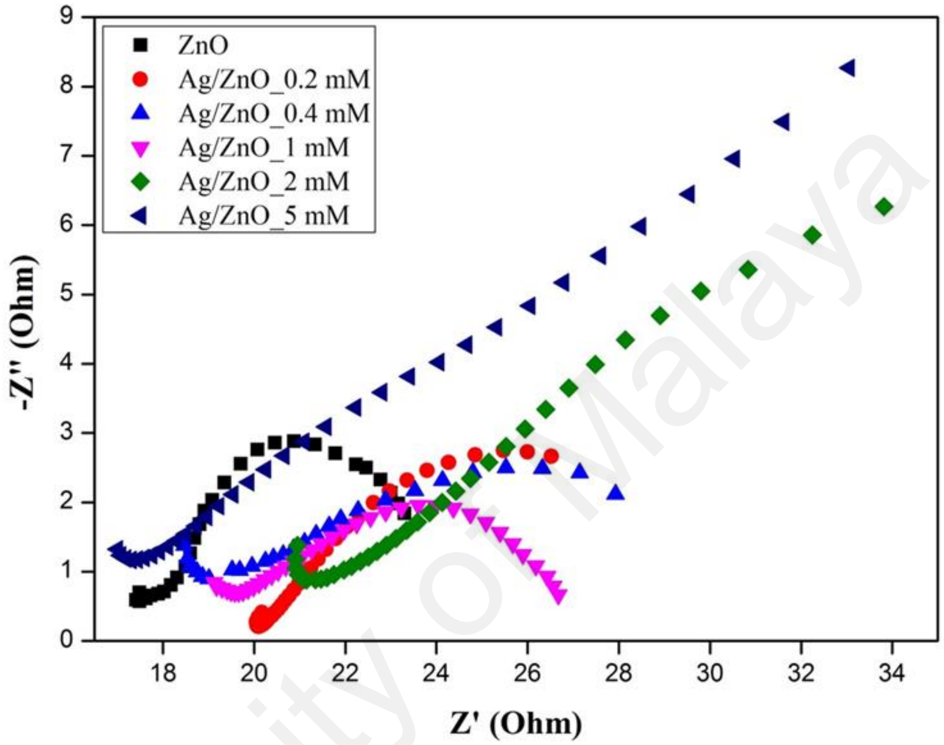

Figure 6.10: Nyquist plot of ZnO nanopillars and Ag nanoparticles sensitized ZnO nanopillars heterostructures at different $AgNO_3$ salt concentration

The analysis of Nyquist plot spectrum provides the information of the charge transport process that occurs in the semiconductor and electrolyte. The Nyquist plot for all as-prepared photoanodes that reduced at different $AgNO_3$ concentration is shown in Figure 6.10. Ag/ZnO_1 mM photoanode exhibits the smallest capacitive arc diameter suggesting that this photoanode possesses the fastest charge transfer at the semiconductor/electrolyte interface. It is hypothesized that the Ag nanoparticles has enhanced the electron mobility by suppressing the recombination of photogenerated electron/hole pairs in the Ag/ZnO heterostructures, thus enhanced the J_{ph} rate. In conjugation with this, reduction in charge transfer resistance is another key factor for improving the PEC performance (Wu et al., 2014). As the $AgNO_3$ concentration was increased up to 5 mM, a linear potion is observed which is known as Warburg resistance. This resistance is mainly due to the frequency dependence of ion diffusion that transport from electrolyte to electrode surface (Ma et al., 2015; Anitha et al., 2016).

6.3.4 Mott-Schottky Plot Analysis

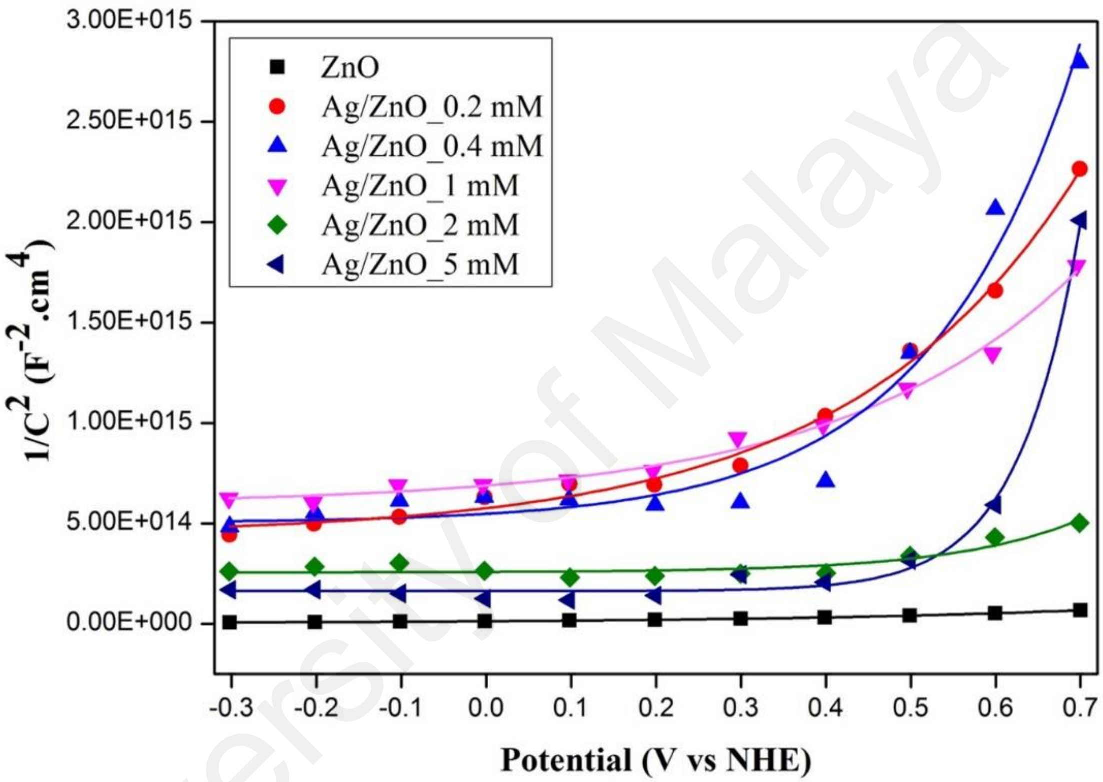

Figure 6.11: Mott-Schottky plot of ZnO nanopillars and Ag sensitized ZnO nanopillars at different $AgNO_3$ salt concentration

The MS plot of ZnO nanopillars and Ag nanoparticles sensitized ZnO nanopillars photoanodes which is generated from the EIS measurement is depicted in Figure 6.11. All photoanodes show the positive slope that observed in MS plot indicates that all as-synthesized photoanodes have a characteristic of n-type semiconductor material. The obtained E_{fb} and N_D for all photoanodes are summarized in Table 6.7.

Table 6.7: Intrinsic electronic values of Ag sensitized ZnO photoanodes with varied $AgNO_3$ salt concentration

Photoanode	**Charge carrier density, N_D (cm^{-3})**	**Flat band potential, E_{fb} (V)**		**Onset potential, E_{onset} (V) vs Ag/AgCl (± 0.05 V)**
		vs NHE (± 0.02 V)	**vs Ag/AgCl (± 0.02 V)**	
ZnO nanopillars	5.643×10^{15}	-0.40	-0.60	-1.03
Ag/ZnO_0.2 mM	2.736×10^{15}	-0.42	-0.62	-1.05
Ag/ZnO_0.4 mM	2.031×10^{15}	-0.12	-0.32	-1.04
Ag/ZnO_1 mM	1.763×10^{16}	-0.56	-0.76	-1.07
Ag/ZnO_2 mM	1.692×10^{16}	0.14	0.06	-1.03
Ag/ZnO_5 mM	1.021×10^{15}	0.56	0.36	-1.01

Upon the sensitization of Ag nanoparticles, the N_D estimation is getting increased when $AgNO_3$ concentration was increased from 0.2 mM to 1 mM as summarized in Table 6.7., with Ag/ZnO_1 mM photoanode achieves the highest N_D estimation which is almost 3.1 times higher than pristine ZnO nanopillars photoanode. The sensitization of Ag nanoparticles is successfully enhanced the donor density, whereby finally enhanced the electrical conductivity as well as the charge transport (Kang et al., 2013). However, the N_D estimation is reduced $AgNO_3$ concentration was increased from 2 mM to 5 mM. This may attributed to the insufficient charge separation due to an irregular shape of secondary ZnO nanopillars and may also attribute to the agglomeration of larger particle size of Ag nanoparticles that acted as recombination site (Kang et al., 2013) at the interface of Ag/ZnO heterostructures. In addition, Ag/ZnO_1 mM photoanode also exhibits the most cathodic of E_{fb} value. The negatively shifting of E_{fb} value to the cathodic or negative potential range indicates that the photoanode has the better ability to facilitate the charge separation in the heterostructures and increase the surface band bending (Kang et al., 2013; Upadhyay et al., 2014; Hsu et al., 2015). As a results, the J_{ph} density is enhanced.

Thus, higher N_D value and further negative shift of E_{fb} are another key factor to improve the PEC performance.

As mentioned before, the E_{onset} is correspond to the E_{fb} and the analysis of overpotential can be carried out after the determination of E_{fb} value. By comparing the value of E_{onset} and E_{fb} against Ag/AgCl reference in Table 6.7, it can be proven that all photoanodes have more cathodic E_{onset} values if comparison with E_{fb} values. Thus, this suggest that no overpotential occurred at negative potential range and faster charge transfer happened in this range (see Figure 6.8) which then facilitate the separation of photogenerated electron/hole pairs. Hence, J_{ph} is generated successfully.

6.4 Summary

The photoelectrode performance that fabricated by Ag nanoparticles sensitized ZnO nanopillars with varied Ag^+ ions reduction period and $AgNO_3$ concentration had been discussed accordingly through LSV, Nyquist plot and MS plot. Next chapter will discuss about the conclusion for current study.

CHAPTER 7: CONCLUSIONS AND FUTURE WORKS

7.1 Introduction

This chapter will conclude all the as-obtained outcomes based on the research objectives that listed in Section 1.5 of Chapter 1. Besides, the future works will be suggested for further improvement to attain even more comprehensive outputs.

7.2 Conclusions

The vertically aligned ZnO nanopillars have been successfully grown on Zn foil at lower temperature by using hydrothermal route after some modification had been conducted. The sensitization of Ag nanoparticles on the surface of ZnO nanopillars has been realized by using two steps hydrothermal method under low temperature condition. The sensitization process has been done through two optimized parameters that consisted of varying Ag^+ ions reduction period and $AgNO_3$ salt concentration. Structural- and optical-characterizations have been systematically conducted in order to elucidate their co-relationship.

Based on the PEC performance, Ag nanoparticles sensitized ZnO nanopillars with 30 min Ag^+ ions reduction period and 1 mM $AgNO_3$ concentration exhibit the highest photocurrent density (with maximum photoconversion efficiency), which is almost 1.4 times higher than that of pure ZnO nanopillars. Mott-Schottky analysis indicate that all the photoelectrodes exhibit n-type characteristic, where the flat band potential and charge carrier density for all photoelectrodes can be derived concurrently. Ag/ZnO_30 min and Ag/ZnO_1 mM photoanodes have the highest charge carrier density and possess the most cathodic flat band potential value. In conjugation with this, the investigation of oxidation process at the electrode surface is analyzed via Nyquist plot. Ag nanoparticles sensitized ZnO nanopillars with 30 min Ag^+ ions reduction period and 1 mM $AgNO_3$ salt concentration show the smallest capacitive arc diameter, which indicates that Ag nanoparticles indeed have greatly enhanced the electron mobility and reduce the charge-transfer resistance. With respect to the characterization (structural and optical properties analysis) and PEC performance (photocurrent generations and PEC behaviours) in previous chapters, it can be concluded that after varying the reduction period and concentration of $AgNO_3$ salt, the best condition (which give the most promising result) to grow Ag nanoparticles sensitized ZnO nanopillars heterostructure is the synthesis carried out with 30 min Ag^+ ions reduction time with 1 mM $AgNO_3$ salt concentration.

7.3 Recommendations for Future Works

In this research, a unique broccoli-like structure of Ag/ZnO photoelectrode has successfully grown after modifying the reduction period of Ag^+ ions, whereby this structure was fabricated at lower temperature (50 °C) and without any additional capping agents. In fact, Zn foil itself became a reducing agent to reduce Ag^+ ions and formed the Ag nanoparticles. Interestingly, final wastes of the synthesis are merely water and mild acid nitric. This kind of procedure and method had created new concept or viewpoint, in which had realized great finding in terms of semiconductor synthesis and fabrication. However, some modification and improvement are needed to be done in terms of PEC performances. In order to improve the findings in this research study, there are few suggestions for future works that are expected to assist the development of field for photoelectrochemical study as-listed below:

- Regarding to this research findings, the properties and performance in PEC application is influenced by the sensitization of Ag nanoparticles. The agglomeration as well as the larger particle size of Ag nanoparticles had reduced the photocurrent density. For instance, Ag/ZnO_240 min sample that possessed larger and longer secondary branches of ZnO nanopillars. However, its ability to absorb more solar lights in the visible range due to its larger surface area is hindered by the agglomeration of larger particle size of Ag nanoparticles. On the other hand, its structure cannot be fully utilized in order to enhance the PEC performance. In order to overcome this matter, it is recommended that the sensitization of Ag nanoparticles is conducted by using photoreduction or sputtering method to avoid agglomeration as well as for obtaining smaller size of nanoparticles with good distribution.

- However, hydrothermal approach that used in this research has its own benefit such as facile and easy to prepare sample. Thus, the sensitization process is suggested to be conducted by using surfactant or by utilizing formamide as a medium to synthesis Ag nanoparticles instead of water (in this research). Formamide is widely used in synthesizing noble metals as reported by Xu et al. in 2013. Additionally, formamide is used to fabricate ZnO as well, in which ZnO nanotubes has successfully fabricated on Zn foil as reported by Yu et al. in 2005. Hence, by implementing formamide in this research procedure, probably a well-distribution of small size of Ag nanoparticles and nanotubes structure of ZnO can be produced. In fact, it is more amazing if the structure of secondary branches of ZnO nanotubes is managed to grow. All these will boost up the total surface area for better interaction during PEC process.
- The PEC performance in this research is evaluated via LSV and other analysis which provide the information about the production of J_{ph}. It is suggested that this research should include the H_2 and O_2 production as well, so that the findings is more convincing and strong. However, the current PEC cell used in this current research is not suitable to perform the H_2 and O_2 production test. Thus, designing a new and well-confined PEC cell with feasibility for gas sampling further suggested.
- The analysis of Nyquist plot should be further performed, which is the Randles circuit of each photoanodes should be generated and the value of resistance as well

as capacitor should be calculated from the Randles circuit. This can be performed by fitting the semicircle in Nyquist plot by using NOVA software. Hence, mechanistic insight and more detailed understanding of the PEC phenomena can be well explained. However, the fitting and analysis of this matter need wide and deep knowledge about EIS as well as theory of electronic circuit. Hence, it is recommended for future works.

- ZnO-based photoelectrode is easily to undergo photo corrosion when exposed with light and may degrade the structure as well. Thus the performance of photoelectrode may decrease also. However, the sensitization of Ag nanoparticles on the surface of ZnO can reduce the degradation and photo corrosion process. In order to study and evaluate the stability of structure for Ag/ZnO photoelectrode, the recyclability test must be performed so that the findings of this research is more convincing. Hence, the stability test is suggested for future works.
- The computational technique of finite-difference time-domain (FDTD) to simulate the plasmonic Ag noble metal on the surface of semiconductor nanostructures is highly recommended so that the explanation with respect to the special effect of SPR can deeply understand and discuss.

REFERENCES

Agrawal, R., Singh, N. R., Ribeiro, F. H., & Delgass, W. N. (2007). Sustainable fuel for the transportation sector. *Proceeding of the National Academy of Sciences of the United States of America*, *104*, 4828-4833.

Ahn, K. S., Yan, Y., Shet, S., Deutsch, T., Turner, J., & Al-Jassim, M. (2007). Enhanced photoelectrochemical responses of ZnO films through Ga and N codoping. *Applied Physics Letters*, *91*, 231909-231912.

Ahn, K. S., Shet, S., Deutsch, T., Jiang, C. S., Yan, Y., Al-Jassim, M., & Turner, J. (2008). Enhancement of photoelectrochemical response by aligned nanorods in ZnO thin films. *Journal of Power Sources*, *176*, 387-392.

Ahn, K. S., Yan, Y., Shet, S., Jones, K., Deutsch, T., Turner, J., & Al-Jassim, M. (2008). ZnO nanocoral structures for photoelectrochemical cells. *Applied Physics Letters*, *93*, 163117-163120.

Ahsanulhaq, Q., Kim, J. H., & Hahn, Y. B. (2007). Controlled selective growth of ZnO nanorod arrays and their field emission properties. *Nanotechnology*, *18*, 115603.

Anitha, V. C., Hamnabard, N., Banerjee, A. N., Dillip, G. R., & Joo, S. W. (2016). Enhanced electrochemical performance of morphology-controlled titania-reduced graphene oxide nanostructures fabricated via a combined anodization-hydrothermal process. *RSC Advances*, *6*, 12571-12583.

Ansari, S. A., Khan, M. M., Ansari, M. O., Lee J., & Cho, M. H. (2013). Biogenic synthesis, photocatalytic, and photoelectrochemical performance of Ag-ZnO nanocomposite. *Journal of Physical Chemistry C*, *117*, 27023-27030.

Aydin, C., Abd El-Sadek, M. S., Zheng, K., Yahia, I. S. & Yakuphanoglu, F. (2013). Synthesis, diffuse reflectance and electrical properties of nanocrystalline Fe-doped ZnO via sol-gel calcination technique. *Optics and Laser Technology*, *48*, 447-452.

Bard, A. J. (2008). Book review of light, water, hydrogen: the solar generation of hydrogen by water photoelectrolysis. *Journal of the American Chemical Society*, *130*, 8567-8568.

Bard, A. J., & Faulkner, L. R. (1980). *Electrochemical methods*. New York, NY: John Wiley & Sons.

Barsoukov, E., & Macdonald, J. R. (2005). *Impedance spectroscopy: Theory, experiment and applications.* Chichester, England: John Wiley & Sons.

Biello, D. (2008, June). Inside the solar-hydrogen house: no more power bills-ever. *Scientific American*. Retrieved from https://www.scientificamerican.com.

Bockris, J. O. M., Reddy, A. K. N., & Galboa-Aldeco, M. E. (2011). *Modern electrochemistry 2A- Fundamentals of electronics*. New York: Springer.

Boddy, P. J., Kahng, D., & Chen, Y. S. (1968). Oxygen evolution on potassium tantalate anodes. *Electrochimica Acta, 13,* 1311-1328.

Bookbinder, D. C., Bruce, J. A., Dominey, R. N., Lewis, N. S., & Wrighton M. S. (1980). Synthesis and characterization of a photosensitive interface for hydrogen generation: chemically modified p-type semiconducting silicon photocathodes. *Proceeding of the National Academy of Sciences of the United States of America*, *77,* 6280-6284.

Bopella, R., Anjaneyulu, K., Basak, P., & Manorama, S. V. (2013). Facile synthesis of face oriented ZnO crystals: tunable plar facets and shape induced enhanced photocatalytic performance. *The Journal of Physical Chemistry C, 117,* 4597-4605.

Bott, A. W. (1998). Electrochemistry of semiconductors. *Current Separations, 17,* 87-91.

Brattain, W. H., & Garrett, C. G. B. (1955). Experiments on the interface between germanium and an electrolyte. *Bell System Technical Journal*, *34,* 129-176.

Bumbrah, G. S. & Sharma, R. M. (2016). Raman spectroscopy – Basic principle, instrumentation and selected application for characterization of drugs of abuse. *Egyptian Journal of Forensic Sciences*, *6*, 209-215.

Cai, X., Han, B., Deng, S., Wang, Y., Dong, C., Wang, Y., & Djerdj, I. (2014). Hydrothermal growth of ZnO nanorods on Zn substrates and their application in degradation of azo dyes under ambient conditions. *CrystEngComm*, *16*, 7761-7770.

Chai, B., Wang, X., Cheng, S., Zhou, H., & Zhang, F. (2014). One-pot triethanolamine-assisted hydrothermal synthesis of Ag/ZnO heterostructure microspheres with enhanced photocatalytic activity. *Ceramics International*, *40,* 429-435.

Chauhan, A. & Chauhan, P. (2014). Powder XRD technique and its application in science and technology. *Journal of Analytical and Bioanalytical Techniques*, *5*, 1000212-1000217.

Cheah, A. J., Chiu, W. S., Khiew, P. S., Nakajima, H., Saisopa, T., Songsiriritthigul, P., … Hamid, M. A. A. (2015). Facile synthesis of Ag/MoS_2 nanocomposite photocatalyst for enhanced visible-light driven hydrogen gas evolution. *Catalysis Science & Technology, 5*, 4133-4143.

Chen, C. K., Shen, Y. P., Chen, H. M., Chen, C. H., Chan, T. S., Lee, J. F., & Liu, R. S. (2014). Quantum-dot-sensitized nitrogen-doped ZnO for efficient photoelectrochemical water splitting. *European Journal of Inorganic Chemistry*, *4*, 773-779.

Chen, Z., Dinh, H. N. & Miller, E. (2013). *Photoelectrochemical water splitting: Standards, experimental methods and protocols*. New York, NY: Springer.

Chia, M. Y., Chiu, W. S., Daud, S. N. H., Khiew, P. S., Radiman, S., Abd-Shukor, R., & Hamid, M. A. A. (2015). Structural- and optical-property characterization of three-dimensional branched ZnO nanospikes. *Materials Characterization*, *106*, 185-194.

Cook, T. R., Dogutan, D. K., Reece, S. Y., Surendranath, Y., Teets, T. S., & Nocera, D. G. (2010). Solar energy supply and storage for the legacy and nonlegacy worlds. *Chemical Reviews*, *110*, 6474-6502.

Cundy, C. S., & Cox, P. A. (2003). The hydrothermal synthesis of zeolites: history and development from the earliest days to the present time. *Chemical Reviews*, *103*, 663-702.

Daud, S. N. H., Haw, C. Y., Chiu, W. S., Aspanut, Z., Chia, M. Y., Khanis, N. H., … Hamid, M. A. A. (2016). ZnO nanonails: organometallic synthesis, self-assembly and enhanced hydrogen gas production. *Material Science Semiconductor Processing*, *56*, 228-237.

Davis, S. J., Caldeira, K., & Matthews, H. D. (2010). Future CO_2 emissions and climate change from existing energy infrastructure. *Science*, *329*, 1330-1333.

Deng, Q., Duan, X., Dickon, N. H. L., Tang, H., Yang, Y., Kong, M., … Wang, G. (2012). Ag nanoparticles decorated nanoporous ZnO mircorods and their enhanced photocatalytic activities. *ACS Applied Materials & Interfaces*, *4*, 6030-6037.

Ding, L., Zhang, R., & Fan, L. (2013). Electrochemical route to the synthesis of ZnO microstructures: its nestlike structure and holding of Ag particles. *Nanoscale Research Letters*, *8*, 78-85.

Dittrich, T., Lebedev, E. A., & Weidmann, J. (1998). Electron drift mobility in porous TiO_2 (anatase). *Physic Status Solidi A*, *165*, 5-6.

Dong, Y., Feng, C., Jiang, P., Wang, G., Li, K., & Miao, H. (2014). Simple one-pot synthesis of ZnO/Ag heterostructures and the application in visible light-responsive photocatalysis. *RSC Advances*, *4*, 7340-7346.

Enesca, A., Duta, A., & Schoonman, J. (2007). Study of photoactivity of tungsten trioxide (WO_3) for water splitting. *Thin Solid Films*, *515*, 6371-6374.

Feng, S., & Xu, R. (2001). New materials in hydrothermal synthesis. *Accounts of Chemical Research*, *34*, 239-247.

Fuel Cell and Hydrogen Energy Association. (2015). *State of the States: fuel cells in America 2015* (6th ed.). Washington, DC: Curtin, S & Gangi, J.

Fujishima, A., & Honda, K. (1972). Electrochemical photolysis of water at a semiconductor electrode. *Nature*, *238*, 37-38.

Fultz, B. & Howe, J. M. (2008). *Transmission electron microscopy and diffractrometry of materials*. New York, NY: Springer.

Gerischer, H. (1966). Electrochemical behavior of semiconductors under illumination. *The Journal of Electrochemical Society*, *113*, 1174-1182.

Ghosh, S. K., & Pal, T. (2007). Interparticle coupling effect on the surface plasmon resonance of gold nanoparticles: from theory to applications. *Chemical Reviews*, *107*, 4797-4862.

Grätzel, M. (2001). Photoelectrochemical cells. *Nature*, *414*, 338-344.

Grätzel, M., & Krol, R. V. D. (2012). *Photoelectrochemical hydrogen production*. New York, NY: Springer

Gu, Z., Paranthaman, M. P., Xu, J., & Pan, Z. W. (2009). Aligned ZnO nanorod arrays grown directly on zinc foils and zinc spheres by a low-temperature oxidization method. *ACS Nano, 3*, 273-278.

Guo, K., Liu, Z., Wang, Y., Zhao, Y., Xiao, Y., Han, J., …. Cui, T. (2014). Fabrication of ZnO/$SrTiO_3$ nanoarrays and its photoelectrochemical performances. *International Journal of Hydrogen Energy, 39*, 13408-13414.

Gurney, R. W., & Mott, N. F. (1938). Theory of the photolysis of silver bromide and the photographic latent image. *Proceedings of the Royal Society A, 164*, 151-167.

Haw, C. Y., Chiu, W. S., Abd-Rahman, S., Khiew, P. S., Radiman, S., Abd-Shukor, R., … Ghazali, N. (2016). The design of new magnetic-photocatalyst nanocomposites ($CoFe_2O_4$-TiO_2) as smart nanomaterials for recyclable-photocatalysis applications. *New Journal of Chemistry, 40*, 1124-1136.

He, H., Li, H. Q., Xia, W. W., Shen, X. S., Zhou, M., Han, J. R., … Cai, W. P. (2015). Electrophoretic fabrication of silver nanostructure/zinc oxide nanorod heterogeneous arrays with excellent SERS performance. *Journal of Materials Chemistry C, 3*, 1724-1731.

Henry, D., Eby, N., Goodge, J. & Mogk, D. (10th November 2016). *X-ray reflection in accordance with Bragg's law*. Retrieved from https://serc.carleton.edu/research_education/geochemsheets/BraggsLaw.html.

Hoang, S., Guo, S., Hahn, N. T., Bard, A. J. & Mullins, C. B. (2012). Visible light driven photoelectrochemical water oxidation on nitrogen-modified TiO_2 nanowires. *Nano Letter*, *12*, 26-32.

Hsu, W. D., Tsai, J. K., Meen, T. H., Wu, T. C., He, Y. K., & Lai, Y. D. (2015). Self-etching-induced morphological evolution of ZnO mircorods grown on FTO glass by hydrothermal method. *Nanoscale Research Letters, 10*, 428.

Hsu, Y. K., & Lin, C. M. (2012). Enhanced photoelectrochemical properties of ternary $Zn_{1-x}Cu_xO$ nanorods with tunable band gaps for solar water splitting. *Electrochimica Acta*, *74*, 73-77.

Hsu, Y. K., Chen, Y. C., & Lin, Y. G. (2015). Novel ZnO/Fe_2O_3 core-shell nanowires for photoelectrochemical water splitting. *ACS Applied Materials & Interfaces, 7*, 14157-14162.

Hsu, Y. K., Fu, S. Y., Chen, M. H., Chen, Y. C., & Lin, Y. G. (2014). Facile synthesis of Pt nanoparticles/ZnO nanorod arrays for photoelectrochemical water splitting. *Electrochimica Acta*, *120*, 1-5.

Huang, X. H., Neretina, S., & El-Sayed, M. A. (2009). Gold nanorods: from synthesis and properties to biological and biomedical applications. *Advanced Materials*, *21*, 4880-4910.

Jagadish, C., & Pearton, S. J. (2006). *Zinc Oxide Bulk, Thin Films and Nanostructures*. New York: Elsevier.

Janotti, A., & Chris, G. V. W. (2009). Fundamentals of zinc oxide as a semiconductor. *Reports on Progress in Physics*, *72*, 126501-126530.

Ji, J., Zhang, W., Zhang, H., Qiu, Y., Wang, Y., Luo, Y., & Hu, L. (2013). High density Si/ZnO core/shell nanowire arrays for photoelectrochemical water splitting. *Journal of Materials Science: Materials in Electronics*, *24*, 3474-3480.

Kang, Q., Cao, J., Zhang, Y., Liu, L., Xu, H., & Ye, J. (2013). Reduced TiO_2 nanotube arrays for photoelectrochemical water splitting. *Journal of Materials Chemistry A*, *1*, 5766-5774.

Kar, S., & Santra, S. (2008). ZnO nanotube arrays and nanotube-based paint-brush structures: a simple methodology of fabricating hierarchical nanostructures with self-assembled junctions and branches. *Journal of Physical Chemistry C*, *112*, 8144-8146.

Khan, A. (2010). Raman spectroscopic study of the ZnO nanostructures. *Journal of Pakistan Materials Society*, *4*, 5-9.

Khaselev, O., & Turner, J. A. (1998). A monolithic photovoltaic-photoelectrochemical device for hydrogen production via water splitting. *Science*, *280*, 425-427.

Kibria, M. G. (2012, July). Solar water splitting: a step towards carbon-free energy and environment. *Chemical Engineering & Science Magazine*. Retrieved from http://chethoughts.com.

Klingshirn, C. (2007). ZnO: material, physics and applications. *A European Journal of Chemical Physics and Physical Chemistry*, *8*, 782-803.

Knight, M. W., Sobhani, H., Nordlander, P., & Halas, N. J. (2011). Photodetection with active optical antenna. *Science, 332*, 702-704.

Kudo, A., & Miseki, Y. (2009). Heterogeneous photocatalyst materials for water splitting. *Chemical Society Reviews*, *38*, 253-278.

Kumar, C. S. S. R. (2013). *UV-vis and photoluminescence spectroscopy for nanomaterials characterization*. New York, NY: Springer.

Lerme, J. (2011). Size evolution of the surface plasmon resonance damping in silver nanoparticles: confinement and dielectric effects. *Journal of Physical Chemistry C*, *115*, 14098-14110.

Lewis, N. S. (2007). Toward cost-effective solar energy use. *Science*, *315*, 798-801.

Liang, Y., Guo, N., Li, L., Li, R., Ji, G., & Gan, S. (2015). Fabrication of porous 3D flower-like Ag/ZnO heterostructure composites with enhanced photocatalytic performance. *Applied Surface Science*, *332*, 32-39.

Liang, Y., Guo, N., Li, L., Li, R., Ji, G., & Gan, S. (2016). Facile synthesis of Ag/ZnO micro-flowers and their improved ultraviolet and visible light photocatalytic activity. *New Journal of Chemistry*, *40*, 1587-1594.

List of power stations in Malaysia. (20th August 2016). Retrieved on 14th, August, 2017, from https://en.wikipedia.org/.

Li, Q, Sun, X., Lozano, K., & Mao, Y. (2014). Facile and scalable synthesis of “caterpillar-like” ZnO nanostructures with enhanced photoelectrochemical water-splitting effect. *Journal of Physical Chemistry C*, *118*, 13467-13475.

Li, R., Han, C., & Chen, Q. W. (2013). A facile synthesis of multifunctional ZnO/Ag sea urchin-like hybrids as highly sensitive substrates for surface-enhanced Raman detection. *RSC Advances*, *3*, 11715-11722.

Li, X., Li, J., Cui, C., Liu, Z., & Niu, Y. (2016). PbS nanoparticle sensitized ZnO nanowire arrays to enhance photocurrent for water splitting. *Journal of Physical Chemistry C*, *120*, 4183-4188.

Li, Z., Luan, Y., Wang, Q., Zhuang, G., Qi, Y., Wang, Y., & Wang, C. (2009). ZnO nanostructure construction on zinc foil: the concept from an ionic liquid precursor aqueous solution. *Chemical Communications*, *41*, 6273-6275.

Linic, S., Christopher, P., & Ingram D. B. (2011). Plasmonic-metal nanostructures for efficient conversion of solar to chemical energy. *Nature Materials*, *11*, 911-921.

Liu, H. R., Shao, G. X., Zhao, J. F., Zhang, Z. X., Zhang, Y., Liang, J., … Xu, B. S. (2012). Worm-like Ag/ZnO core-shell heterostructural composites: fabrication, characterization, and photocatalysis. *The Journal of Physical Chemistry C*, *116*, 16182-16190.

Liu, M., Nam, C. Y., Black, C. T., Kamcev, J., & Zhang, L. (2013). Enhancing water splitting activity and chemical stability of Zinc Oxide nanowire photoanodes with ultrathin Titania shells. *Journal of Physical Chemistry C*, *117*, 13396-13402.

Liu, Y., Gu, Y., Yan, X., Kang, Z., Lu, S., Sun, Y., & Zhang, Y. (2015). Design of sandwich-structured ZnO/ZnS/Au photoanode for enhanced efficiency of photoelectrochemical water splitting. *Nano Research*, *8*, 2891-2900.

Liu, Y., Yan, X., Kang, Z., Li, Y., Shen, Y., Sun, Y., … Zhang, Y. (2016). Synergetic effect of surface plasmonic particles and surface passivation layer on ZnO nanorods array for improved photoelectrochemical water splitting. *Scientific Reports*, *6*, 29907-29914.

Lu, W., Gao, S., & Wang, J. (2008). One-pot synthesis of Ag/ZnO self-assembled 3d hollow microspheres with enhanced photocatalytic performance. *Journal of Physical Chemistry C*, *112*, 16792-16800.

Luan, C., Vaneski, A., Susha, A. S., Xu, X., Wang, H. E., Chen, X.,… Zapien, J. A. (2011). Facile solution growth of vertically aligned ZnO nanorods sensitized with aqueous CdS and CdSe quantum dots for photovoltaic applications. *Nanoscale Research Letters*, *6*, 340-348.

Ma, W., Gu, Z., Nan, H., Geng, B., & Zhang, X. (2015). Morphology-controllable synthesis of 3D firecracker-like ZnO nanoarchitectures for high catalytic performance. *CrystEngComm*, *17*, 1121-1128.

Ma, W., Shi, Q., Nan, H., Zheng, X., Geng, B., & Zhang, X. (2015). Hierarchical ZnO@MnO$_2$@PPy ternary core–shell nanorod arrays: an efficient integration of active materials for energy storage. *RSC Advances*, *5*, 39864-39869.

Maeda, K., Masuda, H., & Domen, K. (2009). Effect of electrolyte addition on activity of $(Ga_{1-x}Zn_x)(N_{1-x}O_x)$ photocatalyst for overall water splitting under visible light. *Catalysis Today*, *147*, 173-178.

Maeda, K., Teramura, K., & Domen, K. (2008). Effect of post-calcination on photocatalytic activity of $(Ga_{1-x}Zn_x)(N_{1-x}O_x)$ solid solution for overall water splitting under visible light. *Journal of Catalysis*, *254*, 198-204.

Miao, J., Yang, H. B., Khoo, S. Y., & Liu, B. (2013). Electrochemical fabrication of ZnO–CdSe core–shell nanorod arrays for efficient photoelectrochemical water splitting. *Nanoscale*, *5*, 11118-11124.

Millar, G. J., Metson, J. B., Bowmaker, G. A., & Cooney R. P. (1995). Influence of oxidation and reduction condition upon the morphology of silica-supported polycrystalline silver catalysts. *Journal of the Chemical Society, Faraday Transactions*, *91*, 133-139.

Ming, T., Zhao, L., Yang, Z., Chen, H., Sun, L., Wang, J., & Yan, C. (2009). Strong polarization dependence of plasmon-enhanced fluorescence on single gold nanorods. *Nano Letters*, *9*, 3896-3903.

Mogensen, K. B., & Kneipp, K. (2014). Size-dependent shifts of plasmon resonance in silver nanoparticle films using controlled dissolution: monitoring the onset of surface screening effects. *Journal of Physical Chemistry C*, *118*, 28075-28083.

Morales, A. E., Pal, U. & Zaldivar, M. H. (2008). Incorporation of Sb in ZnO nanostructures through hydrothermal process. *Journal of Nanoscience and Nanotechnology*, *8*, 6551-6557.

Morkoç, H., & Özgür, U. (2009). *Zinc oxide: fundamentals, materials and device technology*. England: John Wiley & Sons.

Murphy, A. B., Barnes, P. R. F., Randeniya, L. K., Plumb, I. C., Grey, I. E., Home, M. D., & Glasscock, J. A. (2006). Efficiency of solar water splitting using semiconductor electrodes. *International Journal of Hydrogen Energy*, *31*, 1999-2017.

Nevet, A., Berkovitch, N., Hayat, A., Ginzburg, P., Ginzach, S., Sorias, O., & Orenstein, M. (2010). Plasmonic nanoantennas for broad-band enhancement of two-photon emission from semiconductors. *Nano Letters*, *10*, 1848-1852.

Niu, B. J., Wu, L. L., Tang, W., Zhang, X. T., & Meng, Q. G. (2011). Enhancement of near-band edge emission of Au/ZnO composite nanobelts by surface plasmon resonance. *CrystEngComm*, *13*, 3678-3681.

Ni, M., Leung, M. K. H., Leung, D. Y. C., & Sumathy, K. (2007). A review and recent developments in photocatalytic water-splitting using TiO_2 for hydrogen production. *Renewable and Sustainable Energy Reviews, 11*, 401-425.

Ogden, J. M., & Williams, R. H. (1990). Electrolytic hydrogen from thin-film solar cells. *International Journal of Hydrogen Energy, 15*, 155-169.

Osterloh, F. E., & Parkinson, B. A. (2011). Recent developments in a solar water-splitting photocatalysis. *MRS Bulletin, 36*, 17-22.

Pacholski, C., Kornowski, A., & Weller, H. (2004). Site-specific photodeposition of silver on ZnO nanorods. *Angewandte Chemie, 116*, 4878-4881.

Peralta, M. D. L. R., Pal, U., & Zeferino, R. S. (2012). Photoluminescence (PL) quenching and enhanced photocatalytic activity of Au-decorated ZnO nanorods fabricated though microwave-assisted chemical synthesis. *ACS Applied Materials & Interfaces, 4*, 4807-4816.

Polte, J. (2015). Fundamental growth principles of colloidal metal nanoparticles – a new perspective. *CrystEngComm, 17*, 6809-6830.

Pompa, P. P., Martiradonna, L., Torre, A. D., Sakla, F. D., Manna, L., Vittorio, M., … Rinaldi, R. (2006). Metal-enhanced fluorescence of colloidal nanocrystals with nanoscale control. *Nature Nanotechnology, 1*, 126-130.

Porter, M. D., Lipert, R. J., Siperko, L. M., Wang, G., & Narayanan, R. (2008). SERS as a bioassay platform: fundamentals, design, and applications. *Chemical Society Reviews, 37*, 1001-1011.

Prasad, M. A. & Sangaranarayanan, M. V. (2004). Analysis of the diffusion layer hickness, equivalent circuit and conductance behaviour for reversible electron transfer processes in linear sweep voltammetry. *Electrochimica Acta, 49*, 445-453.

Qi, J., Dang, X., Hammond, P. T., & Belcher, A. M. (2011). Highly efficient plasmon-enhanced dye-sensitized solar cells through metal@oxide core–shell nanostructure. *ACS Nano, 5*, 7108-7116.

Quintana, M., Edvinsson, T., Hagfeldt, A., & Boschloo, G. (2007). Comparison of dye-sensitized ZnO and TiO_2 solar cells: studies of charge transport and carrier lifetime. *The Journal of Physical Chemistry C, 111*, 1035-1041.

Raman, C. V. & Krishnan, K. S. (1928). A new type of secondary radiation. *Nature*, *121*, 501-502.

Ren, X., Sangle, A., Zhang, S., Yuan, S., Zhao, Y., Shi, L., … MacManus-Driscoll, J. L. (2016). Photoelectrochemical water splitting strongly enhanced in fast-grown ZnO nanotrees and nanocluster structures. *Journal of Materials Chemistry A*, *4*, 10203-10211.

Sau, T. K., Rogach, A. L., Jackel, F., Klar, T. A., & Feldmann, J. (2010). Properties and applications of colloidal nonspherical noble metal nanoparticles. *Advanced Materials*, *22*, 1805-1825.

Scanning electron microscope A to Z: Basic knowledge for using the SEM. (25th June 2009). Retrieved 3rd, March, 2017, from http://www.jeolusa.com/.

Shaban, Y. A., & Khan, S. U. M. (2007). Surface grooved visible light active carbon modified (CM)-n-TiO_2 thin films for efficient photoelectrochemical splitting of water. *Chemical Physics*, *339*, 73-85.

Shelton, S. (2015, July). World's largest eco-friendly hydrogen plant opens in Germany. *Hybridcars*. Retrieved from http://www.hybridcars.com.

Shi, W., Song, S., & Zhang, H. (2013). Hydrothermal synthetic strategies of inorganic semiconducting nanostructures. *Chemical Society Reviews*, *42*, 5714-5743.

Sivula, K., Formal, F. L., & Grätzel, M. (2009). WO_3-Fe_2O_3 photoanodes for water splitting: a host scaffold, guest absorber approach. *Chemistry of Materials*, *21*, 2862-2867.

Smith, E & Dent, G. (2005). *Modern Raman spectroscopy: a practical approach*. Chichester, England: John Wiley & Sons.

Sounart, T. L., Liu, J., Voigt, J. A., Huo, M., Spoerke, E. D., & McKenzie, B. (2007). Secondary nucleation and growth of ZnO. *Journal of the American Chemical Society*, *129*, 15786-15793.

Sun, K., Jing, Y., Li, C., Zhang, X., Aguinaldo, R., Kargar, A., … Wang, D. (2012). 3D branched nanowire heterojunction photoelectrodes for high-efficiency solar water splitting and H_2 generation. *Nanoscale*, *4*, 1515-1521.

Sun, K., Madsen, K., Andersen, P., Bao, W., Sun, Z., & Wang, D. (2012). Metal on metal oxide nanowire co-catalyzed Si photocathode for solar water splitting. *Nanotechnology*, *23*, 194013-194023.

Sun, X., Li, Q., Jiang, J., & Mao, Y. (2014). Morphology-tunable synthesis of ZnO nanoforest and its photoelectrochemical performance. *Nanoscale, 6*, 8769-8780.

Swapp, S. (26th May 2017). *Scanning electron microscopy (SEM)*. Retrieved from http://serc.carleton.edu/research_education/geochemsheets/techniques/SEM.html.

Tachibana, Y., Vayssieres, L., & Durrant, J. R. (2012). Artificial photosynthesis for solar water-splitting. *Nature Photonics*, *6*, 511-518.

Tao, G., Li, S., Ma, C., Liu, K., & Zhang, Q. Y. (2015). A highly sensitive and recyclable SERS substrate based on Ag-nanoparticle-decorated ZnO nanoflowers in ordered arrays. *Dalton Transactions*, *44,* 3447-3453.

Thanh, N. T. K., Maclean, N., & Mahiddine, S. (2014). Mechanisms of nucleation and growth of nanoparticles in solution. *Chemical Reviews*, *114,* 7610-7630.

Titov, A. V., & Král, P. (2008). Modelling the self-assembly of colloidal nanorod superlattices. *Nano Letters*, *8*, 3605-3612.

Unalan, H. E., Wei, D., Suzuki, K., Dalal, S., Hiralal, P., Matsumoto, H., … Amaratunga, G. A. J. (2008). Photoelectrochemical cell using dye sensitized zinc oxide nanowires grown on carbon fibers. *Applied Physics Letters*, *93,* 133116-133119.

Upadhyay, S., Bagheri, S., & Abd-Hamid, S. B. (2014). Enhanced photoelectrochemical response of reduced-graphene oxide/$Zn_{1-x}Ag_xO$ nanocomposite in visible-light region. *International Journal of Hydrogen Energy*, *39*, 11027-11034.

Vuong, N. M., Reynolds, J. L., Conte, E., & Lee, Y. I. (2015). H:ZnO nanorod-based photoanode sensitized by CdS and carbon quantum dots for photoelectrochemical water splitting. *Journal of Physical Chemistry C*, *119*, 24323-24331.

Wang, F., Seo, J. H., Li, Z., Kvit, A. V., Ma, Z., & Wang, X. (2014). Cl-doped ZnO nanowires with metallic conductivity and their application for high-performance photoelectrochemical electrodes. *ACS Applied Materials & Interfaces*, *6*, 1288-1293.

Wang, G., Yang, X., Qian, F., Zhang, J. Z., & Li, Y. (2010). Double-sided CdS and CdSe quantum dot co-sensitized ZnO nanowire arrays for photoelectrochemical hydrogen generation. *Nano Letters*, *10*, 1088-1092.

Wang, J., Li, Y., Ge, J., Zhang, B. P., & Wan, W. (2015). Improving photocatalytic performance of ZnO via synergistic effects of Ag nanoparticles and graphene quantum dots. *Physical Chemistry Chemical Physics, 17*, 18645-18652.

Wang, T., Jiao, Z., Chen, T., Li, Y., Ren, W., Lin, S., … Bi, Y. (2013). Vertically aligned ZnO nanowire arrays tip-grafted with silver nanoparticles for photoelectrochemical applications. *Nanoscale*, *5*, 7552-7557.

Wang, T., Lv, R., Zhang, P., Li, C., & Gong, J. (2015). Au nanoparticle sensitized ZnO nanopencil arrays for photoelectrochemical water splitting. *Nanoscale, 7*, 77-81.

Wang, Z. L. (2008). Splendid one-dimensional nanostructures of zinc oxide: a new nanomaterial family for nanotechnology. *ACS Nano*, *2*, 1987-1992.

Warule, S. S., Chaudhari, N. S., Ambekar, J. D., Kale, B. B., & More, M. A. (2011). Hierarchical nanostructured ZnO with nanorods engendered to nanopencils and pin-cushion cactus with its field emission study. *ACS Applied Materials & Interfaces, 3*, 3454-3462.

Wei, Y., Ke, L., Kong, J., Liu, H., Jiao, Z., Lu, X., …. Sun, X. W. (2012). Enhanced photoelectrochemical water-splitting effect with a bent ZnO nanorod photoanode decorated with Ag nanoparticles. *Nanotechnology*, *23*, 235401-235409.

Wei, Y., Ke, L., Leong, E. S. P., Liu, H., Liew, L. L., Teng, J. H., … Sun, X. W. (2012). Enhanced photoelectrochemical performance of bridged ZnO nanorod arrays grown on v-grooved structure. *Nanotechnology*, *23*, 365704-365710.

Wei, Y., Kong, J., Yang, L., Ke, L., Tan, H. R., Liu, H., … Du, H. (2013). Polydopamine-assisted decoration of ZnO nanorods with Ag nanoparticles: an improved photoelectrochemical anode. *Journal of Materials Chemistry A*, *1*, 5045-5052.

Whang, T. J., Hsieh, M. T., & Chen, H. H. (2012). Visible-light photocatalytic degradation of methylene blue with laser-induced Ag/ZnO nanoparticles. *Applied Surface Science, 258*, 2796-2801.

Williams, D. B. & Carter, C. B. (2009). *Transmission electron microscopy: A textbook for material science*. New York, NY: Springer.

Willard, H. H., Meritt, J. L. L., Dean, J. J. & Settle, J. F. A. (1988). *Instrumental methods of analysis*. New Delhi, India: CBS Publisher & Distributors.

Wolcott, A., Smith, W. A., Kuykendall, T. R., Zhao, Y., & Zhang, J. Z. (2009). Photoelectrochemical study of nanostructured ZnO thin films for hydrogen generation from water splitting. *Advanced Functional Materials, 19*, 1849-1856.

Wu, M., Chen, W. J., Shen, Y. H., Huang, F. Z., Li, C. H., Li, S. K. (2014). In situ growth of matchlike ZnO/Au plasmonic heterostructure for enhanced photoelectrochemical water splitting. *ACS Applied Materials & Interfaces*, *6*, 15052-15060.

Wu, Z., Xue, Y., Wang, H., Wu, Y., & Yu, Hao. (2014). ZnO nanorods/Pt and ZnO nanorods/Ag heterostructures arrays with enhanced photocatalytic degradation of dyes. *RSC Advances*, *4*, 59009-59016.

Wu, Z. C., Xu, C. R., Wu, Y., Yu, H., Tao, Y., Wan, H., & Gao. F. (2013). ZnO nanorods/Ag nanoparticles heterostructures with tunable Ag contents: a facle solution-phase synthesis and applications in photocatalysis. *CrystEngComm*, *15*, 5994-6002.

Xiao, M., Jiang, R., Wang, F., Fang, C., Wang, J., & Yu, J. C. (2013). Plasmon-enhanced chemical reactions. *Journal of Materials Chemistry A*, *1*, 5790-5805.

Xu, B., Zhang, Z., & Wang, X. (2013). Formamide: an efficient solvent to synthesize water-soluble and sub-ten-nanometer nanocrystals. *Nanoscale*, *5*, 4495-4505.

Xu, C., Song, Y., Lu, L., Cheng, C., Liu, D., Fang, X., … Li, D. (2013). Electrochemically hydrogenated TiO_2 nanotubes with improved photoelectrochemical water splitting performance. *Nanoscale Research Letters*, *8*, 1-7.

Yang, H., Jin, Z., Hu, H., Lu, G., & Bi, Y. (2017). Fivefold enhanced photoelectrochemical properties of ZnO nanowire arrays modified with C_3N_4 quantum dots. *Catalysts, 7*, 99-111.

Yang, L., Zhou, H., Fan, T., & Zhang, D. (2014). Semiconductor photocatalysts for water oxidation: current status and challenges. *Physical Chemistry Chemical Physics*, *16*, 6810-6826.

Yang, X., Wolcott, A., Wang, G., Sobo, A., Fitzmorris, R. C., Qian, F., … Li, Y. (2009). Nitrogen-doped ZnO nanowire arrays for photoelectrochemical water splitting. *Nano Letters*, *9*, 2331-2336.

Yin, J., Zang, Y., Yue, C., Wu, Z., Wu, S., Li, J., & Wu, Z. (2012). Ag nanoparticles/ZnO hollow nanospheres arrays: large scale synthesis and surface plasmon resonance effect induced Raman scattering enhancement. *Journal of Materials Chemistry*, *22*, 7902-7909.

Yu, H., Zhang, Z., Han, M., Hao, X., & Zhu, F. (2005). A general low-temperature route for large-scale fabrication of highly oriented ZnO nanorod/nanotube arrays. *Journal of American Chemical Society*, *127*, 2378-2379.

Yu, Y. X., Ouyang, W. X., Liao, Z. T., Du, B. B., & Zhang, W. D. (2014). Construction of ZnO/ZnS/CdS/$CuInS_2$ core−shell nanowire arrays via ion exchange: p−n junction photoanode with enhanced photoelectrochemical activity under visible light. *ACS Applied Materials & Interfaces*, *6*, 8467-8474.

Zak, A. K., Abrishami, M. E., Abd-Majid, W. H., Yousefi, R., & Hosseini, S. M. (2011). Effects of annealing temperature on some structural and optical properties of ZnO nanoparticles prepared by a modified sol-gel combustion method. *Ceramics International*, *37*, 393-398.

Zamiri, R., Rebelo, A., Zamiri, G., Adnani, A., Kuashal, A., Belsley, M. S., & Ferreira J. M. F. (2014). Far-infrared optical constants of ZnO and ZnO/Ag nanostructures. *RSC Advances*, *4*, 20902-20908.

Zare, M., Mortezaali, A., & Shafiekhan, A. (2016). Photoelectrochemical determination of shallow and deep trap states of platinum-decorated TiO_2 nanotube arrays for photocatalytic applications. *Journal of Physical Chemistry C*, *120*, 9017-9027.

Zhang, S. Y., Regulacio, M. D., & Han, M. Y. (2014). Self-assembly of colloidal one-dimensional nanocrystals. *Chemical Society Reviews*, *43*, 2301-2323.

Zhang, X., Li, Y., Zhao, J., Wang, S., Li, Y., Dai, H., & Sun, X. (2014). Advanced three-component ZnO/Ag/CdS nanocomposite photoanode for photocatalytic water splitting. *Journal of Power Sources*, *269*, 466-472.

Zhang, X., Liu, Y. & Kang, Z. (2014). 3D branched ZnO nanowire arrays decorated with plasmonic Au nanoparticles for high-performance photoelectrochemical water splitting. *Applied Materials & Interfaces*, *6*, 4480-4489.

Zhang, X., Qin, J., Xue, Y.,Yu, P., Zhang, B., Wang, L., & Liu, R. (2014). Effect of aspect ratio and surface defects on the photocatalytic activity of ZnO nanorods. *Scientific Reports*, *4*, 1-8.

Zhang, X., Zhao, J., Wang, S., Dai, H., & Sun, X. (2014). Shape-dependent localized surface plasmon enhanced photocatalytic effect of ZnO nanorods decorated with Ag. *International Journal of Hydrogen Energy*, *39*, 8238-8245.

Zheng, Y., Zheng, L., Zhan, Y., Lin, X., Zheng, Q., & Wei, K. (2007). Ag/ZnO heterostructure nanocrystals: synthesis, characterization, and photocatalysis. *Inorganic Chemistry*, *46*, 6980-6986.

Zhou, J., Xu, N. S., & Wang, Z. L. (2006). Dissolving behavior and stability of ZnO wires in biofluids: a study on biodegradability and biocompatibility of ZnO nanostructures. *Advanced Materials*, *18*, 2432-2435.

Zhou, L., Yang, R, Yu, M., Bai, F., Li, C., & Wang, Z. L. (2008). Cellular level biocompatibility and biosafety of ZnO nanowires. *Journal of Physical Chemistry C*, *112*, 20114-20117.

Zijlstra, P., James, W. M. C., & Gu, M. (2009). Five-dimensional optical recording mediated by surface plasmons in gold nanorods. *Nature*, *459*, 410-413.

Zou, Z., Ye, J., Sayama, K., & Arakawa, H. (2001). Direct splitting of water under visible light irradiation with an oxide semiconductor photocatalyst. *Nature*, *414*, 625-627.

LIST OF PUBLICATIONS AND PAPERS PRESENTED

Publications

Daud, S. N. H., Haw, C. Y., Chiu, W. S., Aspanut, Z., Jani, N. A., Khiew, P. S., Chin, L. Y., Abd. Hamid, M. A., & Ali, A. M. (2017). 3D hyperbranched heterostructures of Ag nanocrystals decorated ZnO nanopillars: controlled growth and optical properties characterization. *CrystEngComm*, *19*, 5591-5603.

Daud, S. N.H., Haw, C. Y., Chiu, W. S., Aspanut, Z., Chia, M. Y., Khanis, N. H., Khiew, P. S., & Abd. Hamid, M. A. (2016). ZnO nanonails: organometallic synthesis, self-assembly and enhanced hydrogen gas production. *Materials Science in Semiconductor Processing*, *56*, 228-237.

Paper Presented

Morphology tuning of ZnO nanostructures grown on zinc foil using facile and low temperature hydrothermal method.
24th Scientific Conference of the Microscopy Society Malaysia (SCMSM 2015), 2nd-4th December 2015, Avillion Hotel, Malacca.